MICROPOROUS CRYSTALLINE MATERIALS FOR METHANE HYDRATE GROWTH

by

Shurraya A. Denning

A thesis submitted to the Faculty and the Board of Trustees of the Colorado School of Mines in partial fulfillment of the requirements for the degree of Doctor of Philosophy (Chemical Engineering).

Golden, Colorado

Date _____

Signed: _____

Shurraya A. Denning

Signed: _____

Dr. Moises A. Carreon

Thesis Advisor

Signed: _____

Dr. Carolyn A. Koh

Co-Thesis Advisor

Golden, Colorado

Date _____

Signed: _____

Dr. Anuj Chauhan

Professor and Head

Department of Geophysics

ABSTRACT

Natural gas represents a high and constantly growing demand as an energy source, as it possesses a high heating value and burns cleaner than other conventional fossil fuels or coal. Effective strategies for natural gas storage are essential due to the fluctuations in demand, and are in need of improvement so as to not waste this energy source.

Gas hydrates, also generally referred to as hydrates, exhibit the potential to efficiently storage methane, the primary component of natural gas, due to their large methane uptake capacity, non-explosive nature, and being environmentally begin. The barriers to commercialization of hydrates for methane storage arise from slow hydrate growth and low water-to-hydrate conversion. A proposed solution to these issues involves the addition of microporous crystals as hydrate promoters, as the properties of the materials can greatly influence hydrate formation.

In this work, we investigated the effects of selected microporous crystals on methane hydrate formation to gain better insight as to what properties of porous materials lend to promoting hydrate growth. We focused on a range of microporous material compositions, studying organic-inorganic hybrids (metal organic frameworks), organic (porous organic cages), and inorganic (zeolites). These studies also elucidated the effects of metal ions (present in metal organic frameworks) and surface hydrophobicity on methane hydrate formation. This work may pave a new path towards the commercialization of hydrates for methane storage, and could improve the feasibility of implementing gas hydrates for other applications, such as carbon dioxide sequestration.

TABLE OF CONTENTS

LIST OF FIGURES

LIST OF TABLES

LISTS OF SYMBOLS

Mass ratio of water to crystalline material……R_w

Molecular weight of water……MW_{H2O}

Hydration number……..n_{HYD}

Heat of dissociation of methane structure I hydrate……..H_{HYD}

Hydrate dissociation measured in the high pressure differential scanning calorimeter……H_{diss}

Size of crystallite……L

Scherrer's shape factor constant……K

Wavelength……..λ

Full width of the peak at half its maximum intensity……B

Diffraction angle……θ

ACKNOWLEDGEMENTS

I appreciatively acknowledge my advisors Moises A. Carreon and Carolyn A. Koh for their guidance and support during my Ph.D. work. They put their faith in me when they first accepted me into the program, and helped me succeed despite the hurdles that stood in my way. The praise they offered me along with gentle critique motivated me to work hard and explore new ideas.

I thank my committee members, Dr. Luis E. Zerpa, Dr. Joseph R. Samaniuk, and Dr. Nikki Farnsworth their helpful comments and questions, as they probed me to think of aspects on a broader scale, to see the forest instead of just focusing on the tree.

I want to show gratitude towards three incredible colleagues, Dr. Jolie Lucero, Dr. Ahmad AA Majid, and James M. Crawford. They helped me brainstorm many times and provided excellent insight that stemmed from their different backgrounds and expertise. I want to especially thank Dr. Jolie Lucero as she not only trained and mentored me, but she also shared a friendship with me that kept me in a positive mindset throughout all of the trials I faced.

I also want to acknowledge the Hydratebusters at the Center for Hydrate Research who initially inspired my passion for research and drive to obtain my PhD. They provided me a kind and welcoming environment, from offering doughnuts to attending my speaking events.

I want to recognize the unending support and unconditional love I received from my husband, Aaron Denning. He encouraged me to find a healthy work/life balance, and made the life part of the balance joyful and fun. He also kept me true to my faith, knowing I needed that solid foundation in my life.

Lastly, I want to thank my family for their support, especially my grandparents Joan and Richard Gillies. They showed me the value of education and determination through their own life stories, and encouraged me to never let the negativity of the world stop me from achieving what I wanted from life.

CHAPTER 1 INTRODUCTION

Porous materials and gas hydrates occur in many different areas, both in nature and engineered in laboratories. The types of porous materials range from sediments like clay or rocks to crystalline like zeolites or metal-organic frameworks. The diversity of porous materials, such as structures (e.g. pore size, surface area) and chemical composition (e.g. organic, inorganic), results in an array of functionalities and applications. Gas hydrates, an ice like structure that encapsulates guest molecules, appear as a nuisance in oil and gas operations as it can form plugs in pipelines, and in sediments on the ocean floor, where it contains vast amounts of natural gas. The simplicity of the gas hydrates (i.e. consists of only water and guest molecules) makes it appealing to target the encaging of specific guest molecules, such as carbon sequestration. Both porous materials and gas hydrates hold the potential for applications that would increase the sustainability of energy usage, especially natural gas. The following sections highlight the motivation for utilizing porous materials and gas hydrates, and the relevant applications.

1.1 Motivation: Energy Demand

The ever-increasing population growth demands for more resources, ranging from food to energy. The U.S. Energy Information Administration predicts that the global energy consumption will rise from ~450 quadrillion British thermal units (BTUs) consumed in 2018 to ~900 quadrillion BTU by 2050.[1] Over the last seven years, the amount of natural gas consumption in the United States reached an average of 26 trillion cubic feet (TCF), with an average increase in consumption each year of 4.3 billion cubic feet (BCF).[2] The United States currently leads as the world's highest natural gas producer with an estimate increase in production from ~29 TCF in 2018 to ~43 TCF in 2050.[1] Consequentially, in 2017 natural gas was the second largest sector of energy in the United States and provided approximately 28% of the total amount of energy consumed.[2]

The ever-growing demand for energy drives the research of sources with less environmental impact to both minimize the carbon footprint and prevent the release of toxins, such as hydrogen sulfide. Compared to petroleum products, natural gas is considered a cleaner energy source, as the combustion natural gas produces primarily carbon dioxide, water, and small amounts of nitrogen oxides.[3,4] Despite the predicted rapid increase in renewable energy sources by 2050, the use of natural gas will still steadily grow with an expected 40% increase from 2018 to 2050.[1] In order to exploit this cleaner energy source, the extracted natural gas needs

efficient storage and purification. The following sections briefly cover specifics related to natural gas storage and separation.

1.2 Natural Gas Storage & Transportation

When the demand for natural gas is low, due to factors such as low prices or summer time versus winter, gas storage provides a means to conserve the fuel until it is an appropriate time to use it. Currently, natural gas is most commonly stored in underground facilities, such as a depleted reservoir, aquifer, or salt caverns.[4] Although these methods became more common after World War II and have since undergone further development, underground facilities are geologically and geographically limited.[4] Seeking alternative storage methods would provide a means to become independent of the geological and geographical limits. This independence extends beyond the situation of using natural gas for electricity generation or commercial/residential heating and cooling to less common areas, including but not limited to: transportation without a pipeline and natural gas as fuel to replace gasoline in vehicles.

Due to the high cost of pipeline construction, other modes of transporting natural gas are in high demand for either remote production facilities, facilities with small yield, and for remote areas requiring the consumption of natural gas. Although liquefied natural gas (LNG) is currently used today to transport natural gas via tankers, trucks, and railroads, this process requires a significant amount of energy to cool the fuel to -162°C, and the boil off from LNG can over pressurize the tank.[5]

As mentioned before, replacing the use of the petroleum product gasoline for vehicles with natural gas would result in less harmful off gas and more efficient fuel usage. One major issue with using natural gas in this way stems from the low density of natural gas. Currently, there are vehicles that utilize natural gas, but this fuel is stored in highly pressurized, heavy tanks due to the low density of natural gas, which pose a major safety hazard.[3,6] If the fuel could be stored at closer to ambient pressures, this hazard could be significantly reduced and thus promote further development of natural gas fueled vehicles.

Two alternative storage methods currently undergoing research and development are adsorbents and gas hydrates. Both of these methods will be discussed in detail in the later sections.

1.3 Applications of Porous Materials

The properties of microporous materials, such as structure and chemical makeup, influences its interactions with gases and thus it's potential for gas storage.[7] Among those properties include: uniform porosity, surface area, pore accessibility, adsorption capacity, and a system of interconnected pores and channels.[8] Due to the harsh conditions of natural gas, the microporous material must be thermally, chemically, and mechanically stable.

1.3.1 Gas Storage via Sorption

The microporous material's surface area plays an extremely important role in its effectiveness as a natural gas adsorbent. Multiple studies found that a material with higher surface area typically adsorbs more methane, which applies to a range of materials including zeolites, metal-organic frameworks (MOFs), activated carbon, and polymers.[9,10] One study concluded that the surface area of a porous material effects the adsorption capacity significantly more than any other property of the material.[10]

Another important aspect is the chemical nature of the material, specifically the adsorption sites. The type of adsorption site determines what type of gas molecule is more likely to adsorb, and the strength of adsorption. Notably, a strong adsorption of methane to a porous material must be balanced out with how easily the methane can be released after storage.[6] Although gas storage in porous materials is promising, and in some cases already being applied industrially, continued research is needed to explore and gain a better understanding of gas storage in porous materials to make the process more economically feasible and efficient, and to determine the lifetime and recycling of the material.[7]

1.4 Applications of Gas Hydrates

The properties of guest molecule specific hydrate structure stability and thermodynamic stability lend to the development of gas hydrates for gas storage. The properties also lead to the stable formation of naturally occurring methane hydrate deposits in oceanic sediments, which is currently being investigated as a potential new energy source.

1.4.1 High Gas Storage Capacity in Hydrates

A single crystal gas hydrate can capture a significantly large amount of gas; for example, 164 m^3 of CH_4 at STP is captured in 1 m^3 of hydrate.[11] This capacity significantly reduces the volume of natural gas when it is captured in a hydrate, making it ideal for storage.[12] Additionally, hydrates can exhibit a self-preservation phenomenon upon dissociation in which

after hydrate formation at low temperature and high pressures, lowering the pressure does not cause immediate dissociation.[11] The understanding of self-preservation is limited, but many studies suggest that an ice-like shield forms on the outside of the hydrate, which prevents the gas from escaping.[11,13] For example, one study showed that methane could be stored at ambient pressure and at -5°C for up to 10 days.[12] If natural gas can be transported at ambient pressure and temperatures, then this method could replace the costly procedure of liquefaction of natural gas, which one study estimated could be a cost saving of 24%.[14] Furthermore, the precursors required for gas hydrate formation are water and gas, making the process nearly environmentally benign, making this method high desirable.

1.4.2 Energy Source in Naturally Occurring Hydrates in Oceanic Sediments

The naturally occurring gas hydrates most often found in oceanic sediments is an up and coming potential energy resource. Surveyors estimate that there is around 1.5×10^{16} m^3 of methane stored in naturally occurring hydrate deposits, and that over 220 of these deposits exist.[15] Currently, there is convincing field and simulation data that indicates that extracting the methane from these deposits using a method of depressurizing the hydrates works well.[16–20] The exploitation of this resource runs into many barriers that currently prevent it from becoming economically feasible. Although some deposits, as found in China, Alaska N. Slope, India, and Japan, contain a high density of naturally occurring gas hydrates, many other sources face the barrier of low resource density.[21] The key to opening up more opportunities for naturally occurring hydrates is to find a way to extract the methane efficiently from the oceanic sediments. One of the keys to making this process efficient is to obtain a better understanding of gas hydrate growth and stability in porous materials. Characterizing a methane hydrate deposit would narrow down the type of extraction process would be best suited for the particular geological system.[21] More research into how different types of porous materials effect hydrate formation, dissociation, growth, and nucleation will provide a better means to characterize a naturally occurring hydrate deposit.

1.5 Thesis Organization

The central objective of this proposal is to explore how structural, compositional, morphological, and textural properties of microporous materials influence the nucleation and growth of methane gas hydrates. Chapter 1 introduces the motivation of this work, the demand for natural gas, and the applicable aspects of porous materials and gas hydrates in the storage and

transportation of natural gas. The first section of Chapter 2 discusses the different classes of porous materials relevant to this work: metal organic frameworks, porous organic cages, and zeolites. The second section of Chapter 2 covers aspects of hydrate growth and thermodynamic stability. The third section of Chapter 2 reviews current literature on the synergistic effects of porous materials and gas hydrates on methane storage. In Chapter 3, the effects of the metal organic framework HKUST-1 on methane hydrate growth will be explored to gain a better understanding of how the mild wettability and high thermal conductivity increases water-to-hydrate conversion and decreases hydrate nucleation induction time. Chapter 4 extends the study on HKUST-1 to determine the scalability of the hydrate promotion results to a large, packed column. The effect of subcooling on the performance of HKUST-1 as a promoter will be studied by varying the pressure and temperature conditions of the column, along with varying the concentration of HKUST-1 in the system. Chapter 5 contains an investigation of the metal organic frameworks ZIF-8 and ZIF-67 as methane hydrate promoters. The focus is to see how two microporous materials with the same sodalite topology and differing metal ions effect hydrate conversion and nucleation induction time. Chapter 6 a purely organic microporous material, CC3, will be studied to observe the effects of a purely organic microporous material on methane hydrate growth. In Chapter 7 the zeolites SSZ-13, and SAPO-34 will be used to examine how the hydrophobicity of zeolites with the same chabazite structure effects methane hydrate growth. Lastly, Chapter 8 will summarize the findings of the work completed in this thesis, and provide recommendations for future work.

CHAPTER 2 LITERATURE REVIEW

2.1 Microporous Crystals

Microporous materials are defined as porous materials with pore diameters less than ~2nm and include a vast range of physical and chemical properties. The following sections focus on three classes of microporous materials: metal-organic frameworks, porous organic cages, and zeolites.

2.1.1 Metal-Organic Frameworks

Significant research is targeting the development of metal-organic frameworks (MOF), a crystalline material consisting of metal clusters linked with organic molecules, as a means of gas storage and separation. The advantages of MOFs that contribute to the potential for storage and separation stems from accessible pore volumes and adsorption sites, free pore volume, molecular sieving pore aperture, and chemical stability (especially with water and hydrocarbons). [22]

The methane storage capacity may be improved or tuned by changing the chemical composition of a MOF, as MOFs are chemically diverse. One study used Raman spectroscopy to determine that the linkers in the structure play an essential part in how methane gas adsorbed to a isoreticular MOF.[23] Another study further investigated the adsorption site of MOFs with a low density of unsaturated metal centers, specifically HKUST-1, PCN-11, and PCN-14, and found that the metal site coordinated with the gas molecule significantly more than with the linkers.[24]

The MOF HKUST-1, illustrated in Figure 2.1, exhibits promising results for methane storage, with a reported uptake of 270 cc(STP)/cc at 65 bar that surpasses the Department of Energy (DOE) target volumetric uptake of 263 cc(STP)/cc at 65 bar (ignoring packing efficiency loss).[25] The two primary methane adsorption cites in HKUST-1 are the small cage window site and open copper site.[24]

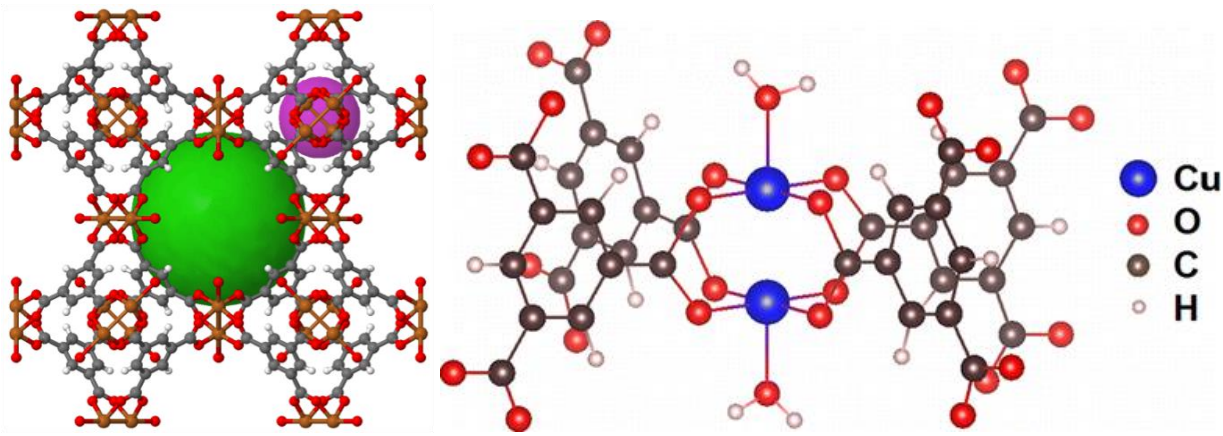

Figure 2.1 (Left) Structure of HKUST-1 where the spheres represent the different cages, with internal pore aperture of 1.0 nm and 1.4 nm.[26] (Right) The blue represents copper, red represents oxygen, grey represents carbon, and white represents hydrogen.[27]

Another two MOFs of interest are ZIF-8 and ZIF-67, which are zeolitic imidazolate frameworks with the same sodalite topology and composed of 2-methylimidazole ligands linking zinc ions and cobalt ions, respectively.[28] A representative image of ZIF-8 (top right) and ZIF-67 (bottom right) are giving in Figure 2.2.

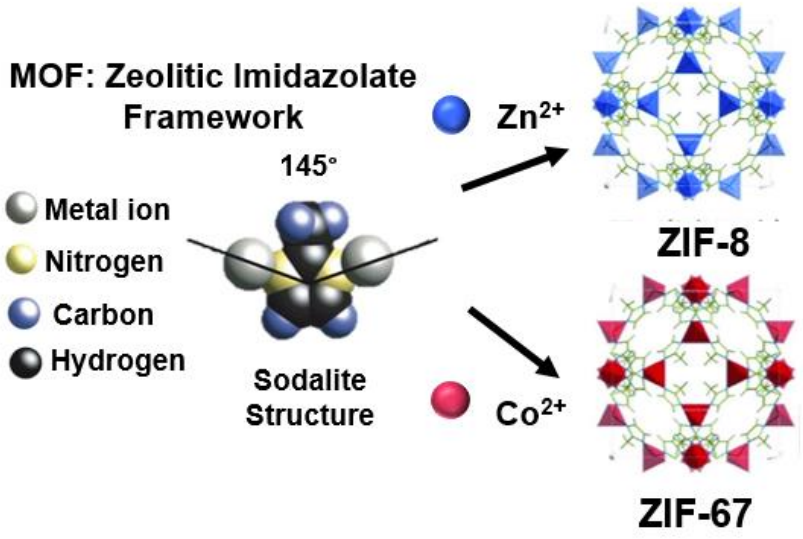

Figure 2.2 Representation of the metal organic framework subclass known as zeolitic imidazolate framework (ZIF) bond angle for the sodalite topology respective to two prototypical ZIFs: zinc based ZIF-8 (top right) and cobalt based ZIF-67 (bottom right), in which the large pore diameter is 1.2 nm.[29]

Both ZIFs exhibit high chemical and thermal stability. Unlike HKUST-1, methane adsorbs preferentially to the organic linker of these ZIFs rather than the metal ion cite.[30] A study using neutron powder diffraction found that methane preferentially adsorbed to the organic linker with a secondary adsorption site on the zinc ion.[31]

2.1.2 Porous Organic Cages

Porous organic cages (POCs) are comprised of organic molecules covalently bonded together to form a cage. These cages can assemble to produce a 3D diamonoid crystalline microporous structure with uniform pore size and large surface areas that are chemically and thermally stable.[32] What makes this material very different from zeolites and MOFs is that the cages are discrete building blocks, thus in addition to the cage's intrinsic cavity, the assembly of cages form extrinsic voids. Most POC synthesis involves a cycloimination reaction, and a variety of amines and trialdehydes required for this reaction result in the formation of different cages.[33] The morphology, structure, and texture of a POC can be controlled by stirring and solvothermal treatment conditions, offering a wide variety of tunable properties.[34,35]

A highly studied POC is CC3, which is made up of 1,3,5-triformylbezene coordinated with trans-1,2,-diaminocyclohexane, is a good candidate for methane storage.[33] Figure 2.3 contains an illustration of the material's framework. The tunable properties of CC3, such as its density, can affect the extent of gas storage.[36]

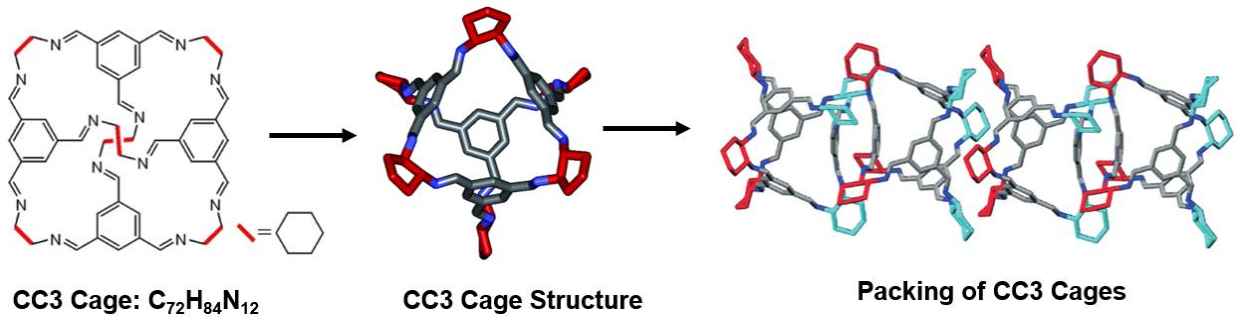

Figure 2.3 Representative image of a prototypical porous organic cage denoted as CC3.[37,38]

A study conducted on using functionalized CC3 found that it could adsorb a significant amount of methane, as the cage's internal surfaces acts as a good adsorption site, and the cage geometry is optimal for confining methane.[36]

In addition to gas storage, CC3 shows promise as membrane as the limiting pore size of CC3 is approximately 3.6 Å and therefore able to molecularly sieve small impurities such as CO_2, N_2, and H_2 from the primary component of natural gas, CH_4.[35] One study found that diffusion dominated the high permeation seen in the CC3 membrane.[39] Although this material show good potential, very little literature exists on synthesis of a pure CC3 membrane for gas separations, as most times CC3 or other POCs are incorporated into polymer membranes to form a mix matrix membrane.

2.1.3 Zeolites

A zeolite is an aluminosilicate (i.e. oxygen linked alumina, silica, and/or phosphorous tetrahedral) uniform microporous crystalline material with a rigid pore structure, and is chemically, mechanically, and thermally stable.[40] Figure 1.1 illustrates the framework of a zeolite with chabazite topology. Many different zeolites exist, differing in aspects such as structure, porosity, topology, and chemistry. These properties play into whether or not a type of zeolite will be suitable for gas storage or gas separation, which is typically specific for what type of gas is in question.[6]

Open cage frameworks, surface area, pore size, and pore volume all effect the amount of methane adsorbed, with some properties promoting adsorption better than others.[41] One study observed that in a comparison of sodium based zeolites, the one with the largest surface area and pore volume absorbed more methane despite having the smallest pore diameter.[41] Additionally, the surface chemistry of zeolites influences the amount of methane stored with a particular emphasis on the structure's charge, the hydrophobicity, and the acidity of the zeolite.[42,43] As seen with zeolite SAPO-34, a silico-aluminophosphate zeolite with chabazite topology shown in Figure 2.4, the polarity of the gas influences the extent of adsorption due to the interaction between the gas molecule and the anionic framework of SAPO-34.[44,45] Overall, the gas storage performance of a zeolite is determined by structure and chemistry.

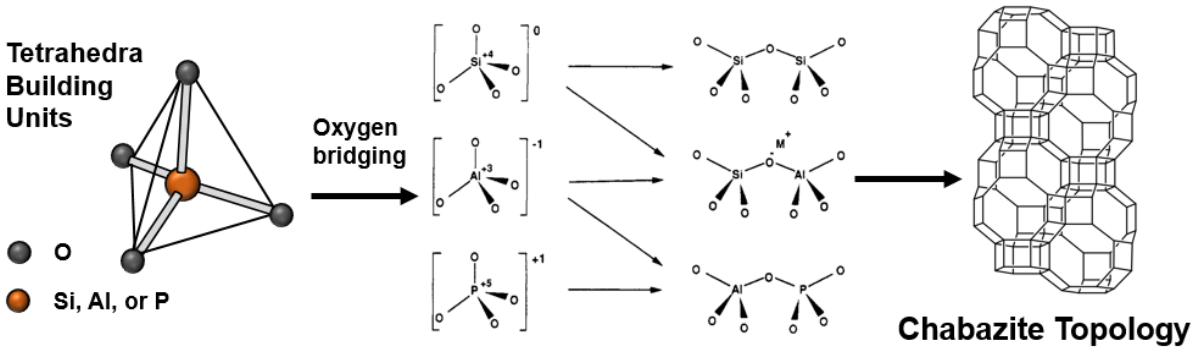

Figure 2.4 Tetrahedral building units of the zeolite structures forming oxygen bridges that result in an overall structural topology.[46,47]

A large variety of zeolites are applied in the form of a membrane for gas separation. SAPO-34, shows promising separation for natural gas as it can separate out a range of impurities: CO_2/CH_4[48–50], N_2/CH_4[51–53], He/CH_4[45] and H_2/CH_4[54]. The primary driving force for these separations through SAPO-34 stems from the molecular sieving capabilities, as the pore size of SAPO-34 is 3.8 Å, which sieves CO_2 (3.3 Å), N_2 (3.6 Å), He (2.6 Å), and H_2 (2.9 Å) from CH_4 (3.8 Å).[55] For the gas mixture CO_2/CH_4, the CO_2 adsorbs relatively better than CH_4 to the surface of SAPO-34, hence competitive adsorption makes this separation highly successful. The other gases, N_2, He, and H_2, do not adsorb relatively better to the surface of SAPO-34, but their small size allows for a higher rate of diffusion. This example goes to show how different aspects of a membrane can promote or impede separation of natural gas impurities from methane. Numerous other zeolite membranes in literature successfully separated CO_2/CH_4 (zeolite T [56], SSZ-13 [57,58], FAU-type [59], DD3R [60]) and N_2/CH_4 (SSZ-13 [58], DD3R [60]), to name a few.

2.2 Gas hydrates

Gas hydrates, as mentioned previously, occur in nature as an energy source and show potential for application to methane storage and gas separation. The following sections describe gas hydrates in more detail, highlighting how the properties of gas hydrates effect the potential applications.

2.2.1 Structure

A gas hydrate consists of water molecules that form hydrogen bonds around a guest molecule (typically a gas), and coordinate together into a crystalline structure.[11] The guest molecule interacts with the water via van der Waals forces, and the strength of this force influences the stability of the structure of the hydrate. The stable hydrate formation region

requires high pressure and low temperature, with the position of the stability region dependent upon the type of guest molecule. The guest molecules promote the formation of different hydrate structures, with the most common being structure I (sI), structure II (sII), and structure H (sH), as shown in Figure 2.5.[11]

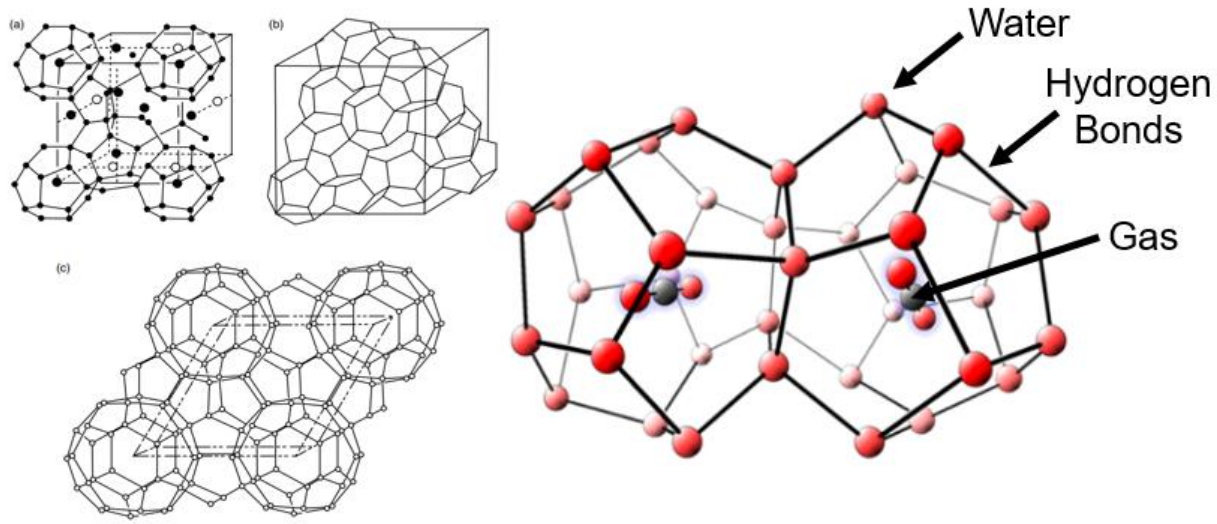

Figure 2.5 Left - representative image of gas hydrate structures: (a) cubic structure I, (b) cubic structure II, and (c) hexagonal structure H.[11] The most common 5^{12}, $5^{12}6^2$, and $5^{12}6^4$ cages that compose these structures are 3.95Å, 4.33Å, and 4.73Å in diameter, respectively.[11] Right – illustration of structure I hydrate with gas encapsulated inside.

The structures differ in what size cages it contains and the number of those cages in a unit cell, which relates to how many water molecules are required to form that unit cell.[11] The type of guest molecule factors into determining what structure is formed partly due to ratio of the molecule diameter and the cavity size of the cages in a structure.[11] A ratio close to 1, yet not exceeding 1, correlates with high hydrate stability, as a larger diameter molecule in the cage results in more repulsion between the guest and water molecules. The van der Waals interactions between the guest molecule and the water increase in strength as that repulsion is increased, which in turn stabilizes the cavity. Notably, the hydrate structure is so dependent upon its guest molecules for stabilization that hydrates will not form unless the properly sized guest molecule is present.

2.2.2 Thermodynamics

The stability of the hydrate structure also depends upon whether or not the temperature and pressure conditions of the system lie within the phase envelope. The phase envelope depends upon both the type of guest molecule and the structure formed. Figure 2.6 depicts the phase envelope for methane hydrate structure I, with values obtained from Gibbs free energy minimization software CSMGem.

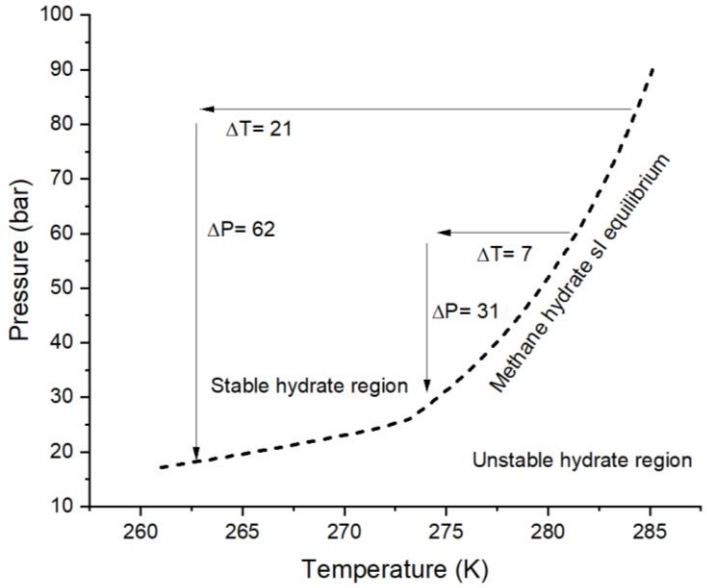

Figure 2.6 Phase boundary for methane hydrate structure I, plotted from CSMGem. Driving force in terms of subcooling temperature (ΔT) and pressure (ΔP) indicated for two sets of temperature and pressure system conditions.[61]

The two arbitrary points in the stable hydrate region in Figure ## illustrate how a larger subcooling (hydrate equilibrium temperature at a given pressure minus the temperature of the system) and a larger pressure driving force (hydrate equilibrium pressure at a given temperature minus the pressure of the system) promotes a higher degree of hydrate stability. When a higher driving force and subcooling are applied, then system fluctuations are less likely to disturb the system as compared to a system that operates with conditions closer to that of the phase boundary.

An additive can shift the hydrate stability region, either by thermodynamically inhibiting hydrate stability (curve shifts left) or by promoting it (curve shifts right). For example, methanol and sodium chloride are both used as thermodynamic inhibitors in oil and gas pipelines where

the operating conditions typically reside in the hydrate stability zone.[62] The shift in the curve allows the system to continue operating at those conditions while reducing the risk of hydrate formation and potentially a hydrate plug.[62] Conversely, additives such as tetrahydrofuran (THF) shift the curve to the right, which is advantageous for applications such as energy storage in hydrates.[63]

2.2.3 Kinetics

The process for hydrate nucleation is stochastic in nature, and therefore the onset of the nucleation is not necessarily reproducible.[64] Additionally, homogeneous hydrate formation rarely takes place in practical conditions, as anything from an impurity in the water phase or the wall of a reactor can act as a hydrate nucleation site.[64] These aspects makes the study of hydrate kinetics difficult. Hydrate nucleation depends heavily upon the extent of subcooling in the system ($\Delta T=T_{eq} - T_{sys}$) and the length of time the system has been at the subcooled temperature.[65] Figure 2.7(1) depicts the general scheme for hydrate formation: induction time (length of time before hydrate nucleation), initial rate of consumption (occurs right after nucleation starts), rate of consumption (formation that is limited by initial growth thus occurs at slower rate).[11]

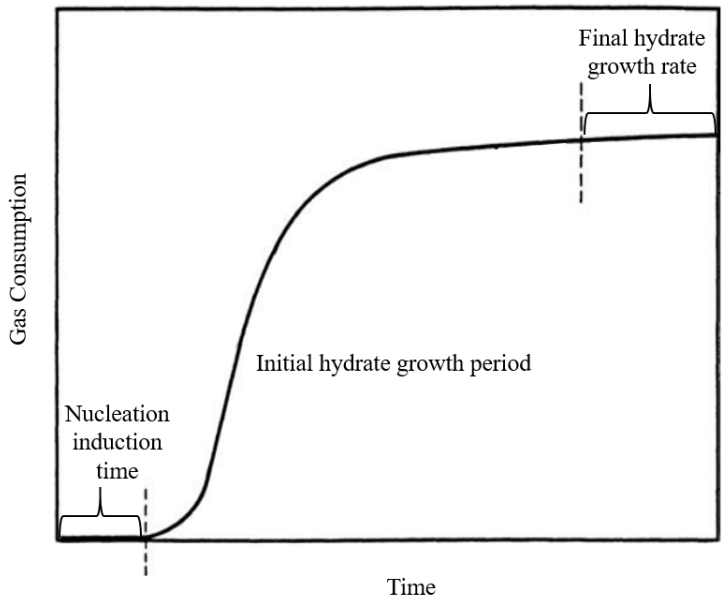

Figure 2.7 Growth graph, one of pressure drop versus temperature during formation.[11]

When hydrates form and dissociate in a system, the next cycle of formation may exhibit effects from water memory. Hence, when the system is primed to the conditions for hydrate

formation, the hydrates may form with a reduced induction time as compared to the first induction period. This phenomena is not well understood, with some researchers hypothesizing that after the first cycle of hydrate formation, nanobubbles of gas are trapped in the liquid phase as a result from the dissociation of the hydrates, and thus act as a local source for hydrate formation, hence why it occurs faster.[66]

Similarly to the thermodynamics aspect of hydrates, there are additives that can affect the kinetics of hydrate formation. Certain additives promote hydrate growth, such as sodium dodecyl sulfate (SDS). A molecular dynamics study on SDS's effect on hydrate growth determined that the capability of SDS to greatly increase the rate of hydrate growth stems from the hydrophobic tail interacting favorably with the initial hydrate surface and potentially occupying some of the hydrate's partial cages.[67] Kinetic inhibitors target aspects of hydrate growth, typically by lengthening the induction time for hydrate nucleation. An example of a kinetic inhibitor is polyvinylpyrrolidone (PVP), which similarly to SDS interacts with the growing surface of the hydrates, yet the way it binds to the surface inhibit the growth.[68]

2.2.4 Mass & Heat Transfer Effects on Hydrate Growth

The hydrate formation process can be slowed significantly by mass and heat transfer limitations. The initial formation of gas hydrates in a system typically takes place at the interface between the gas and water phase.[69] This formation creates a film at the interface, trapping the water phase. Although this film can still permit gas diffusion due to the hydrate's porous nature, the film stunts the rate of hydrate growth. The hydrate film depends upon many factors, such as the extent of subcooling, with its crystallization occurring as a continuous growth mechanism.[69] One way to help mitigate this limitation is by increasing the gas-to-water contact area, which can be achieved by many means such as apparatus design (e.g. bubble column,[70] stirred tanks[71]) and porous materials (e.g. silica glass,[72] activated carbon[73]).

Hydrate formation is an exothermic process, which limits itself as the local heat given off warms the nearby area, making it less desirable for more hydrates to form. The impact of this limitation can be reduced by introducing something into the system that is thermally conductive, such as copper heat transfer plates[74] and porous materials with copper nodes[26].

2.2.5 Self Preservation

A kinetic anomaly associated with hydrates, called 'self-preservation', occurs when the dissociation of the hydrate results in a supercooled liquid water film forming at the interface of

the gas and water phase which prevents the now trapped gas molecules from escaping.[75] This supercooled liquid water film can freeze to form a layer of ice (illustrated in Figure 2.8, and thus 'preserves' the hydrate encased inside despite the conditions of the system being outside of the hydrate stability region.[75]

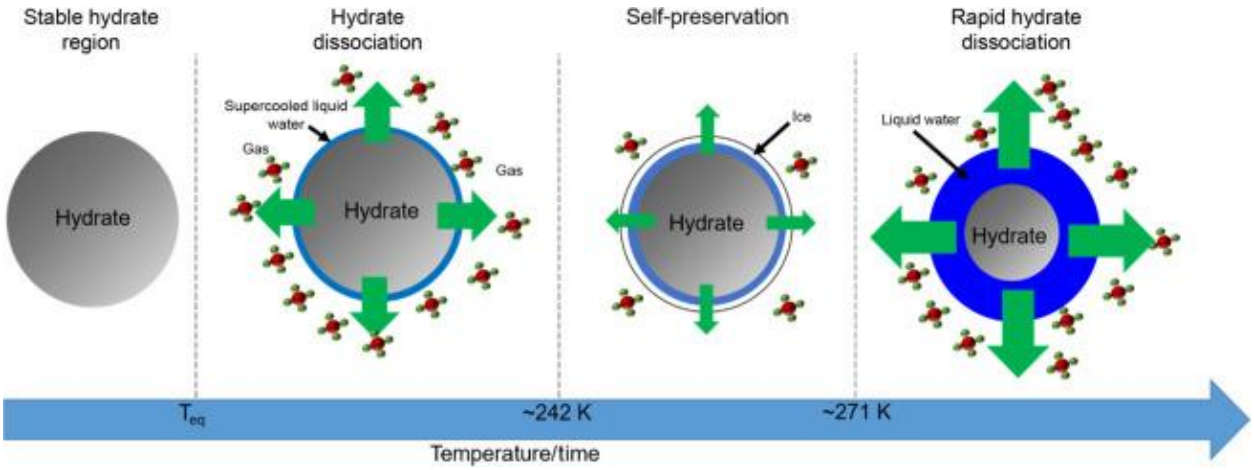

Figure 2.8 Illustration of temperature effects on hydrate structure stability.[75]

Self-preservation can be harnessed for energy storage, as a hydrate can be used to capture a gas such as methane, and then preserved at ambient pressure and temperatures slightly below the freezing point of ice, which can be stable up to weeks or months.[75–77] The methane gas is easily recovered from the hydrate, as warming the system above the freezing point of ice results in rapid hydrate dissociation, as shown in Figure ##.

2.3 Combining Gas Hydrates with Porous Crystals

Porous materials combined with gas hydrates may increase the overall gas storage and separation potential by combating two major obstacles in terms for gas hydrates: long induction time for hydrate formation and limited water to hydrate conversion. Porous materials offer many advantages for gas hydrate nucleation and growth promotion, with two being surface chemistry and material structure. Surface chemistry of the material may induce more hydrate growth and faster nucleation and growth due to reasons ranging from hydrophobicity to thermal conductivity.[78,79] The structure of the material impacts hydrate nucleation and growth many ways, such as surface area, which increases the gas-to-water interface, and pore volume, which if large enough can confine hydrates within, as illustrated in Figure 2.9.[79,80]

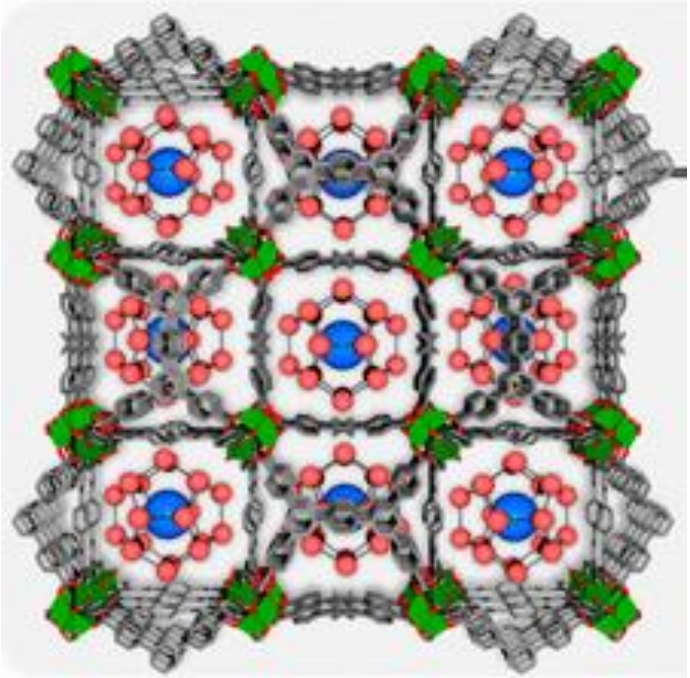

Figure 2.9 Metal organic framework with metal nodes (green) linked with organic ligands (grey) containing a methane (blue) hydrate consisting of water molecules (red) forming hydrogen bonds around the gas molecule.[81]

A vast array of different porous materials have been studied, ranging from activated carbon,[82,83] classic order mesoporous carbon CMK-3,[84] silica gels,[85] to smectite clays[86]. The materials of interest in this work are zeolites, metal-organic frameworks, and porous organic cages. These microporous materials cover three primary chemical nature groups: inorganic (zeolite), organic-inorganic (metal-organic frameworks), and organic (porous organic cages). The following subsections discuss the reasoning and potential of three microporous materials as promoters for hydrate formation and growth.

2.3.1 MOFs as Promoters for Gas Hydrate Formation

Metal-organic frameworks (MOFs) possess unique properties that not only make this porous material suitable for gas storage and separation, but these properties extend to make MOFs interesting for promoting gas hydrate formation. These properties include chemical diversity (e.g. surface chemistry, framework composition), structural flexibility due to its organic linkers, generally large surface area (~1000 m^2/g), and tunable porosity.[87]

Similarly to zeolites, the cavity size of a MOF must exceed the size of a structure I hydrate, which has a unit cell length of 1.2 nm. An advantage MOFs have over zeolites is the flexibility of the framework, as a zeolite is composed of purely inorganic components while

MOFs are a mix of organic and inorganic. The organic ligands that link the metal ions together in the framework can flex, making it easier for the MOF to adjust in size when a hydrate forms inside the pore cavity.

There are only a few studies conducted on MOFs and methane gas hydrates. One of the completed studies compared hydrophobic ZIF-8 and hydrophilic MIL-53(Fe) and found that the hydrophobicity of ZIF-8, combined with its high adsorption of methane, resulted in more methane storage and more water-to-hydrate conversion than MIL-53(Fe).[87] Thus, the chemical nature of a MOF can be optimized as a gas hydrate promoter.

Some of the studies on gas hydrate growth in microporous metal-organic frameworks (MOFs) encompass the following materials: MIL-53,[88] MIL-53(Al),[89] ZIF-8,[87,89,90] MIL-101,[91] and MIL-100(Fe)[87].

This next table, Table 2.1, summarizes the studies that used metal organic frameworks (MOFs) to promote gas hydrate formation.

Table 2.1 Summary of studies on the different types of MOFs that have been employed as methane hydrate promoters and corresponding comments on experimental procedures and overall conclusions from the study.

Type of MOF	Comments	Ref.
MIL-53(Al)	Recorded pressure and temperature in a reactor. Measured hydrate equilibrium curve with the material present, matches that of bulk water. At 274.15K and pressures 0 to 10 MPa, less methane stored in system with MIL-53 & hydrates versus a system with dry MIL-53.	89
MIL-100(Fe)	Methane high pressure adsorption. Water-to-hydrate conversion 56% at 4 MPa and 275K.	87
MIL-53	Low-temperature synchrotron high-resolution powder diffraction. Hydrates form in meso/macro pores. Equilibrium curves measured.	88
ZIF-8	Recorded pressure and temperature in a reactor. Measured hydrate equilibrium curve with the material present, matches that of bulk water. At 274.15K and pressures 0 to 10 MPa, ZIF-8 combined with gas hydrates increased the amount of methane stored relative to dry ZIF-8.	89

Table 2.1 continued.

ZIF-8	Methane high pressure adsorption, inelastic neutron scattering, and synchrotron x-ray powder diffraction. Nearly 100% water-to-hydrate conversion.	[87]
	Measured pressure drop. The net methane stored in the material with hydrates is 56% more than that of the dry material at 269.15K and 2.85 MPa.	[90]
MIL-101	Microsecond molecular dynamics simulations. Methane hydrate forms preferentially on outer surface. Hydrophilicity causes water to block cavities, decreasing the amount of methane in cavities as the water content increases.	[91]
Cr-soc-MOF-1	High pressure methane isotherms 275K, 0 to 10 MPa. At 10 MPa, this material combined with hydrates stores 50% more methane as compared to the dry material. Conversion of 66%	[73]
Y-shp-MOF-5	The addition of this material did not increase the overall amount of methane stored relative to how much the dry material can store.	[73]
HKUST-1	Measured heat consumed/released using high pressure differential scanning calorimeter. Water-to-hydrate conversion reached a high of 87.2% at 8 MPa.	[26]

2.3.2 POCs as Promoters for Gas Hydrate Formation

POCs offer a unique structure that could promote gas hydrate growth and nucleation as the material has intrinsic cavities in a discrete cage, and extrinsic voids formed by the packing of these cages.[92] As this crystalline material is purely organic, it also offers a similar advantage as MOFs in terms of an expanding pore size, which could accommodate a gas hydrate unit cell if the pore is close to or larger than 1.2 nm.[11]

Some POCs, such as CC3, show high water stability, a feature essential for a gas hydrate promoter.[92] The cage geometry of this material promotes high methane adsorption, which may aid in hydrate nucleation due to the gas adsorbing to the surface.[36] CC3 also proved stable under high pressure conditions with methane gas, further showing that this porous material may work

well as a gas hydrate formation promoter. As far as the author is aware, no studies on gas hydrate growth in POCs has been executed.

2.3.3 Zeolites as Promoters for Gas Hydrate Formation

A zeolite has many desirable properties for gas hydrate formation, such as mechanical, thermal, and chemical stability. The mechanical stability, stemming from four oxygen atoms bridging the Si, Al, and/or P atoms together, is essential as high pressures are required for the formation of gas hydrates, which could crush a structure, making it no longer useful.[44] The thermal stability is necessary to withstand the low temperatures need for hydrate formation, and the cycling of cooling and heating that would take place if the material is reused. Chemical stability would prevent the various compositions of natural gas and the water present to form hydrates from degrading the material.

Other properties of zeolites that may influence gas hydrate formation is its surface area, which can be as high as ~800 m^2/g,[93] tunable acid-base chemistry,[94] varying hydrophobicity,[95] and pore diameter and volume[41]. The cavity size of a zeolite determines whether or not gas hydrates can form within the pores. The unit cell length of a structure I hydrate, the most common structure, formed with methane, is 1.2 nm, therefore the cavity size of the zeolite must be larger.[11,96] For zeolite RHO, the cavity size is 1.0 nm, suggesting that the pores will contain water and/or gas, but no hydrates.[96] The pores near the external surface of the crystal may act as nucleation sites for gas hydrates, explaining in part why RHO promoted hydrate nucleation.[96] Some of the studies on the growth of methane hydrates in microporous zeolites in literature are RHO,[96] 13X,[89,97] 5A,[97–99] 3A,[98] and 13A[97].

The following Table 2.2 summarizes the studies in literature that involve methane gas hydrate growth by zeolites.

Table 2.2. Summary of the types of zeolites studied as promoters for methane hydrate growth with comments on the experimental procedure and results.

Type of Zeolite	Comments	Ref.
RHO	Chemical additives: THF. At 100 bar, 275K, and 60,000s, amount of CH4 adsorbed reached 140 mmol/g.	96

Table 2.2 continued.

13A Zeolite	Measured amount of gas consumed. Equilibrium curve determined. At a subcooling temperature of 2K, nucleation time reduced from 18 hours to 8 hours, whereas at >7K, no reduction in nucleation time was observed.	97
13X Zeolite	Measured amount of gas consumed. Equilibrium curve determined. At a subcooling temperature of 2K, nucleation time reduced from 18 hours to 2.5 hours, whereas at >7K, no reduction in nucleation time was observed.	97
	No chemical additives. Recorded pressure and temperature in a reactor. Measured hydrate equilibrium curve with the material present, matches that of bulk water.	89
5A Zeolite	Measured amount of gas consumed. Equilibrium curve determined. At a subcooling temperature of 2K, nucleation time reduced from 18 hours to 5 hours, whereas at >7K, no reduction in nucleation time was observed.	97
	Chemical additives: SDS. Mechanical agitation and magnetic stirring. 8.4 MPa, 273.5K. Measured amount of gas in hydrate. Without SDS, gas storage capacity of methane hydrate (volume ratio) is 54, while with SDS it is 156.	98
	Chemical additives: THF, TBAB. 1.5 & 1.8 MPa, 285.15K Reduced hydrate nucleation time. Measured pressure drop. Performance based on gas uptake. Highest gas to hydrate conversion 39.42%.	99
3A Zeolite	Chemical additives: SDS. Mechanical agitation and magnetic stirring. 8.4 MPa, 273.5K. Measured amount of gas in hydrate. Without SDS, gas storage capacity of methane hydrate (volume ratio) is 62, while with SDS it is 178.	98

CHAPTER 3
METAL ORGANIC FRAMEWORK HKUST-1 PROMOTES METHANE HYDRATE FORMATION FOR IMPROVED GAS STORAGE CAPACITY

Modified from: S. Denning, A.AA. Majid, J.M. Lucero, J.M. Crawford, M.A. Carreon, C.A. Koh*, "Metal−Organic Framework HKUST-1 Promotes Methane Hydrate Formation for Improved Gas Storage Capacity" ***ACS Applied Materials & Interfaces 2020,*** 12, 47, 53510-53518

In this chapter, we studied the synergistic effects of the copper based metal organic framework HKUST-1 and gas hydrates for the purpose of methane storage. The following chapter covers the results of the study along with the experimental methods used, which is also published in ACS Applied Materials & Interfaces, 2020, 12, 47, 53510-53518.

3.1 Porous Crystals for Methane Hydrate Formation Promotion

This work aims to further investigate porous materials as a hydrate growth promoter. Porous materials provide two primary desired advantages: the material increases the surface area of gas-to-water contact, and the surface chemistry of the material may induce faster gas hydrate nucleation and growth [78,79]. Researchers have investigated an extensive number of materials (including but not limited to): activated carbon [82,100,101], functionalized carbon nanotubes [102], silica gels [85,103], silica glass [72,104], silica sand [105,106], clay [86,107], Ottawa sand [108], polyurethane foam [109], aluminum foam [110], carbon CMK-3 [84], zeolites [96–99,111], and metal organic frameworks (MOFs) [79]. The last material listed, MOFs, offer a unique combination of properties that are seemingly advantageous for promoting gas hydrate formation: namely, high surface area and an assortment of different surface chemistries and structures. The MOFs investigated experimentally and/or via computer simulations, as far as we are aware of, consist of the following: MIL-101 [91], MIL-53 [88], MIL-100 [87], and ZIF-8 [87,90].

The work presented here focuses on employing the metal-organic framework HKUST-1 (or $Cu_3(BTC)_2$) as a promoter for methane hydrate growth. This MOF is comprised of copper nodes linked by 1,3,5-benzenetricarboxylic acid, resulting in a structure with bimodal pores [112]. HKUST-1 shows promise as a material for promoting gas hydrate formation mainly due to its high surface area, typically ~1000 m^2/g [112,113], internal pore apertures of 1.4 nm and 1.0 nm [114],

high volumetric methane uptake [25], and thermally conductive structural chemistry [115]. Figure 3.1 illustrates the structure of HKUST-1 (left) and structure I hydrate (right), although not to scale [116,117].

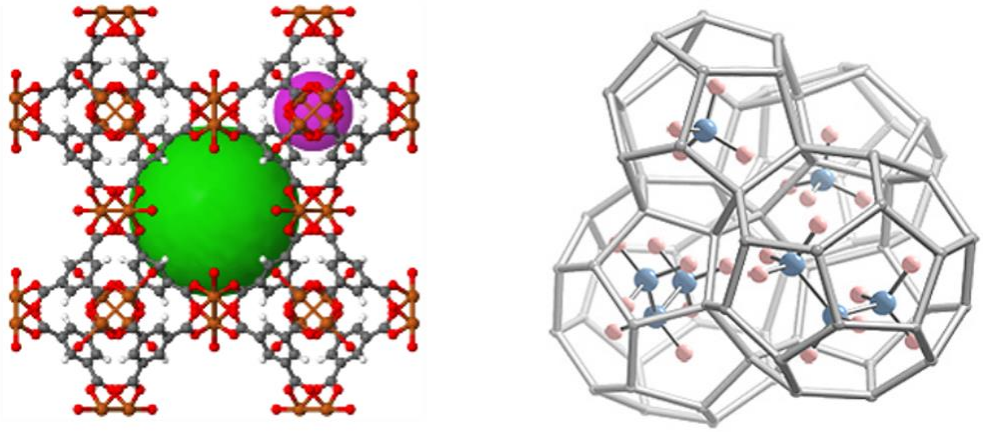

Figure 3.1 (Left) Structure of HKUST-1, which consists of 1,3,5-benzenetricarboxylic acid linking copper nodes the structure of HKUST-1. The green and pink spheres represent the size of the two internal pores where gas can be stored.[116] (Right) The most common methane hydrate, structure I. Water molecules hydrogen bond to form a cage around methane.[117] These depictions are not to scale.

Furthermore, the surface chemistry of HKUST-1 results in high methane [113,118] and water adsorption [119], in which the wettability of HKUST-1 increases the gas-to-water contact area and may promote gas hydrate growth in the pores as well as on the external surface. Furthermore, the high thermal conductivity of HKUST-1 due to the presence of copper within its framework may help to promote hydrate growth by removing the local heat of hydrate formation.

In this study we used a high pressure differential scanning calorimeter (HP-DSC) to follow methane hydrate growth in the presence of HKUST-1. The results demonstrate that the unique properties of HKUST-1 (i.e. large surface area, hydrophilicity, thermal conductivity) result in high water-to-hydrate conversion, suggesting that this MOF is an excellent methane hydrate growth promotor.

3.2 Experimental Methods

The synthesis and characterization of HKUST-1, the procedures used for the high pressure differential scanning calorimeter (HP-DSC), and the calculations of the obtained data are detailed in the following sections.

3.2.1 HKUST-1 Materials & Synthesis Procedure

The HKUST-1 synthesis approach used in this study follows the synthetic protocol reported elsewhere [120]. First, 3.5 g of copper(II) nitrate hydrate (98%, Sigma-Aldrich, $Cu(NO_3)_2 \cdot 2H_2O$) was mixed in 96 mL deionized water until completely dissolved. A separate solution containing 1.68 g of 1,3,5-benzenetricarboxylic acid (98%, Sigma-Aldrich) was mixed until dissolved in 96 mL of ethanol. Next, the two solutions were stirred together for 10 minutes before being placed in a Teflon-lined autoclave in a conventional oven. The solution was heated for 6 hours at 100°C and then cooled at a rate of 1°C/minute to 60°C. Once the oven reached 60°C, the autoclave was taken out of the oven and cooled to room temperature (~20°C). The cooled solution was centrifuged to separate out the HKUST-1 crystals, which were then washed by adding clean ethanol. The resulting solution was centrifuged to re-isolate the HKUST-1 crystals. This washing process was completed 3 times. The resultant material was then dried in an oven at 100°C.

3.2.2 HKUST-1 Characterization Methods

Powder X-ray diffraction patterns were collected using a Siemens Kristalloflex 810 diffractometer operating with Cu Kαl radiation at a wavelength of 1.54059Å with a voltage of 30 kV and current of 25 mA. The morphology of the HKUST-1 crystals before and after use in the HP-DSC was observed using a JOEL JSM-7000F field emission scanning electron microscope. A nitrogen isotherm at 77K was conducted to elucidate the surface area and pore volume using an ASAP 2020 porosimeter (Micromeritics, Norcross, GA, USA). For this analysis, all samples were degassed at 150°C for over 8 hours under vacuum. The same instrument and degas parameters were used to collect a methane isotherm at 273 K.

3.2.3 High Pressure Differential Scanning Calorimeter Measurements

The gas hydrate formation and dissociation behavior was observed using a high pressure differential scanning calorimeter (HP-DSC) VIIa (Setaram Inc.) with an operational pressure range of 0.1 MPa to 15.4 MPa and a temperature range of 228 K to 393 K, a resolution of 0.04

μW, and an overall precision of ±0.2K and ±25kPa. Figure 3.2 provides a schematic of the equipment [121].

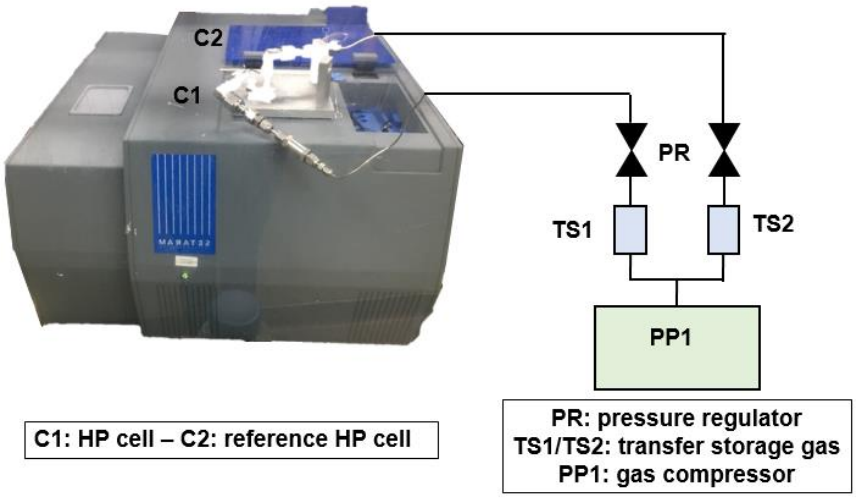

Figure 3.2 Schematic of the high pressure Differential Scanning Calorimeter (HP-DSC) VIIa (Setaram Inc.)

The sample was prepared by pipetting deionized water directly onto the dried sample to achieve a desired water ratio, further denoted as R_w. The HP-DSC tests were conducted as follows: first, the sample was placed into the DSC cuvette cell and was pressurized to the specified pressure. Then, the temperature was raised to 30℃ at a rate of 0.8℃/min. Next, the sample was cooled down to -15℃ at a rate of 0.8℃/min and then warmed back to 30℃ at a rate of 0.7℃/min. This cooling and heating cycle was repeated two more times, for a total of three times.

An additional HP-DSC test was conducted using the same sample preparation method as for that of the scan but a different HP-DSC cooling and heating procedure. The sample was heated to 30℃ at a rate of 0.5℃/min, held at 30℃ for 3 hours, cooled at a rate of 0.8℃/min to -10℃, held for 24 hours, and then heated to 30℃ at a rate of 0.3℃/min. This method is called an isothermal experiment.

3.2.4 Calculation of Water-to-Hydrate Conversion

The extent of water-to-hydrate conversion utilizes the heat flux measured by the HP-DSC for the endothermic peak. The endothermic hydrate dissociation peak is integrated and the

resulting value, given in J/g, is denoted as H_{diss}. This value is used to calculate the water-to-hydrate conversion using the following equation[121]:

$$Hydrate\ Conversion\ (\%) = 100 * \frac{H_{diss} *\ MW_{H2O} * n_{HYD}}{H_{HYD}} \quad (3.1)$$

The other variables in this equation represent the following:

Heat of dissociation of methane structure I hydrate (H_{HYD}) = 54.4 kJ/mol.[122]

Molecular weight of water (MW_{H2O}) = 18 g/mol.

Hydration number (n_{HYD}) = 5.9[121]

3.3 Results & Discussion

The following subsections detail the results from this study and the respective discussion.

3.3.1 HKUST-1 Effect on Hydrate Formation and Dissociation

Table 3.1 displays the key results from experiments that vary by the mass ratio of water to HKUST-1 (R_w). These results include: water-to-hydrate conversion, hydrate dissociation temperature, and amount of methane stored in the system relative to the amount of water present.

Table 3.1 The hydrate percent of water-to-hydrate conversion, hydrate dissociation temperature for different ratios of water to HKUST-1 by mass (R_w), and amount of methane stored per gram of water in the system.

Ratio H_2O to HKUST-1 (g/g)	Water to Hydrate Conversion (%)	Dissociation Temperature (°C)	CH_4 Stored to H_2O in System (mmol/g)
No HKUST-1	5.9±0.3%	10.5±0.1	0.55±0.03
0.39	20.5±0.8%	10.3±0.1	1.9±0.1
0.58	52.4±1.3%	10.5±0.1	4.9±0.1
0.97	62.3±0.7%	10.3±0.1	5.8±0.1
0.98	64.4±2.6%	10.5±0.1	6.0±0.2
0.98	67.5±0.7%	10.4±0.1	6.3±0.1
1.08	87.2±0.7%	10.7±0.1	8.1±0.1

[1]Experiments repeated 3 times to test reproducibility.

The addition of HKUST-1 increased the amount of water converted into hydrate by 3.5 to 14.8 times compared to a system with only water and methane. The dissociation temperature of each trial, in comparison to the experiment with only water and methane, do not show variances that exceed the equipment precision limits. The amount of methane stored relative to the amount of water in the system increased 3.5 to 14.7 times as compared to a system with only water and methane, which confirms that adding HKUST-1 promotes more methane storage. The HKUST-1 sample used in this study had a measured methane volumetric uptake of 0.89 mmol CH_4/g HKUST-1, whereas the hydrate formation experiment with the highest conversion, 87.2%, resulted in 9.8 times more methane stored relative to the mass of HKUST-1 in the system. The methane adsorption isotherm for the synthesized HKUST-1 is show in Figure 3.3.

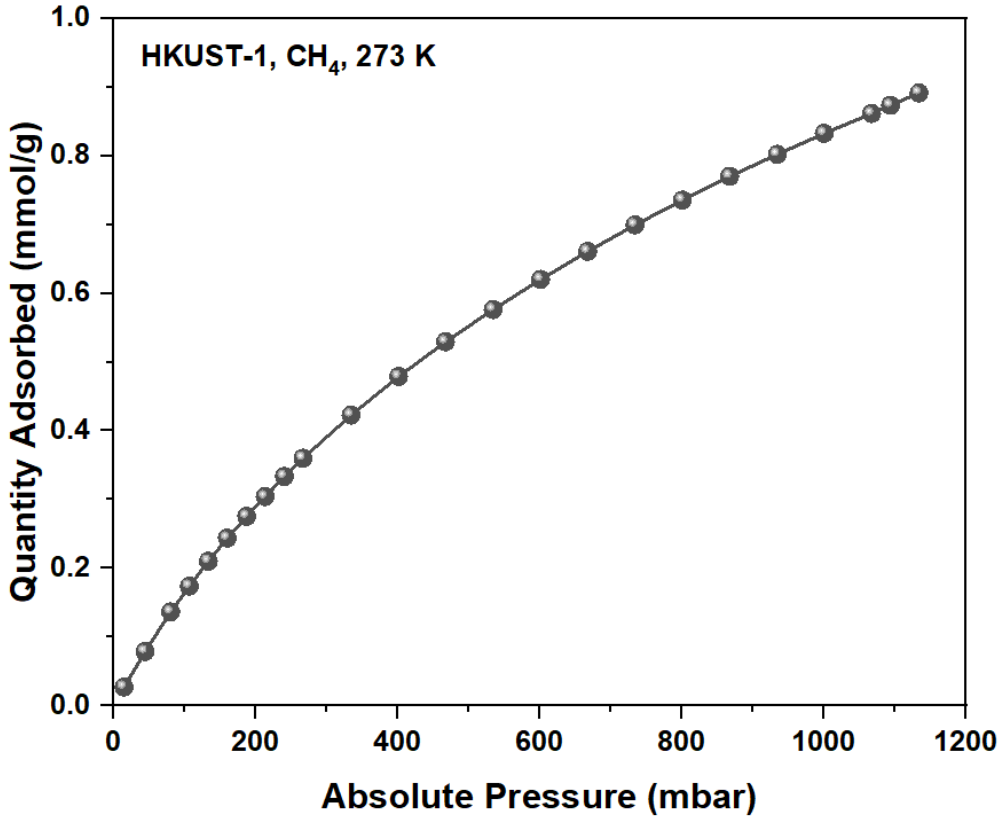

Figure 3.3 Total volumetric uptake of methane isotherm for HKUST-1, collected at 273K.

Notably, other studies in literature observed higher methane adsorption on dry HKUST-1 than that measured in this study, but the experimental conditions are not similar enough for a direct valid comparison [118,123]. Although still significant, the focus of this work is to use HKUST-1 as a gas hydrate promoter, as the promising results of hydrates for gas storage mentioned previously stem from hydrates exhibiting self-preservation (i.e. ice film forming around bulk hydrate that maintains hydrate stability after formation outside of the hydrate thermodynamic stability zone) [124]. Self-preservation allows for methane storage and transportation in hydrates at ambient pressures and low temperatures [125]. This independence from high pressure makes gas hydrates a desirable method of gas storage and fuel transportation, whereas dry HKUST-1 would need to be maintained at high pressure for methane storage.

In this study, the water-to-HKUST-1 mass ratio of 1.08 produced the highest water-to-hydrate conversion of 87.2% while the mass ratio of 0.39 only converted 20.5%. Overall, the amount of water converted to hydrate decreased with decreasing R_w, as shown in Figure 3.4.

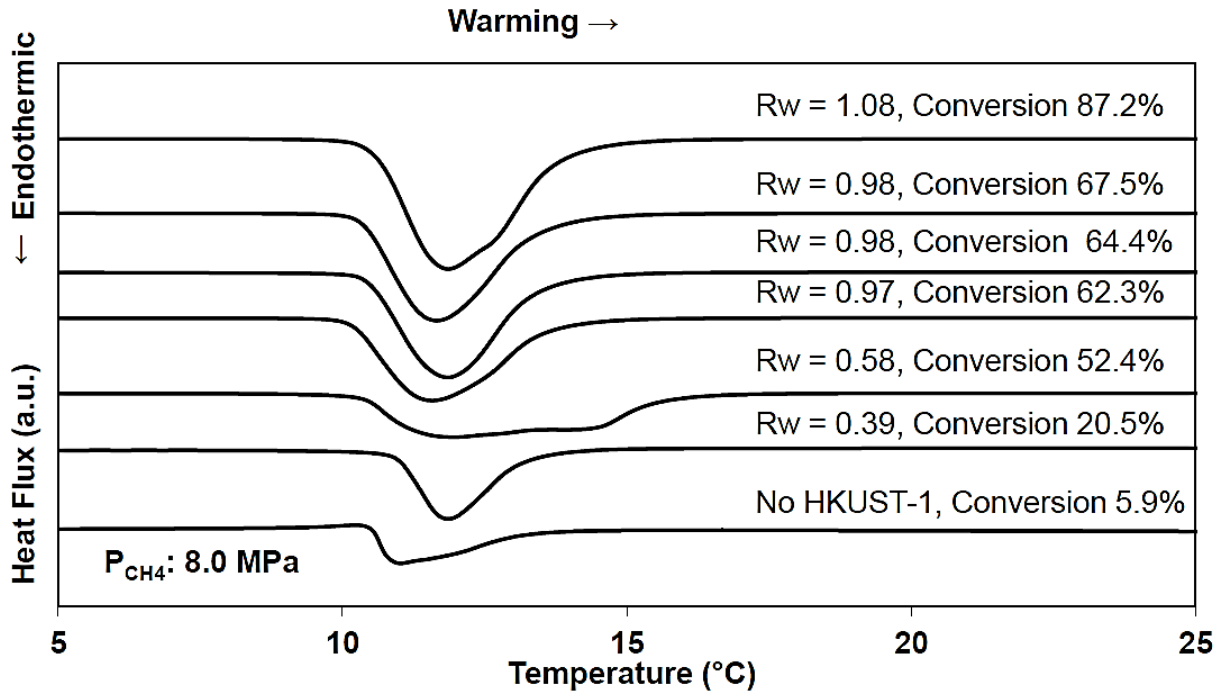

Figure 3.4 HP-DSC warming profiles of synthesized HKUST-1 and CH_4 at different water-to-HKUST-1 mass ratios (R_w) compared to profile without HKUST-1 and the respective water to hydrate conversion at 8.0 MPa. Scanning procedure of cooling from 30°C to -15°C and then heating back to 30°C. Each sample was subjected to 3 cycles of hydrate formation and dissociation to ensure repeatability.

The observed correlation of increased hydrate conversion with increasing R_w also arose in a study that conducted molecular dynamic simulations of hydrate formation with the MOF MIL-101 [91]. The authors of this study found that oversaturation of the MOF led to hydrate formation in the outer space of the MOF crystal; seemingly, hydrate growth was no longer constrained within the crystal's pores [91]. An additional postulation for this correlation stems from the water dispersion capabilities of HKUST-1. A study using ^{1}H MAS NMR to observe the water uptake of HKUST-1 concluded that the water molecules adsorb to the copper atoms in the structure; as more water molecules adsorb, faster exchange of water occurs throughout the structure [126]. This fast exchange leads to relatively efficient water dispersion over the surface of HKUST-1, providing a large gas-to-water interface. For a methane/water system, the hydrate film starts at the interface and then propagates into the water phase as methane diffuses through the hydrate layer [127]. Therefore, the experiment with higher water contact provided more water uniformly dispersed on the surface, allowing for more hydrate growth.

Although increased water dispersion increases the gas-to-water interface, the interaction between a MOF's surface and the water molecules also plays a significant role in hydrate nucleation. This relationship was explored in a study comparing hydrophilic MIL-100 (Fe) and hydrophobic ZIF-8 [87]. ZIF-8 converted almost all of the water to hydrate, whereas MIL-100 (Fe) only converted ~56% of the water on the external surface of MIL-100 (Fe) into hydrate [87]. The hydrophobicity of ZIF-8 prevented water from clogging the pores; instead, methane adsorbed to the surface, increasing the gas-to-water interface better than a hydrophilic surface does and thus promoting more hydrate formation [87]. The authors also postulated that the strength of the interaction between water and the surface of MIL-100 (Fe) interfered with the preferred orientation of water molecules for hydrate formation. One study supported this postulation by conducting molecular dynamics simulations on materials with different hydrophobicity and concluded that a hydrophilic surface changed the local ordering of water molecules in a way that hindered hydrate nucleation [128,129]. The extent of water adsorption of HKUST-1 (~400 mg/g) [130] is between that of MIL-100 (Fe) (560 mg/g) and ZIF-8 (18 mg/g), suggesting that the hydrophilicity of HKUST-1 may limit the hydrate growth.

In literature, other materials have shown higher water-to-hydrate. One example is silica sand, in which an experiment performed at 8.0 MPa and a constant 4°C resulted in a water-to-

hydrate conversion of 94.7% with an induction time of 34.7 hours [131]. Another example is a study on activated carbon, which found that at 8.0 MPa, the highest conversion 98.6%[82]. Our work has similarly high conversion for the experiment conducted with a water to HKUST-1 mass ratio of 1.08, as it resulted in a conversion of 87.2%. Note that although many other materials showed relatively high water-to-hydrate conversion, most of those studies were conducted at different experimental conditions, such as different pressures[132], and/or with chemical additives, such as THF [99], and therefore a direct comparison is challenging.

Another factor in the successful gas hydrate promotion may stem from the thermal conductivity of the HKUST-1 structure. A study on the transport of heat generation from gas adsorption to the surface of HKUST-1 using molecular dynamics simulations found that this heat dissipated quickly throughout the structure [115]. Similarly, the exothermic heat given off by gas hydrate formation would move away from the local area, promoting both hydrate nucleation and growth.

A brief investigation of the effects of HKUST-1 was performed via an isothermal test conducted in the HP-DSC. Figure 3.5 in the Supporting Information shows the change in heat flux versus time for a system with only H_2O and CH_4 versus a system with HKUST-1, H_2O and CH_4 where both experiments were pressurized at 8.0MPa and held at -10°C for 24 hours. The system without HKUST-1 shows a prominent hydrate and/or ice formation peak starting at approximately 4 hours and 15 minutes after the system reach -10°C. In contrast, the system with HKUST-1 started forming hydrate and/or ice approximately 10 minutes before the system reached -10°C. Therefore, the presence of HKUST-1 decreased the induction time by 4 hours and 25 minutes, making the addition of HKUST-1 to the system kinetically favorable. Additionally, the heat flux profile in Figure 3.5 shows ice and hydrate dissociation for the system containing only H_2O and CH_4 while the system with HKUST-1, H_2O and CH_4 only shows dissociation of hydrate. This further observation confirms our statement that HKUST-1 promotes hydrate formation.

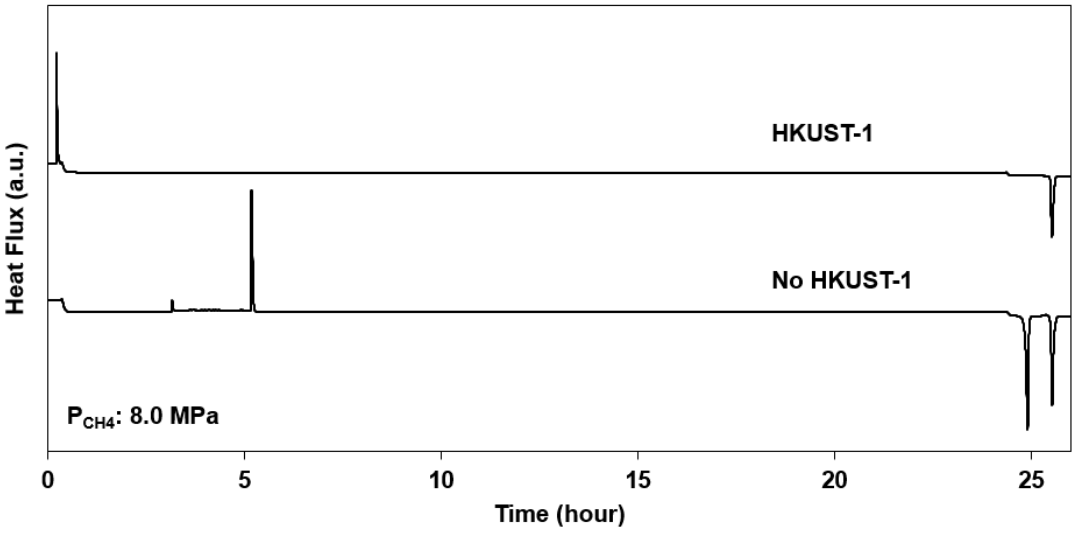

Figure 3.5 HP-DSC cooling and warming profile for isothermal test at 8.0 MPa with only H_2O and CH_4 (bottom line) and for a test with HKUST-1, H_2O and CH_4 with a water to HKUST-1 mass ratio (R_w) of 0.87 (top line).

3.3.2 Effects of Hydrate Formation/Dissociation on HKUST-1 Pores

The HP-DSC experiment conducted with an R_w of 0.39 is close to the saturation point of HKUST-1 reported in literature (~400mg/g) [130], and thus gives insight on the location of hydrate formation. The water-to-hydrate conversion in the system with the R_w of 0.39 is only 3.5 times higher than the conversion in a system with only water and methane. This relatively poor improvement as compared to the R_w of 1.08 (87.2% conversion) may be caused by the rapid and uniform water dispersion on the crystal surface leaving little water left for hydrate formation. The low conversion is not accompanied by endothermic peak at 0°C, which corresponds to ice dissociation. The absence of this peak indicates that the pores are playing an influential role in the process of hydrate formation and dissociation.

The large pore cavity (1.4 nm) could potentially accommodate most common methane hydrate, structure I, which has a lattice size of approximately 1.2 nm [11,114]. However, the limiting pore aperture of HKUST-1 of ~1.0 nm would make this potential hydrate allocation within the pores quite challenging [114]. Therefore, pore confinement may potentially lead to increased gas hydrate formation and/or sites for nucleation without containing methane hydrates within the pores.

Powder X-ray diffraction (XRD) and nitrogen isotherms were collected to further investigate whether hydrate formation took place only on the outer surface of the HKUST-1

crystal, or both on both the surface and in the pores. Figure 3.6 shows the powder XRD patterns for the HKUST-1 crystals before and after hydrate formation and dissociation in the HP-DSC in comparison to the simulated HKUST-1 pattern. The XRD peak positions of the experimental patterns agree well with the simulated XRD pattern, confirming the formation HKUST-1 crystalline structure.

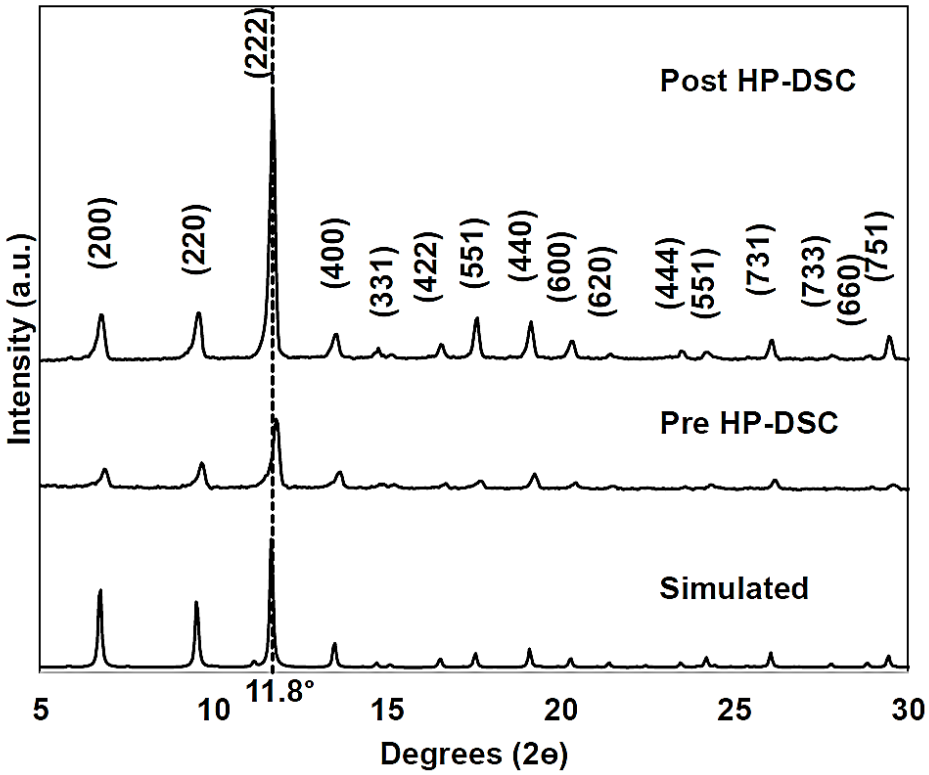

Figure 3.6 Powder XRD pattern of synthesized HKUST-1 crystals before and after hydrate formation and dissociation in the HP-DSC. Simulated pattern shown for comparison. The dashed line shows the 11.8° 2θ angle.

The post HP-DSC pattern in Figure 3.6 shows a slight 2θ shift of 0.1° to the left relative to the pre HP-DSC pattern, denoted with a dashed vertical line. Previous studies on microporous crystals concluded that a shift to the left indicates an expansion of the unit cell [33]. The nitrogen isotherm at 77K confirmed pore expansion, as shown in the inset of Figure 3.7.

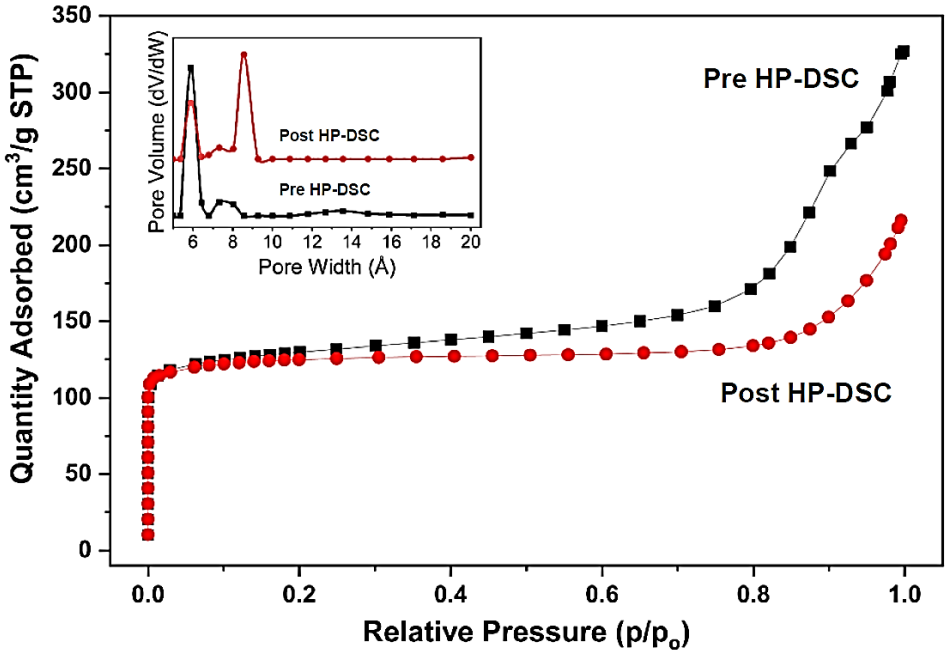

Figure 3.7 Nitrogen adsorption isotherms at 77K for a sample of HKUST-1 before and after hydrate formation/dissociation. The pore volume and pore width for the two samples is shown in the inset.

The most prominent pore in the HKUST-1 sample before the HP-DSC was 0.59 nm, while the sample after hydrate formation and dissociation was 0.86 nm. Initially, the pre HP-DSC sample had a large pore size range of ~0.7 to 0.85 nm with a the most prominent size being ~0.73 nm. After the HP-DSC, the large pore size shifted right to a range of ~0.7 to 0.93 nm and a primary large pore size of ~0.86 nm. The size of the typical methane hydrate, structure I, is 1.2 nm, which is too big for the HKUST-1 pores.

A plausible reason for the expansion is formation of ice in the pores. The lack of an endothermic peak at 0°C for these tests further supports the hypothesis that if ice formation occurs, it is in the pores while hydrates form on the outer surface. The hydrate layer on the external surface of the HKUST-1 crystal may prevent the ice from melting until the hydrate melts. Another explanation may be that some of the water adsorbed by HKUST-1 in the pores may stay as a free liquid water phase. This would account for why only some of the pores with a diameter of 0.6 nm increased in size, as the pores that did not increase may have held liquid water throughout the experiment.

To explore ice formation versus trapped liquid water, a test was conducted with a mass ratio of water to HKUST-1 of 1.05 at ambient pressure. Approximately 56.4% of the water in the

system converted into ice, insinuating that the remaining 43.6% of the water stayed in a liquid phase. Due to the HKUST-1 material's high water affinity, the liquid water most likely occupied the pores of the crystal. This phenomena was studied in silica micropores and found that liquid water phase could stay thermodynamically stable down to ~235K [133]. Thus, both ice and water are likely filling the pores while hydrate formation occurs only at the surface of HKUST-1 crystals. Previous studies on methane hydrate formation in MOFs support the preferential formation of methane hydrates form on the crystal surface.[87,88,91]

3.3.3 HKUST-1 Structural Integrity after Hydrate Formation and Dissociation

For practical gas storage applications using HKUST-1, the material must maintain its integrity throughout multiple uses. Figure 3.8 shows the cooling and warming profiles for the same HKUST-1 sample undergoing hydrate formation and dissociation for three cycles that occurred consecutively. The minimal deviation in conversion (±0.7%) and equilibrium temperature (±0.1°C) are well within the bounds of precision of the HP-DSC.

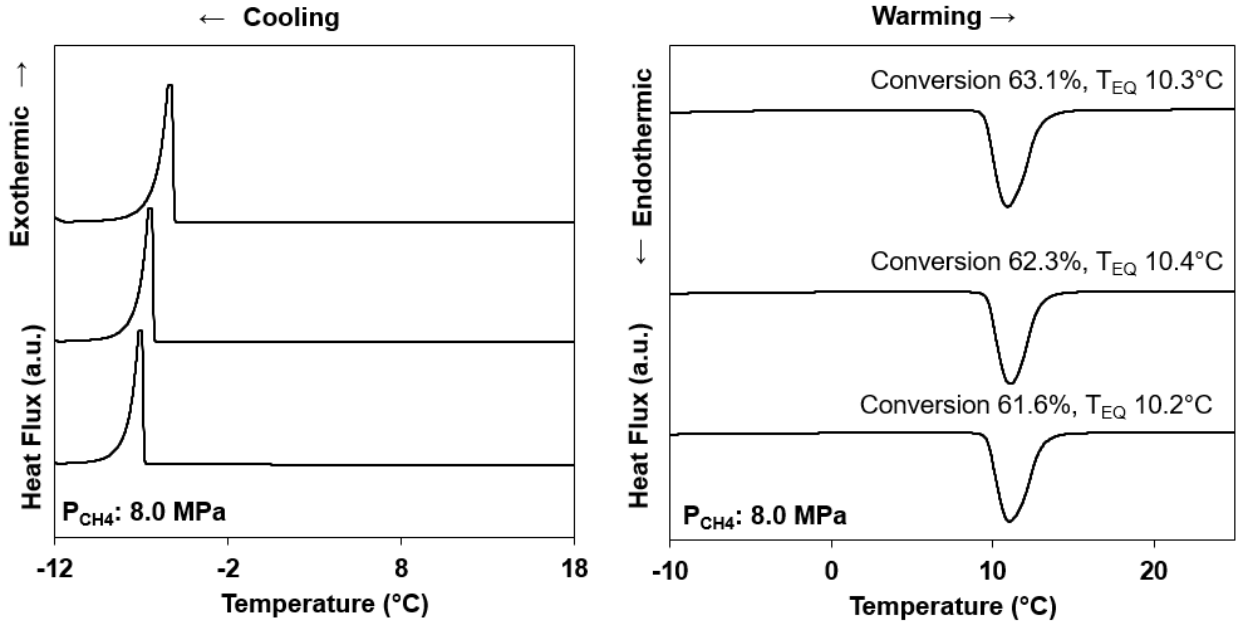

Figure 3.8 HP-DSC cooling (left) and warming (right) profiles of synthesized HKUST-1 and CH_4 at water-to-HKUST-1 mass ratios (R_w) of 0.97 at 8.0 MPa for 3 cycles. For the 3 cycles, the extent of hydrate conversion is within ±0.7% and the equilibrium temperature (T_{EQ}) is within ±0.1°C.

An interesting observation notable in the XRD pattern in Figure 3.6 is that the sample underwent gas hydrate formation and dissociation (post HP-DSC). This sample displays different

intensity ratios for some of the peaks, compared with the intensity ratios of the sample before hydrate formation and dissociation (pre HP-DSC). For instance, after subjecting HKUST-1 to several formation and dissociation cycles, the pattern clearly shows a change in the preferential plane exposure of the plane (222) over the other crystallographic planes. One possible reason for the overall change in intensity ratios is that a higher concentration of crystallites are present after gas hydrate formation, an observation noted in other studies of crystalline materials [134,135].

The nitrogen isotherm at 77K, shown in Figure 3.7, shows evidence of densification as the pore volume decreased from 0.50 to 0.33 cm^3/g. The most likely causes for the densification are exposure to water and high pressure. Previous studies correlated the decrease in the 200/222 and 220/222 ratios with the presence of water densifying the structure [136,137], a change observed in this work as the 200/222 and 220/222 peak intensity ratios decreased by a factor of 0.72 and 0.56, respectively. As for the high pressure postulation, one particular study found that when subjecting HKUST-1 to high pressure the structure retained its crystallinity up to 200 MPa, which is 25 times higher than the pressure this study used in the HP-DSC experiments [138]. Therefore, the most probable reason for the densification is exposure to water during the HP-DSC experiments, since the pressures used in this study were insufficient to cause significant densification. These studies indicate that the changes to HKUST-1 structure (i.e. pore volume, pore diameter, and degree of crystallinity) in this work was not due to the high pressure nor low temperature conditions of the HP-DSC, but instead due to the presence of water. Overall, the crystalline structure of HKUST-1 is preserved after hydrate formation and dissociation, as indicated by Figure 3.6, and therefore no phase change occurred.

Figure 3.9 shows representative SEM images of the HKUST-1 sample before and after hydrate formation and dissociation.

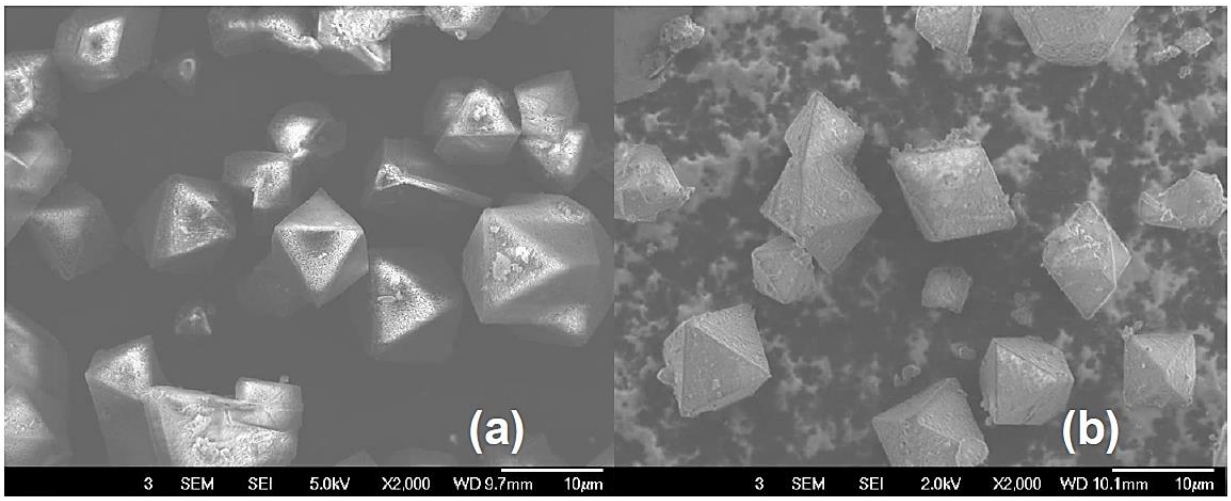

Figure 3.9. Representative SEM images of synthesized HKUST-1 crystals (a) before and (b) after hydrate formation and dissociation.

These images show that the crystal retained its well-faceted bipyramid octahedral morphology. Further analysis verified that the crystals retained a relatively narrow size distribution and average particle size of 9.30±2.68 μm and 8.01±1.32 μm, respectively. The relatively large overall size of the HKUST-1 crystal may be one reason why the observed surface area (498 m^2/g) was lower than the typically reported surface areas (~1000 m^2/g) [112,113]. The very small particles visible around the HKUST-1 crystals in Figure 3.9 for the sample after hydrate formation and dissociation in the HP-DSC (b) may result from the decomposition of the material due to the presence of water, as found by a study that took SEM images of HKUST-1 exposed to water over a time period of 28 days [139]. These particles and the maintained morphology for the post HP-DSC align with the conclusion of a study, which found that the decomposition due to water starts at the crystal surface [135]. Multiple studies found that an ethanol solvent treatment can reverse decomposition of HKUST-1, as ethanol plays a vital role in the kinetics of the synthesis of HKUST-1; thus, an ethanol treatment could increase the longevity of HKUST-1 [136,137].

The work completed in this study will aid in future studies utilizing HKUST-1 in aiding in hydrate growth, particularly studies looking at the scalability of HKUST-1 to larger volumes. Scalability is the key to confirming whether or not HKUST-1 and hydrates could be potentially implemented as a commercial methane storage technology. Since the synthesis of HKUST-1 is already commercially developed, then the focus of scalability would be the hydrate component. The process must address the mass transfer (e.g. formation of hydrate at the interface of water

and gas forms a gas diffusion barrier) and heat transfer (e.g. local heat of hydrate formation inhibiting further hydrate growth) challenges mentioned previously. The complexity of different apparatus configurations, crystal concentrations, and operating conditions makes scalability worth a future in-depth study.

3.4 Conclusions

In summary, HKUST-1 was demonstrated to increase the water-to-hydrate conversion from 5.9% to as high as 87.2% for the purpose of promoting gas hydrate growth for methane gas storage. The increased conversion stems from the material's large surface area and unique surface chemistry of the material. Specifically, the large surface area increased the gas-to-water interface, reducing the transport limitation of a hydrate film forming between phases. The structure's hydrophilicity led to dispersed water molecules across its surface, which increased the gas-to-water contact area but also ordered the water molecules in a way that may have limited or prohibited hydrate formation. The high thermal conductivity of HKUST-1 due to the presence of copper nodes within its framework promoted hydrate growth by removing the local heat of hydrate formation. These properties led to a reduction of 4.4 hours in induction time when HKUST-1 was added to the system. Investigation into the crystal integrity over the course of multiple hydrate formation and dissociation cycles showed that, the HKUST-1 crystal structure was preserved. The desirable methane hydrate growth and potential for long-term stability of the HKUST-1 crystal structure makes this MOF, HKUST-1, a highly promising promoter for gas hydrate formation for methane storage applications.

CHAPTER 4
METHANE HYDRATE GROWTH PROMOTED BY MICROPOROUS ZEOLITIC IMIDAZOLATE FRAMEWORKS ZIF-8 & ZIF-67 FOR ENHANCED METHANE STORAGE

Modified from: S. Denning, A.AA. Majid, J.M. Lucero, J.M. Crawford, M.A. Carreon, C.A. Koh*, "Methane Hydrate Growth Promoted by Microporous Zeolitic Imidazolate Frameworks ZIF-8 and ZIF-67 for Enhanced Methane Storage" ***ACS Sustainable Chemistry & Engineering 2021,*** 9, 27, 9001-9010

This work studied the effects of two zeolitic imidazolate frameworks, ZIF-8 and ZIF-67, on methane hydrate. The chapter contains detailed experimental methods and analysis, of which are published in ACS Sustainable Chemistry & Engineering 2021, 9, 27, 9001-9010.

4.1 Comparison of Zeolitic Imidazole Frameworks ZIF-8 and ZIF-67 as Methane Hydrate Growth Promoters

By combining the methane storage capabilities of porous materials with gas hydrates, there can be a synergistic result where the amount stored with the combination of both hydrates and the porous materials is more than that of hydrates or porous materials on their own.[81,90] Metal-organic frameworks (MOFs) are a particularly interesting class of porous materials, as they are chemically diverse in composition, have large surface areas, and exhibit tunable porosity.[140] As far as the authors are aware, the MOFs studied as methane hydrate promoters include MIL-53,[88] MIL-53(Al),[89] ZIF-8,[87,89,90] HKUST-1,[26,89] MIL-101,[91] MIL-100(Fe),[87] Cr-soc-MOF-1,[81] and Y-shp-MOF-5.[81] These studies showed promising results for the application of MOFs as methane hydrate promoters, with more details of the results show in Table 4.1.

Table 4.1 Overview of studies that used metal organic frameworks (MOFs) as methane hydrate growth promoters.

Type of MOF	Comments	Ref.
MIL-53(Al)	Recorded pressure and temperature in a reactor. Measured hydrate equilibrium curve with the material present, matches that of bulk water. At 274.15K and pressures 0 to 10 MPa, less methane stored in system with MIL-53 & hydrates versus a system with dry MIL-53.	89

Table 4.1 continued.

MIL-100(Fe)	Methane high pressure adsorption. Water-to-hydrate conversion 56% at 4 MPa and 275K.	[87]
MIL-53	Low-temperature synchrotron high-resolution powder diffraction. Hydrates form in meso/macro pores. Equilibrium curves measured.	[88]
ZIF-8	Recorded pressure and temperature in a reactor. Measured hydrate equilibrium curve with the material present, matches that of bulk water. At 274.15K and pressures 0 to 10 MPa, ZIF-8 combined with gas hydrates increased the amount of methane stored relative to dry ZIF-8.	[89]
	Methane high pressure adsorption, inelastic neutron scattering, and synchrotron x-ray powder diffraction. Nearly 100% water-to-hydrate conversion.	[87]
	Measured pressure drop. The net methane stored in the material with hydrates is 56% more than that of the dry material at 269.15K and 2.85 MPa.	[90]
MIL-101	Microsecond molecular dynamics simulations. Methane hydrate forms preferentially on outer surface. Hydrophilicity causes water to block cavities, decreasing the amount of methane in cavities as the water content increases.	[91]
Cr-soc-MOF-1	High pressure methane isotherms 275K, 0 to 10 MPa. At 10 MPa, this material combined with hydrates stores 50% more methane as compared to the dry material. Conversion of 66%	[73]
Y-shp-MOF-5	The addition of this material did not increase the overall amount of methane stored relative to how much the dry material can store.	[73]
HKUST-1	Measured heat consumed/released using high pressure differential scanning calorimeter. Water-to-hydrate conversion as high as 87.2% at 8.0 MPa.	[26]

The studies on HKUST-1[26] and ZIF-8[87] reported high (>80%) water-to-hydrate conversion, whereas the other studies focused primarily on the amount of methane consumed by

the hydrate and MOF. Of these studies, very few look at the recyclability and structural integrity of the metal organic frameworks after methane hydrate formation and dissociation, with the notable exceptions of two studies on ZIF-8[87,89] and previous work by our group with HKUST-1[26]. Both ZIF-8 studies evaluated structural changes after only a single cycle of hydrate formation and dissociation, whereas our work with HKUST-1 evaluated these changes after three cycles. Therefore, more research is needed to determine the long-term viability of metal organic frameworks as methane hydrate promoters.

The porous materials relevant to this study are metal-organic frameworks; more specifically, the materials are zeolitic imidazolate frameworks (ZIF), which is a subclass of MOFs. ZIFs contain both inorganic (metal ion) and organic (imidazolate linker) components, and the framework is composed of tetrahedral structural units, like that of zeolites.[141] In this study, two microporous zeolitic imidazolate frameworks were chosen: ZIF-8 and ZIF-67. To the best of our knowledge, no studies have been documented on ZIF-67 as a methane hydrate promoter. Since these ZIFs are isostructural, the study of both, would be helpful to better understand the role (if any) of the metal core in methane gas hydrate formation. ZIF-8 and ZIF-67 exhibit the same sodalite topology with imidazole linkers and zinc or cobalt metal centers, respectively[28]. Both ZIFs exhibit surface areas above 1000 m^2/g, pore volumes of ca. 0.6 cm^3/g, and internal pore diameters of 1.2 nm[142–146]. An illustration of the representative structures of gas hydrate structure I, ZIF-8 and ZIF-67 are given in Figure 4.1(a), Figure 4.1(b) and Figure 4.1(c), respectively.

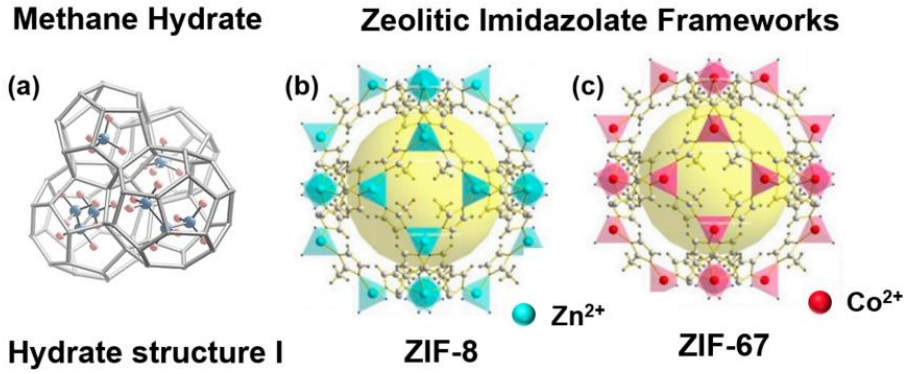

Figure 4.1 Illustration of (a) methane hydrate structure I with a unit cell size of 1.2 nm, and the two zeolitic imidazolate frameworks of sodalite structure (b) ZIF-8 and (c) ZIF-67. The yellow spheres represent the internal pore, which has a diameter of 1.2 nm.[117,147] Not to scale.

For ZIF-8 and ZIF-67, the large surface areas and the internal pore diameter are advantageous for hydrate formation. The large surface area generates a large gas-to-water contact area, both externally and internally due to the pores. The diameter of the ZIFs cavity (1.2 nm) is approximately the same size of a methane hydrate structure I unit cell (1.2 nm), thus the pores could provide more interfacial area for gas hydrate formation. The confined space of the pore also can promote hydrate growth due to the pore's effect on the water activity, and this formation can act as a site for hydrate nucleation.[96,99]

These porous materials also have high methane adsorption capacity, with ZIF-8 reaching up to ~8 mmol/g at 80 bar, which provides a source of methane for hydrate formation.[89,148] The hydrophobicity of the ZIFs also plays an important role, as a hydrophobic surface positively effects the water ordering necessary for hydrate cages to begin to form.[149] According to a study that tested the water stability of both ZIF-8 and ZIF-67, these ZIFs were stable in water to pressures as high as 800 bar, which indicates that these materials should maintain crystal integrity during and after the wet, high pressure environment in hydrate formation and dissociation experiments.[150]

In this study, the effect of ZIF-8 and ZIF-67 on methane hydrate growth was investigated using a high pressure differential scanning calorimeter (HP-DSC). Two key findings confirm that these microporous crystals are exceptional methane hydrate growth promoters: 1) high water-to-hydrate conversion, and 2) significant reduction in hydrate nucleation induction time. These encouraging results are most likely due to the ZIFs' large surface areas, hydrophobicity, water stability, and mechanical stability.

4.2 Experimental Methods

The synthesis method for ZIF-8 and ZIF-67 are detailed below along with the characterization methods, the operating procedure for the high pressure differential scanning calorimeter (HP-DSC) and the respective calculations.

4.2.1 ZIF-8 & ZIF-67 Materials & Synthesis Procedure

ZIF-8 and ZIF-67 were synthesized via microwave heating. This method has been employed for synthesis as it produces small crystals with a narrow size distribution, as observed in studies that used this method to synthesize other porous crystals, such as MOFs,[151,152] zeolites,[67] oxides [68] and porous organic cages.[155]

The procedure for synthesizing ZIF-8 is adapted from elsewhere.[142] First, 0.10 g of zinc acetate hexahydrate (Sigma-Aldrich, >98%), was dissolved in 10 g of deionized water. Next, 0.41 g of 2-methylimidazolate (Aldrich, 99%) was added to the solution, which was stirred for 1 hour. The resulting solution was put in a 100 cm^3 Teflon-lined XP1500 vessel with a thermocouple inside. The vessel was then placed in a CEM Mars 5 microwave and heated to 120°C for 30 minutes with a ramp time of 5 minutes at 100% of 400W power, with a ramp time of 5 minutes. Once the vessel cooled naturally to room temperature, the solution was washed with deionized water and ethanol via centrifugation for 5 minutes at 3800 rpm. The resulting crystals were dried at 80°C for 24 hours.

The procedure for synthesizing ZIF-67 is similar to that of ZIF-8, with modifications from elsewhere.[156] The precursors employed to synthesize ZIF-67 are 2-methylimidazolate (Aldrich, 99%), cobalt(II) nitrate hexahydrate (Sigma-Aldrich, >98%), and deionized water. First, 5.50 g of 2-methylimidazolate was dissolved into 20 g of deionized water. Second, in a separate beaker, 0.45 g of cobalt(II) nitrate hexahydrate was dissolved in 3 g of deionized water. Next, the two solutions were mixed together for 1 hour. The combined solution was put in a 100 cm^3 Teflon-lined XP1500 vessel with a thermocouple inside. The vessel was then placed in a CEM Mars 5 microwave and heated to 120°C for 30 minutes at 100% of 400W power, with a ramp time of 5 minutes. Once the vessel cooled naturally to room temperature, the solution was washed with deionized water and methanol via centrifugation for 5 minutes at 3800 rpm. The resulting crystals were dried at 80°C for 24 hours.

4.2.2 ZIF-8 & ZIF-67 Characterization Methods

To test the structural integrity of ZIF-8 and ZIF-67 crystals, a baseline was taken before subjecting the materials to the formation and dissociation of gas hydrates and then one was taken after. To this end, a Siemens Kristalloflex 810 X-ray diffractometer was used to gather powder x-ray diffraction patterns of the microporous crystals. The diffractometer used Cu Kαl radiation operating at a wavelength of 1.54059Å, accompanied by a current of 25 mA and a voltage of 30 kV. The morphology of each material before and after hydrate formation and dissociation was inspected using a JEOL JSM-7000F field emission scanning electron microscope. An ASAP 2020 porosimeter (Micromeritics, Norcross, GA, USA) was used to collect nitrogen isotherms at -196°C, after the sample was degassed for 8 hours at 200°C under vacuum. Surface areas were calculated using the Brunauer-Emmet-Teller (BET) method following the criterion described by

Rouquerol *et al*.[157] Pore size distributions were calculated using non-local density functional theory (NLDFT) for nitrogen on carbon slit pores. Pore volumes were calculated at P/Po = 0.9. Methane isotherms were collected at 0°C using the same ASAP 2020 porosimeter and employing similar degas conditions as the nitrogen isotherms.

4.2.3 High Pressure Differential Scanning Calorimeter Measurements

A high pressure differential scanning calorimeter (HP-DSC) VIIa Seteram Inc. was used to investigate hydrate formation and dissociation. The HP-DSC operated within these criteria: a resolution of 0.04 μW; a temperature range of 228K to 393K, with a precision of ±0.2K; and a pressure range of 0.1 MPa to 15.4 MPa, with a precision of ±25kPa. The schematic of the HP-DSC is given in Figure 4.2.

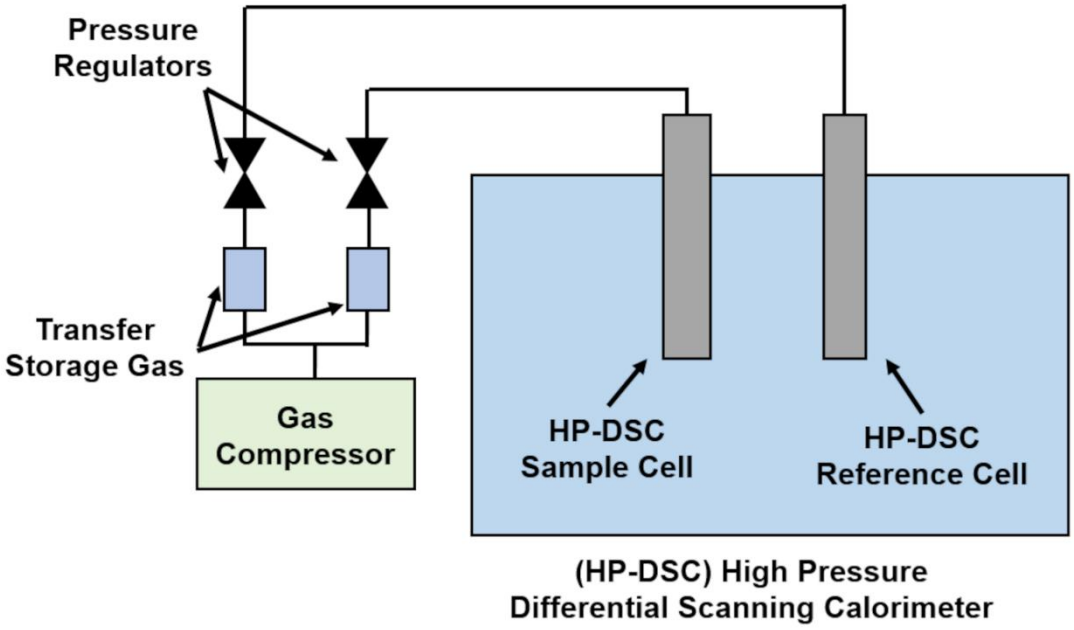

Figure 4.2 Schematic of the high pressure differential scanning calorimeter (HP-DSC).

The employed methods are similar to our previous work.[26] Each sample was prepared by loading the cuvette HP-DSC cell with a specified amount of deionized water, and then adding the dry crystalline material. The ratio of the water's mass relative to the material's mass is denoted by R_w and shown in the following equation:

$$R_w = \frac{\text{mass of water}}{\text{mass of ZIF}} \tag{4.1}$$

The sample was loaded into the HP-DSC and then pressurized with methane gas (Matherson, 99.99%). Two procedures were used for this research: scanning and isothermal. Each procedure was conducted at 8.0 MPa. Note that all of the HP-DSC experiments are performed *in-situ*.
The scanning procedure started by raising the temperature of the system to 30℃ at a rate of 0.5℃/min. The system was held at 30℃ for 3 hours. Next, the system was cooled at a rate of 0.3℃/min to -30℃, then immediately warmed to 30℃ at a rate of 0.3℃/min. To ensure reproducibility and crystal structure integrity, the cooling and heating process was repeated twice more, for a total of 3 times.

The isothermal procedure started by raising the temperature of the system to 30℃ at a rate of 0.5℃/min. The system was held at 30℃ for 3 hours. Next, the system was cooled at a rate of 0.8℃/min to -15℃, then held at that temperature for 24 hours. Then, the system was warmed back up to 30℃ at a rate of 0.3℃/min. This process was repeated once, for a total of 2 times.
For both the scanning and isothermal experiments, the heat flux profiles generated by the HP-DSC were collected. The appearance of peaks corresponded to either ice or hydrate formation or dissociation. The peak location indicates the time and temperature for hydrate formation/dissociation. The area under the peaks corresponds to the magnitude of the amount of hydrate and/or ice formed/dissociated in the system.

4.2.4 Water-to-Hydrate Conversion Calculation

The water-to-hydrate conversion in the HP-DSC system was calculated via the following equation:[26,121]

$$\text{Hydrate Conversion (\%)} = 100 * \frac{H_{diss} * MW_{H2O} * n_{HYD}}{H_{HYD}} \quad (4.2)$$

H_{diss} is the heat flux for the hydrate dissociation endothermic peak, as measured by the HP-DSC. MW_{H2O} is the molecular weight of water (18 g/mol). n_{HYD} is the hydration number (5.9).[121] H_{HYD} is the known value of the heat of dissociation for a methane structure I hydrate (54.4 kJ/mol).[122]

4.3 Results & Discussion

The experimental results their respective discussion is detailed in the following subsections.

4.3.1 Influence of ZIF-8 & ZIF-67 on Water-to-Hydrate Conversion

The zeolitic imidazolate frameworks ZIF-8 and ZIF-67 displayed remarkable performance as methane hydrate growth promoters. The measurements and calculations from the high pressure differential pressure scanning calorimeter (HP-DSC) experiments for a system with only water and with four systems with different water to microporous material mass ratios (R_w) are summarized for ZIF-8 in Table 4.2 and ZIF-67 in Table 4.3.

Table 4.2 Water-to-hydrate conversion, dissociation temperature, and methane stored relative to the amount of water in the system for a system with no microporous material and four water to microporous material mass ratio (R_w) for the zeolitic imidazolate frameworks ZIF-8.

ZIF-8			
Mass Ratio H_2O to ZIF-8 (g/g)	Conversion (%)	Dissociation Temperature (°C)	CH_4 Stored to H_2O in System (mmol/g)
No ZIF-8	4.5	11.5	0.42
0.16	81.1	8.2	7.5
0.38	85.6	8.5	7.9
0.54	83.8	7.9	7.8
1.01	80.0	8.1	7.4

Values correspond to the third cycle of hydrate formation and dissociation

Table 4.3 Water-to-hydrate conversion, dissociation temperature, and methane stored relative to the amount of water in the system for a system with no microporous material and four water to microporous material mass ratio (R_w) for the zeolitic imidazolate framework for ZIF-67.

ZIF-67			
Mass Ratio H_2O to ZIF-67 (g/g)	Conversion (%)	Dissociation Temperature (°C)	CH_4 Stored to H_2O in System (mmol/g)
No ZIF-67	4.5	11.5	0.42
0.16	75.5	8.7	7.0
0.33	86.4	8.8	8.0
0.50	87.7	8.9	8.1
0.82	83.6	8.6	7.7

Values correspond to the third cycle of hydrate formation and dissociation

The warming heat flux profiles for these experiments are given in Figure 4.3.

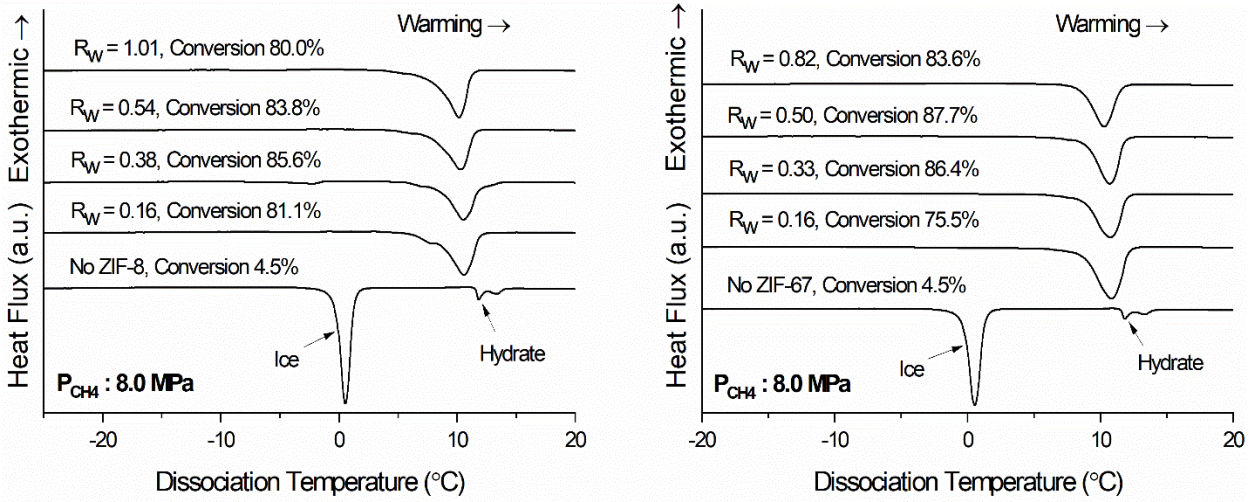

Figure 4.3 Warming HP-DSC heat flux profiles for ZIF-8 (left) and ZIF-67 (right), with respective values for crystal to water mass ratio (R_w) and water-to-hydrate conversion conducted at 8.0 MPa.

Full cooling and warming heat flux profiles for ZIF-8 and ZIF-67 are given in Figure 4.4, with the corresponding temperature profile of the HP-DSC system overlaid.

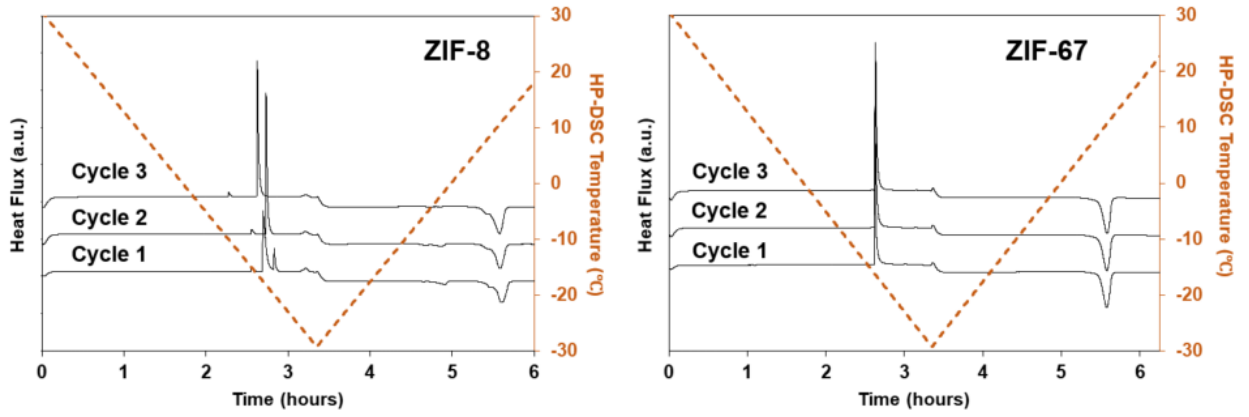

Figure 4.4 Full HP-DSC cooling and warming profiles for 3 consecutive cycles of hydrate formation and dissociation for ZIF-8 (left) and ZIF-67 (right). The orange dashed line represents the temperature of the HP-DSC system.

The addition of either ZIF-8 or ZIF-67 dramatically increased water-to-hydrate conversion as compared to a system without any porous material. The water-to-hydrate conversion ranged from 80.0-85.6% for ZIF-8 and from 75.5-87.7% for ZIF-67 for different

water to ZIF mass ratios. A system with ZIF-8 increased the water-to-hydrate conversion by as much as 15.3 times, raising it from 4.5% to 85.6%. A system with ZIF-67 increased water-to-hydrate conversion by as much as 15.7 times, from 4.5% to 87.7%. Therefore, the addition of ZIF-8 and ZIF-67 increased the amount of methane stored relative to the amount of water in the system from 0.42 mmol/g to highs of 7.9 mmol/g and 8.1 mmol/g, respectively. The amount of methane stored accounts only for the amount that is captured in the hydrate as determined using the methane structure I hydration number and heat flux from the respective HP-DSC experiments, and does not include the amount of methane potentially adsorbed on the microporous crystal.

The high water-to-hydrate conversion seen is this study most likely stems from physical and chemical properties of the two ZIFs. The high surface area of ZIF-8 (1052 m^2/g) and ZIF-67 (1585 m^2/g) increased the gas-to-water contact area, thus reducing the gas diffusion barrier caused by a hydrate growth forming a film at the interface of gas and water. The water-to-hydrate conversion of neither ZIF-8 nor ZIF-67 exhibited a significant dependency on the crystal-to-water mass ratio as compared to the results from our previous study where we used the metal organic framework HKUST-1 as a promoter at the same conditions, as we saw a significant positive correlation between crystal-to-water mass ratio and water-to-hydrate conversion.[26] A small decrease in conversion was observed at the higher ZIF to water mass ratios in this study, most likely due to the increased amount of water slightly decreasing the gas-to-water contact area.

The organic linker 2-methylimidazole linker, present in both ZIF-8 and ZIF-67, contributes to high hydrophobicity in both materials, as evident from water contact angle measurements and water adsorption isotherms reported in literature.[145,146,158–160] This high hydrophobicity promotes hydrate growth, as found by a study that compared the efficacy of a hydrophobic and a hydrophilic MOF in promoting methane hydrate growth.[87] These authors demonstrated that the hydrophobic MOF promoted more water-to-hydrate conversion, thus increasing the amount of methane stored in hydrate form.[87] Other studies in the literature determined that a hydrophobic surface does not negatively interfere with the ordering of water molecules necessary for hydrate nucleation,[128,161] further supporting the positive effect of hydrophobicity in hydrate growth.

Another influential property of ZIF-8 and ZIF-67 is their relatively high methane adsorption. The methane adsorption isotherms obtained for the synthesized ZIF-8 and ZIF-67 are shown in Figure 4.5.

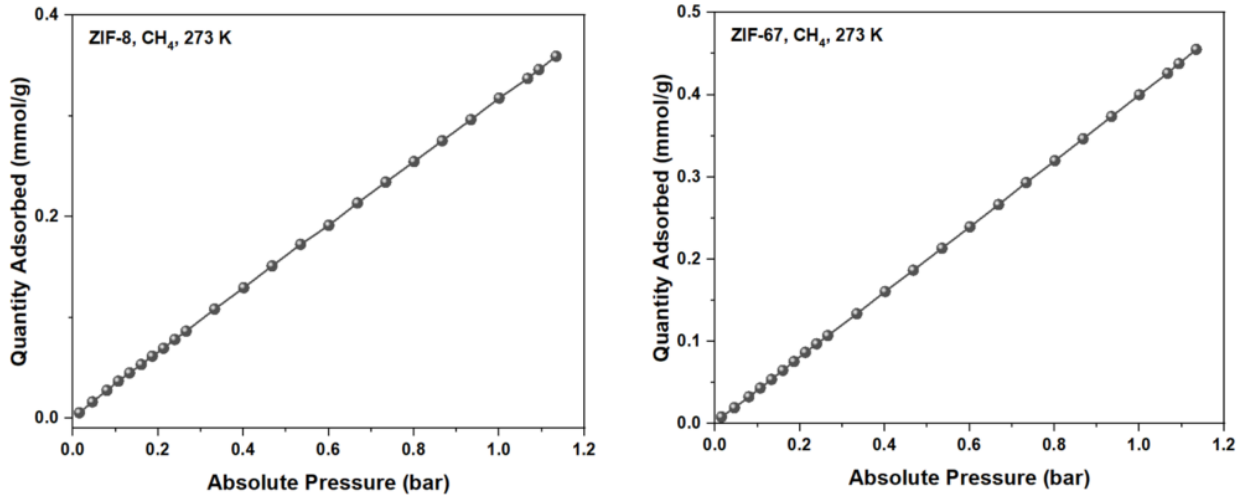

Figure 4.5 Methane adsorption isotherm for synthesized ZIF-8 (left) and synthesize ZIF-67 (right) conducted at 273K after degassed at 200°C for 8 hours.

The linear shape of the methane adsorption isotherms collected in this work are at low pressures (max of 1.1 bar) and match the shape of methane adsorption for both ZIF-8 and ZIF-67 at these similar low pressures.[87,148] ZIF-8 stores approximately 0.33 mmol CH_4/g at 1 bar and 273K, which is less than the value reported in the literature at similar conditions (0.53 mmol/g at 1 bar and 273K).[148] The difference in CH_4 uptake may be related to different textural, and morphological properties (surface area, crystal size among others). ZIF-67 stored more than ZIF-8, reaching a high of 0.41 mmol CH_4/g at 1 bar and 273K. This value, as well, was lower than reported in the literature (0.54 mmol/g at 1 bar and 273K).[148] Note, at higher pressures (~80 bar), studies observed significantly higher methane adsorption (~8 mmol/g) for ZIF-8, thus more methane may be adsorbed to the ZIFs at the conditions of the HP-DSC.[89] The methane adsorbed on the material's surface acted as a methane source for hydrate formation. When combined with the hydrophobicity of the materials, this methane source helps promote hydrate growth, as observed in a similar system with silica material.[162] Additionally, the methane adsorption isotherms collected in this work are at 1 bar, whereas in literature a study measured methane adsorption on ZIF-8 as high as 8 mmol/g at 80 bar, indicating that significantly more methane may be adsorbed to the ZIFs during the HP-DSC experiments.[89]

An isothermal HP-DSC elucidated that ZIF-8 and ZIF-67 dramatically reduced the hydrate nucleation induction time (i.e. the time between the system's stabilization at -15°C and the appearance of an exothermic peak, which is indicative of hydrate formation). A system with no porous material had a nucleation induction time of 3.8±1.3 hours. ZIF-8 and ZIF-67 reduced this time on average by 2.0 hours (51.6% decrease) and 3.5 hours (92.2% decrease), respectively. Therefore, these materials provide a considerable kinetic advantage as methane hydrate promoters. Figure 4.6 shows the isothermal HP-DSC profiles of ZIF-8 and ZIF-67 compared to a system without any material.

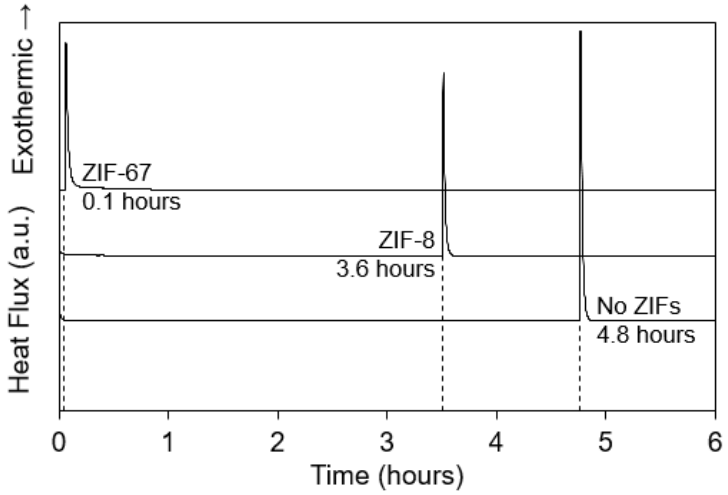

Figure 4.6 Profile of isothermal HP-DSC experiments conducted at -15°C for ZIF-67 (top), ZIF-8 (middle), and a system with any porous material (bottom).

In terms of shortening hydrate nucleation induction time, ZIF-67 exceeded the performance of ZIF-8. The 1.3-hour-faster induction time of ZIF-67 can be attributed to two measured properties that differ between the synthesized ZIFs: surface area and methane adsorption. The synthesized ZIF-67 has a surface area of 1585 m^2/g, whereas the surface area of the synthesized ZIF-8 is 1052 m^2/g. As mentioned above, the methane adsorption of ZIF-67 (0.41 mmol/g at 1 bar) is higher than ZIF-8 (0.33 mmol/g at 1 bar). For both materials, methane adsorbs preferentially to the organic linker, not the metal ions. The larger surface area is capable of containing more adsorbed methane, and thus surface area is the primary reason for differing induction times.[30] Therefore, the higher surface area and methane adsorption capacity of ZIF-67 results in ZIF-67 reducing the hydrate nucleation induction time more than ZIF-8.

4.3.2 Effect of ZIF-8 & ZIF-67 on Hydrate Dissociation Temperature

The average hydrate dissociation temperatures in systems with ZIF-8 (8.2°C±0.3) or ZIF-67 (8.8°C±0.1) is notably lower than that in a system without any porous material (11.5°C±0.1). (These data are also shown in Table 4.2.) The shift to a lower hydrate dissociation temperature is indicative of hydrate formation inside the material, rather than just on the external surface.[104,163] The depression in the dissociation temperature is caused by confined water molecules in the pores having lower water activity.[88,164]

The low water activity requires more thermodynamic driving force to form stable hydrates, and thus these hydrates dissociate at lower temperatures when compared to a bulk hydrate system.[164] Typically, the extent of depression of the hydrate dissociation temperature depends upon the size of the pores, with smaller pore sizes (not smaller than the unit cell size of a hydrate) resulting in a greater depression.[72,104] Thus, methane hydrate formation is taking place in a confined space provided by the ZIFs. The first possible confined space is the pores, as nitrogen isotherms of ZIF-8 and ZIF-67, shown in Figure 4.7, reveal that, for both materials, the larger pore cavity width is ~1.2 nm, which is about the size of the structure I hydrate unit cell (1.2 nm). Additionally, the organic linkers in the ZIFs' structure leads to flexibility, and thus could expanded to better accommodate a methane hydrate.

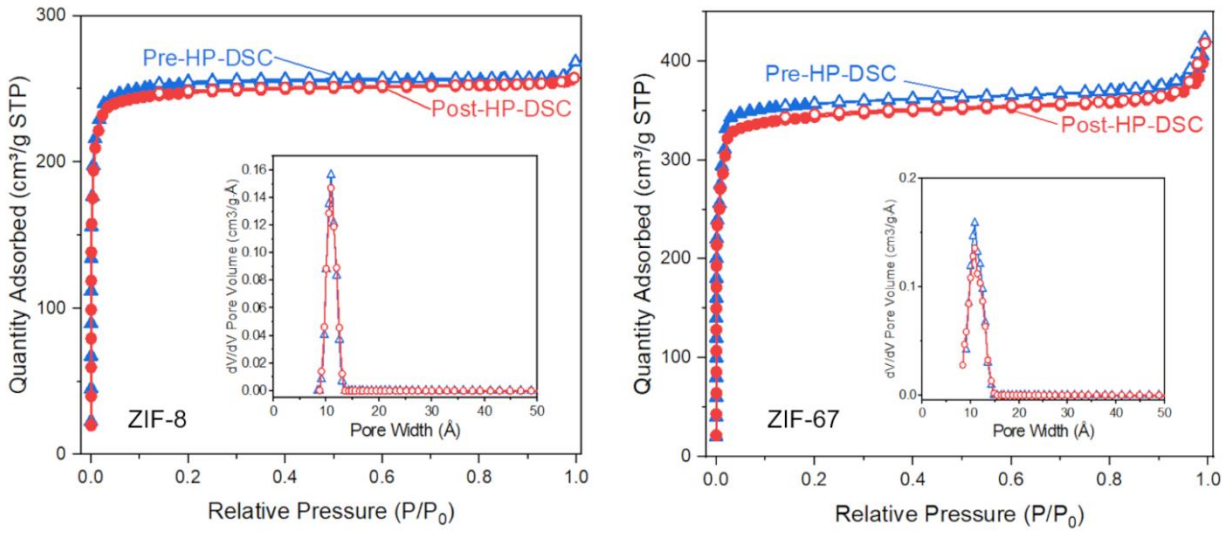

Figure 4.7 Nitrogen isotherms with insets showing pore distributions calculated from NLDFT for synthesized ZIF-8 (left) and ZIF-67 (right) before and after subjecting the crystals to hydrate formation (pre HP-DSC) and hydrate dissociation (post HP-DSC).

Although possible, the pores are an unlikely location for hydrate formation due to the similarities in pore size and the hydrophobic nature of the ZIFs. Even though the hydrophobic external surface of ZIF-8 and ZIF-67 promotes hydrate growth through its positive effect on water ordering, the hydrophobicity limits water uptake into the crystal structure. Water adsorption isotherms reported for ZIF-8 and ZIF-67 in literature show low water uptake, in the range of 0.2 mmol/g to 0.5 mmol/g depending upon the relative pressure.[159,160] The flexible structure of the ZIFs does exhibit better diffusion of molecules at high pressure, such as the conditions in the HP-DSC. An experimental and simulation study on ZIF-8 at high pressures found that at high pressures, the pore windows (3.4Å) expanded to allow transport of molecules through it that typically were too large to fit, such as methane (3.8Å), a phenomena termed 'gate opening'.[165] The enlargement accounts for the high methane adsorption capacity of ZIF-8 at high pressures ranging from 1.8 mmol/g at 1 MPa to 8.5 mmol/g at 10 MPa.[89,165,166] The gate opening of the ZIFs at high pressure thus would allow more diffusion of water throughout the structure, potentially giving rise to hydrate formation within the ZIFs pores. The hydrate formed may only be defective hydrate crystals, a result found in a study that used inelastic neutron scattering to observe hydrate formation in the micropores (<0.7 nm) of hydrophobic activated carbon.[82]

Most likely, though, the reduced dissociation temperature observed in this study with ZIF-8 and ZIF-67 results from formation in the interstitial spacing rather than the pores. This interstitial space is formed of the gaps that result from uneven packing of crystallites in a ZIF particle. A study on MIL-53 found that the hydrate dissociation temperature decreased in the presence of MIL-53, yet the micro pore of MIL-53 (0.6 nm) are too small for the structure I unit hydrate cell.[88] It has been suggested that the observed depression in the hydrate dissociation temperature was caused by hydrate formation taking place in the interstitial space.[88] Therefore, if the interstitial spacing is significant, then it may act more like an external surface, and would not significantly inhibit the water diffusion necessary to form hydrates within these spaces.

4.3.3 Characterization of ZIF-8 Pre & Post Hydrate Formation & Dissociation

With regard to water-to-hydrate conversion, ZIF-8 exhibited a unique trend over the first 3 cycles of hydrate formation and dissociation. Conversion increased from 51.3% in the first cycle to 78.6% in the second and 85.6% in the third. After the third cycle, the consecutive fourth and fifth cycles only showed deviations of ±2.7% from the third cycle. These stabilized results indicate that a change in the material occurred within the first three cycles. Figure 4.8(a) shows

the powder X-ray diffraction (XRD) patterns of ZIF-8 pre- and post-HP-DSC, showing a good match to the simulated sodalite crystallographic pattern, and the relative crystallinity of the peak at 7.3 2θ was maintained with only a 2% deviation over all the cycles.

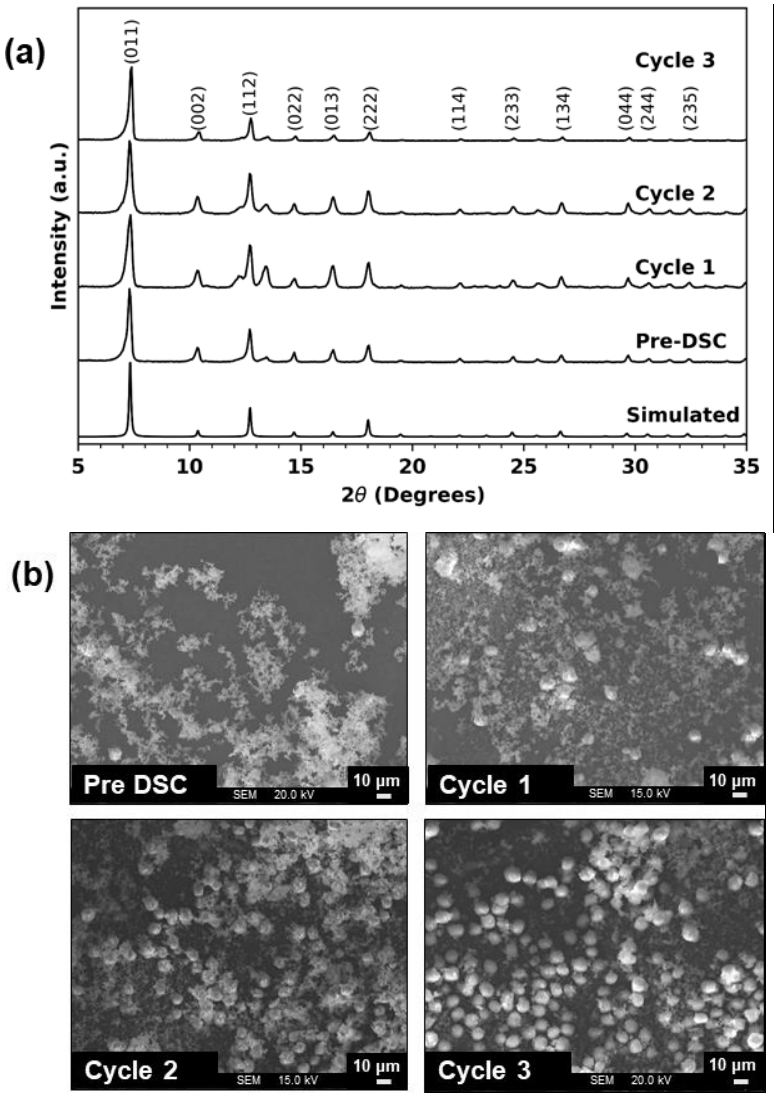

Figure 4.8 (a) X-ray diffraction patterns of: the ZIF-8 sample before hydrate formation and dissociation (Pre-DSC); the ZIF-8 sample after three consecutive cycles; and a simulated pattern for ZIF-8. (b) SEM images of the ZIF-8 sample before the HP-DSC and then after three consecutive cycles.

Notably, however, an unexpected peak arose after the first cycle at 13.4 2θ. This peak then decreased in intensity and nearly disappeared by the third cycle. The presence of this peak may be related to a change in surface morphology.

The SEM images in Figure 4.8(b) confirm that a morphological change took place after each of the first three cycles. The original ZIF-8 sample was a fine powder with an average crystal size of 1.05±0.09μm. After the first cycle, large crystal agglomerates started to appear. Magnified SEM images, shown in Figure 4.9, suggest that the agglomerates arise from the merging of the small crystal particles, as evident in the dashed red circles on the images.

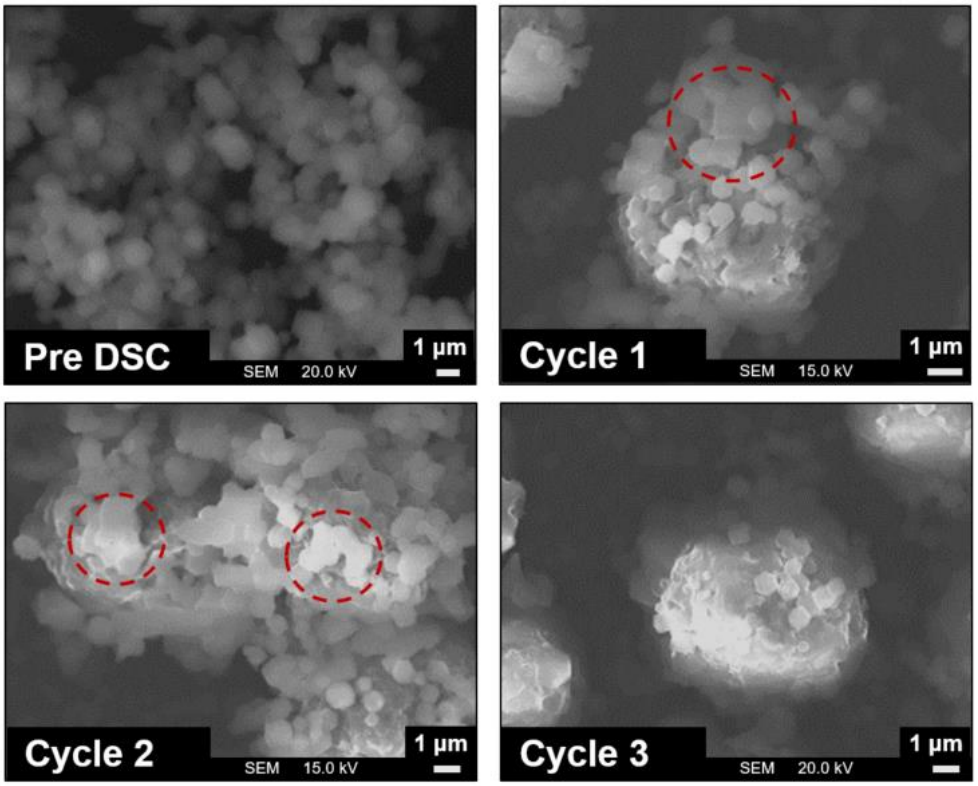

Figure 4.9 SEM images of the synthesized ZIF-8 crystals before and after hydrate formation and dissociation for 3 consecutive cycles. Dashed red circles surround evident areas of agglomeration during cycle 1 and cycle 2, whereas most crystals have already agglomerated by cycle 3.

Immediately after the first cycle, these agglomerates measured up to 8.89±1.10μm, while the other crystals maintained a size of 1.13±0.17μm. The ratio of agglomerates to original particles increased with each cycle until almost all the small crystals were agglomerated. This increase in agglomeration correlated to an increase in conversion, as depicted in Figure 4.10.

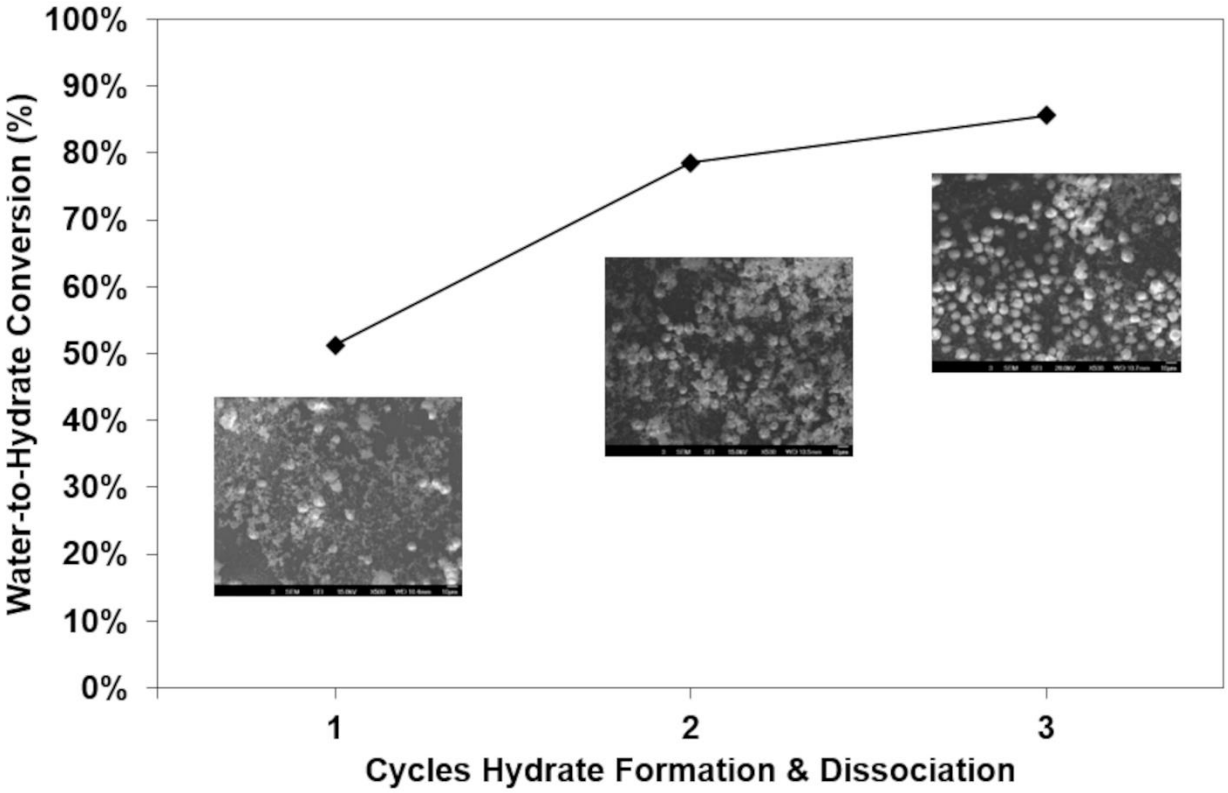

Figure 4.10 Change in water-to-hydrate conversion for 3 cycles of hydrate formation and dissociation for ZIF-8. Inset SEM images of the extent of agglomeration for each cycle.

Therefore, the process of hydrate formation and dissociation must cause the agglomeration; the agglomeration, in turn, promotes more hydrate growth.

Agglomeration of the ZIF-8 particles was observed in another study that examined the performance of ZIF-8 as a promoter.[90] The authors only conducted one cycle of hydrate formation and dissociation, but they found that as the water content in their test increased, the extent of agglomeration increased, too. Therefore, they concluded that water caused ZIF-8 to agglomerate due to the strong hydrogen bonds formed by water molecules making the ZIF-8 particles more attracted to one another.[90] According to the literature, ZIF-8 does not experience any deformation upon exposure to high pressure methane[87] – thus eliminating high pressure as a potential cause of agglomeration. Hence, the observed increase of agglomeration is most likely attributable to increased time of water exposure, with which it correlates.

Another study that used ZIF-8 as a methane hydrate promoter found that the behaviour of the porous material changed after a single cycle of formation and dissociation.[87] The authors concluded that, during the first cycle, hydrate formation takes place primarily in the pores of the

ZIF-8 crystal structure, whereas in the second cycle, hydrate formation occurs in the interstitial space between crystals or on the external surface.[87] The ZIF-8 agglomerates in this study may be forming optimal interstitial spacing for hydrate formation as the single crystals merge. Interestingly, the agglomeration of ZIF-8 particles did not significantly affect surface area (1052 m^2/g to 1031 m^2/g) or pore volume (0.4 cm^3/g to 0.39 cm^3/g). Other than the observed morphology change, the integrity of the ZIF-8 structure is maintained.

4.3.4 Characterization of ZIF-67 Pre & Post Hydrate Formation & Dissociation

For ZIF-67, water-to-hydrate conversion remained consistent throughout each hydrate formation and dissociation cycle. The XRD pattern of the Pre-DSC sample of ZIF-67 matched the simulated sodalite pattern well, as shown in Figure 4.11(a).

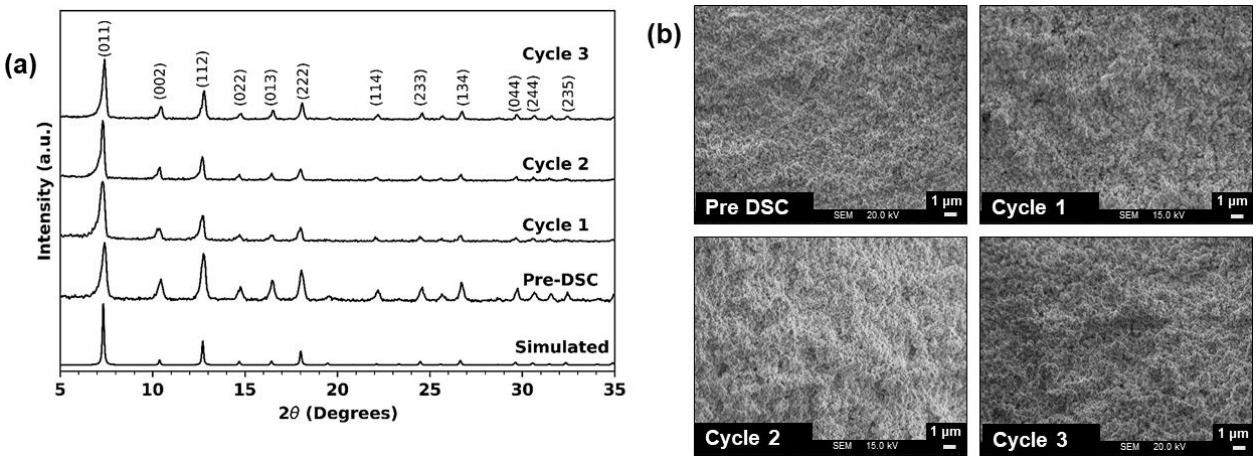

Figure 4.11 (a) X-ray diffraction patterns of: the ZIF-67 sample before hydrate formation and dissociation (Pre-DSC); the ZIF-67 sample after three consecutive cycles; and a simulated pattern for ZIF-8. (b) SEM images of the ZIF-67 sample before the HP-DSC and then after three consecutive cycles.

No appreciable changes occurred in the XRD pattern between the pre- and post-DSC samples aside from an increase in relative crystallinity of the peak at 7.3 2θ after the first cycle of hydrate formation and dissociation. The ~30% observed increase after the first cycle can be attributed to the HP-DSC conditions interacting with any unused precursors to complete the crystal synthesis, as phenomena observed in a study on the effect of ZIF-67 synthesis time on relative crystallinity.[167] To ensure no further changes occurred, a sample of ZIF-67 after 8 cycles was compared to the sample after 1 cycle, and the crystallinity only differed by ±1%. Figure

4.11(b) shows SEM images of the ZIF-67 sample before and after hydrate formation and dissociation. The ZIF-67 crystals as synthesized were packed together, but did not agglomerate after each cycle. Magnified SEM images of the surface morphology of the ZIF-67, shown in Figure 4.12, further indicates that no morphology changes occurred.

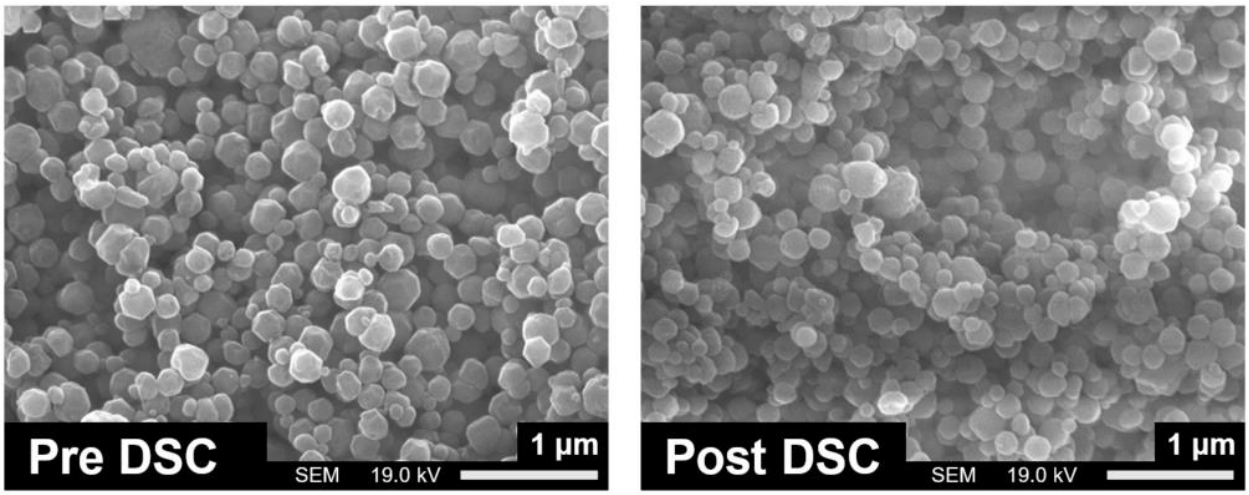

Figure 4.12 SEM images of the synthesized ZIF-67 crystals before (pre DSC) and after (post DSC) 3 cycles of hydrate formation and dissociation.

The consistency of hydrate conversion and the absence of significant changes in the XRD patterns nor SEM images of the pre- and post-DSC ZIF-67 samples indicates that ZIF-67 preserved its structural integrity and resulted in outstanding recyclability. A brief investigation was conducted on the particle size effect for ZIF-67 on hydrate growth promotion. The small particles (0.21±0.05µm), shown in Figure 4.11, led to a conversion of 87.7% at an R_w of 0.50, as reported in Table 4.2. Interestingly, when larger size ZIF-67 particles (2.95±0.45µm), shown in Figure 4.13, were subjected to the HP-DSC, the conversion was 87.6% at an R_w of 0.57.

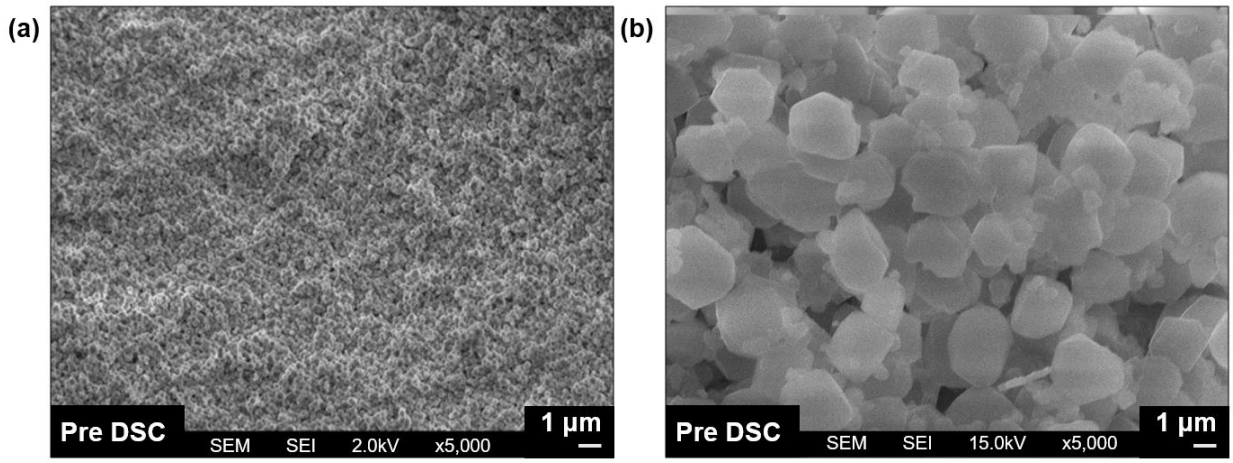

Figure 4.13 (a) synthesized ZIF-67 particles pre HP-DSC with particle diameter of 0.21±0.05µm and (b) with particle diameter of 2.95±0.45µm.

This indicates that for ZIF-67 the particle size does not play a significant role the hydrate growth promotion performance.

While the water-to-hydrate conversion for both ZIFs was similar, there was a difference in the methane hydrate nucleation induction time between the two ZIFs. The difference in reduction observed with ZIF-67 relative to ZIF-8 stems from higher methane adsorption of ZIF-67 as compared to ZIF-8 (0.41 mmol/g versus 0.33 mmol/g, respectively). Since both ZIFs are isostructural and have the same linker, this difference in adsorption uptake is related to the presence of different metal cores, and different textural properties of both ZIFs.

4.4 Conclusions

The methane hydrate growth promotion performance of the two studied zeolitic imidazolate frameworks, ZIF-8 and ZIF-67, showed highly promising results, with water-to-hydrate conversions as high as 85.6% and 87.7%, respectively. The primary factor was the large surface area of ZIF-8 (1052 m^2/g) and ZIF-67 (1585 m^2/g) reducing mass transport limitations by increasing the gas-to-water contact area. ZIF-8 and ZIF-67 reduced the induction times on average by 51.6% and 92.2%, respectively. The difference in reduction observed with ZIF-67 relative to ZIF-8 stems from higher methane adsorption of ZIF-67 as compared to ZIF-8 (0.41 mmol/g versus 0.33 mmol/g at 1bar, respectively). ZIF-8 experienced a morphological change over the course of three consecutive cycles of hydrate formation and dissociation while maintain crystallinity. The fourth and fifth cycle resulted in consistent conversion to the third cycle, and the morphological changes to ZIF-8 ceased after the third cycle, indicating that these two were

correlated. The structural integrity of both ZIFs was preserved. The results from this study conclude that ZIF-8 and ZIF-67 are highly suitable methane hydrate growth promoters. This work demonstrates that ZIF-8 and ZIF-67 are capable of overcoming the mass transfer limitations and slow kinetics typical of methane hydrate formation, exhibiting exceptional potential as a way to transition methane hydrates into an efficient and economical method for methane storage and transportation.

CHAPTER 5

POROUS ORGANIC CAGE CC3: AN EFFECTIVE PROMOTER FOR METHANE HYDRATE FORMATION FOR NATURAL GAS STORAGE

Modified from: S. Denning, A.AA. Majid, J.M. Lucero, J.M. Crawford, M.A. Carreon, C.A. Koh*, "Porous Organic Cage CC3: An Effective Promoter for Methane Hydrate Formation for Natural Gas Storage" ***J. Phys. Chem. C 2021***, 2021, 37, 20512-20521

The work detailed in this chapter covers the study we conducted on subjecting the porous organic cage CC3 to methane hydrate formation to determine its effects on the process. The contents of this chapter are published in J. Phys. Chem. C 2021, 37, 20512-20521.

5.1 Porous Organic Cage CC3

A better understanding of porous material and hydrate formation and dissociation structure-function relationships is key to determining the optimal promoter. Despite the wide range of hydrate formation growth promoters studied, one understudied group is organic porous materials.[79] A novel class of organic porous materials that is highly appealing as a hydrate growth promoter is porous organic cages (POCs).[168] To the best of our knowledge, no studies have been conducted using any POC as hydrate growth promoters. POCs exhibit a unique crystal structure, as they are covalently bonded discrete organic cages that can self-assemble into a microporous material.[168] This solid-state molecular packing is unlike other porous materials such as zeolites or activated carbon.[35,169] The resulting assembly has intrinsic pores (inside the cage) and extrinsic pores (between he assembled cages), and the structure contains the following covalent bonds: C-N, N-H, H-C, and C-C.[168]

The work reported here targets, specifically, the porous organic cage denoted as αCC3 (also referred to as CC3) as a methane hydrate growth promoter. This POC has a 3D microporous crystalline structure comprised of 1,3,5-triformylbenzene coordinated with trans-1,2-diaminocyclohexane that forms cages with unimodal limiting pore size of ~3.6Å and internal cavity diameter of ~5Å.[168,170] These cages are connected via the cyclohexyl groups to form diamondoid pores, as illustrated in Figure 5.1.[168] CC3 is being explored for various applications, such a gas adsorbent (SF_6, Xe;[171] acetylene, ethane, CH_4, ethylene;[36] CO_2[172]), proton

conductor,[173] gas chromatography separations with chiral alcohols,[174] catalytic support for noble metals,[175] and for gas separation via membranes.[32,39,176]

CC3 possesses several unique and advantageous properties that make this microporous crystalline material highly appealing as a methane hydrate promoter. These properties include large surface area,[168] high methane uptake,[79] flexible framework,[172] stability under high pressure,[36,172] and chemical stability.[32] In principle, these properties would not only enable CC3 to improve water-to-hydrate conversion and reduce hydrate nucleation induction time, but also could result in high recyclability of CC3.

In this work, we studied the impact of CC3 on methane hydrate formation and dissociation by employing a high pressure differential scanning calorimeter (HP-DSC). The addition of CC3 improved the water-to-hydrate conversion significantly and reduced the hydrate nucleation induction time primarily due to the large surface area and high methane adsorption.

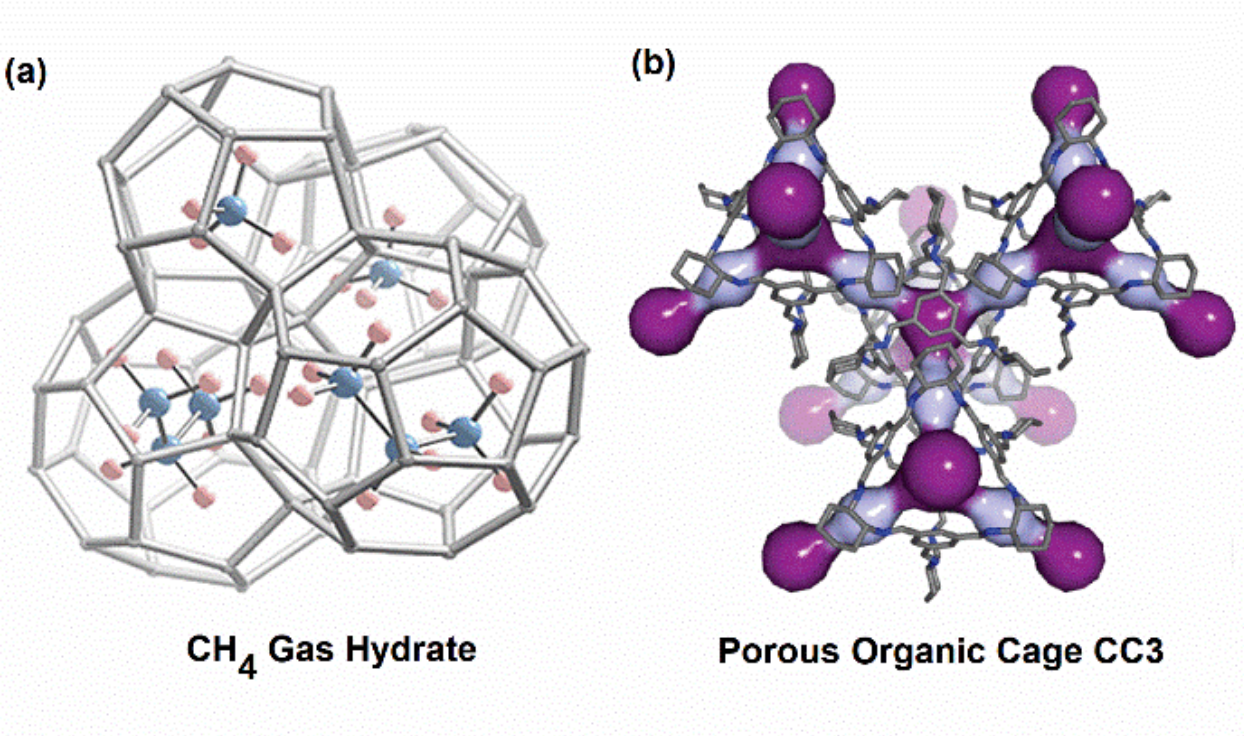

Figure 5.1 (a) Methane structure I hydrate, consisting of water molecules forming hydrogen bonds to encage methane. Unit cell length is ~12 Å.[117] (b) Porous organic cage CC3, consisting of 1,3,5-triformylbenzene coordinated with trans-1,2-diaminocyclohexane, displaying limiting pore aperture of 3.6Å in light purple and the internal cage cavity of ~5 Å in dark purple.[168,170]

5.2 Experimental Methods

The following subsections cover the synthesis and characterization of CC3 along with the high pressure differential scanning calorimeter (HP-DSC) procedure and calculations.

5.2.1 Synthesis of CC3

Microwave assisted thermal treatment was used to synthesize uniform, and narrow size distribution CC3 crystals. Microwave assisted approach is an effective synthetic strategy to synthesize chemically diverse porous crystals with narrow size distribution,[154,177] including CC3 crystals.[155]

The precursors used in the CC3 synthesis were 1,3,5- triformylbenzene (ACROS Organics, 98%), (±)-trans-1,2-diaminocylcohexane (Sigma Aldrich, 99%), dichloromethane (ACS certified, stabilized, Fisher Scientific) and trifluoroacetic acid (Alfa Aesar, 99%). In a typical synthesis, 25 mL of dichloromethane was added slowly to 200 mg of 1,3,5-triformylbenzene in a Teflon liner. Next, 100 µL of trifluoroacetic acid was added. In a separate beaker, 25 mL of dichloromethane was added to 102 mg of (±)-trans-1,2-diaminocylcohexane. This solution was slowly added to the solution in the Teflon liner before putting the liner into a XP1500 vessel. The vessel was placed in a CEM Mars 5 microwave and a thermocouple into the vessel for to control the temperature. The microwave was operated at 100% of 400W for 2 hours at 100°C. Once complete, the vessel was naturally cooled to room temperature. A mixture with the ratio of 60/40 ethanol/dichloromethane was added, and then the solution was centrifuged to separate the crystals from solution. Finally, the crystals were washed twice using ethanol before drying in an oven at 80°C.

5.2.2 Characterization Methods

The structure of CC3 before and after being subjected to hydrate formation and dissociation was characterized using powder X-ray diffraction (XRD), field emission scanning electron microscope (FESEM), argon adsorption isotherm, and methane adsorption isotherm. The XRD used was a Siemens Kristalloflex 810 diffractometer that operated at a wavelength of 1.54059Å, a voltage of 30 kV, and a current of 25 mA. The FESEM used was a JEOL JSM-7000F. The argon adsorption isotherms at 87K and methane adsorption isotherm at 0°C were collected using an ASAP 2020 porosimeter (Micromeritics, Norcross, GA, USA), with the samples undergoing a degas step at 200°C for 8 hours under vacuum. Surface areas were calculated using the cross sectional diameter of Ar (0.142 nm) and the Brunauer-Emmett-Teller

(BET) method following the criteria described elsewhere.[178] The water adsorption isotherm was collected at 22°C using an ASAP 2020 equipped with a vapor adsorption accessory. Prior to analysis, doubly distilled deionized water was loaded in the vapor flask, purged with nitrogen, and allowed to equilibrate at 22°C for 8 hours.

5.2.3 Scherrer Crystallite Size Calculations

To determine the size of the CC3 crystallites, the measured width of the peaks in the powder X-ray diffraction pattern was used in Scherrer's equation:

$$L = \frac{K*\lambda}{B*\cos(\theta)} \tag{5.1}$$

Where 'L' represents the size of the crystallites, 'K' is Scherrer's shape factor constant, 'λ' is the wavelength, 'B' is the full width of the peak at half its maximum intensity (FWHM), and 'θ' is the diffraction angle.[179]

5.2.4 High Pressure Differential Scanning Calorimeter Procedure

Hydrate formation and dissociation were observed using a high pressure differential scanning calorimeter (HP-DSC) VIIa Seteram Inc. that has the resolution of 0.04 μW. The HP-DSC can operate between -45°C to 120°C and 0.1MPa to 15.4MPa with the precision of ±0.2°C and ±25kPa, respectively. The HP-DSC schematic is illustrated in Figure 5.2.

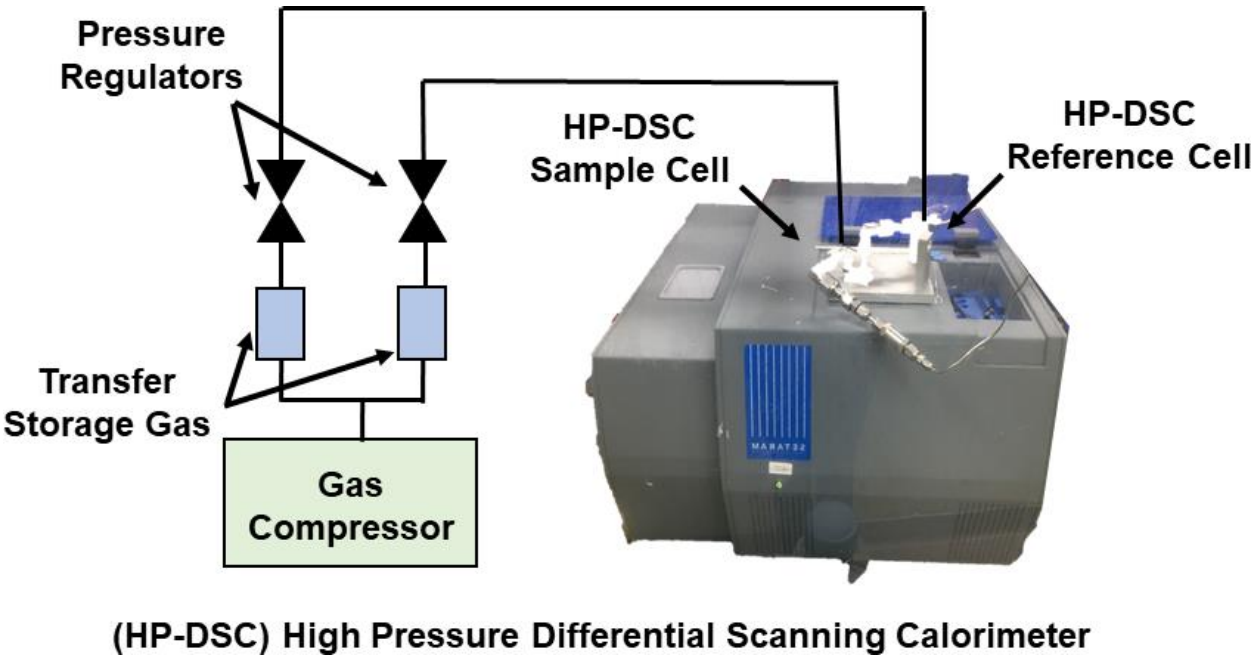

Figure 5.2 High pressure differential scanning calorimeter (HP-DSC) schematic.

The procedures implemented in this study are parallel to our previous work.52 To prepare the samples, first deionized water was added to the HP-DSC cell. Next, the synthesized CC3 was added to the cell to achieve a specific water-to-CC3 mass ratio (Rw). Once the cell was placed in the HP-DSC, the system was pressurized with methane gas (Matherson, 99%).

The first method employed was a scan. The system was raised to a temperature of 30℃ at a heating rate of 0.5℃/min, and then held at 30℃ for 3 hours. Next, the system was cooled to -30℃ at a rate of 0.3℃/min and then heated to 30℃ at the same rate. This scan was repeated 3 times for each sample for the purpose of reproducibility of the results and to determine if the structure integrity of CC3 was maintained.

The second method was an isothermal test. Similar to the scanning method, the system was heated to 30℃ at a rate of 0.5℃/min and then held at that temperature for 3 hours. Then the system was cooled at a rate of 0.8℃/min to -10℃. The temperature was held at -10℃ for 12 hours before heating the system at a rate of 0.3℃/min to 30℃. This process was repeated 3 times.

The warming and cooling HP-DSC heat flux profiles result in exothermic peaks (formation) and endothermic peaks (dissociation). The dissociation temperature denotes the temperature at the onset of the dissociation peak. The area under the peak relates to how much ice or hydrate formed and dissociated in the HP-DSC system.

5.2.5 Water-to-Hydrate Conversion Calculations

The heat flux measurements of the endothermic hydrate dissociation peak obtained from the HP-DSC, denoted as H_{diss}, was used in the following equation to calculation how much water was converted into hydrate during the experiment.[121]

$$\text{Hydrate Conversion (\%)} = 100 * \frac{H_{diss} * MW_{H2O} * n_{HYD}}{H_{HYD}} \tag{5.2}$$

The other variables in the equation are as follows: molecular weight of water (MW_{H2O}= 18 g/mol.); hydration number (n_{HYD}= 5.9)[121], and the heat of dissociation of the methane structure I hydrate (H_{HYD}=54.4 kJ/mol.).[122]

5.3 Results & Discussion

The next subsection cover the results from this work and provide a detailed analysis and discussion.

5.3.1 Impact of CC3 on Water-to-Hydrate Conversion

The addition of CC3 to the water and methane system in the high pressure differential scanning calorimeter (HP-DSC) resulted in a significant increase in the water-to-hydrate conversion, as shown in Table 5.1.

Table 5.1 Results of scanning HP-DSC experiments for a system with and without CC3, displaying water-to-hydrate conversion, hydrate dissociation temperature, and the amount of methane stored relative to the amount of water in the system.

Rw: Ratio H_2O to CC3 (g/g)	Water to Hydrate Conversion (%)	Dissociation Temperature (°C)	CH_4 Stored to H_2O in system (mmol/g)
No CC3	4.5%	11.5	0.42
0.47	82.2%	10.2	7.6
0.65	85.3%	9.9	7.9
0.86	86.9%	9.9	8.0
0.93	80.1%	10.3	8.1
1.22	87.5%	10.2	8.1
1.81	68.0%	10.7	6.3
3.98	10.7%	11.2	1.0
6.02	10.2%	11.1	1.0
6.20	9.8%	11.3	0.9

Values correspond to the third cycle of hydrate formation and dissociation.

The warming profiles gathered from the HP-DSC for selected experiments and full cooling and warming profiles are shown in Figure 5.4.

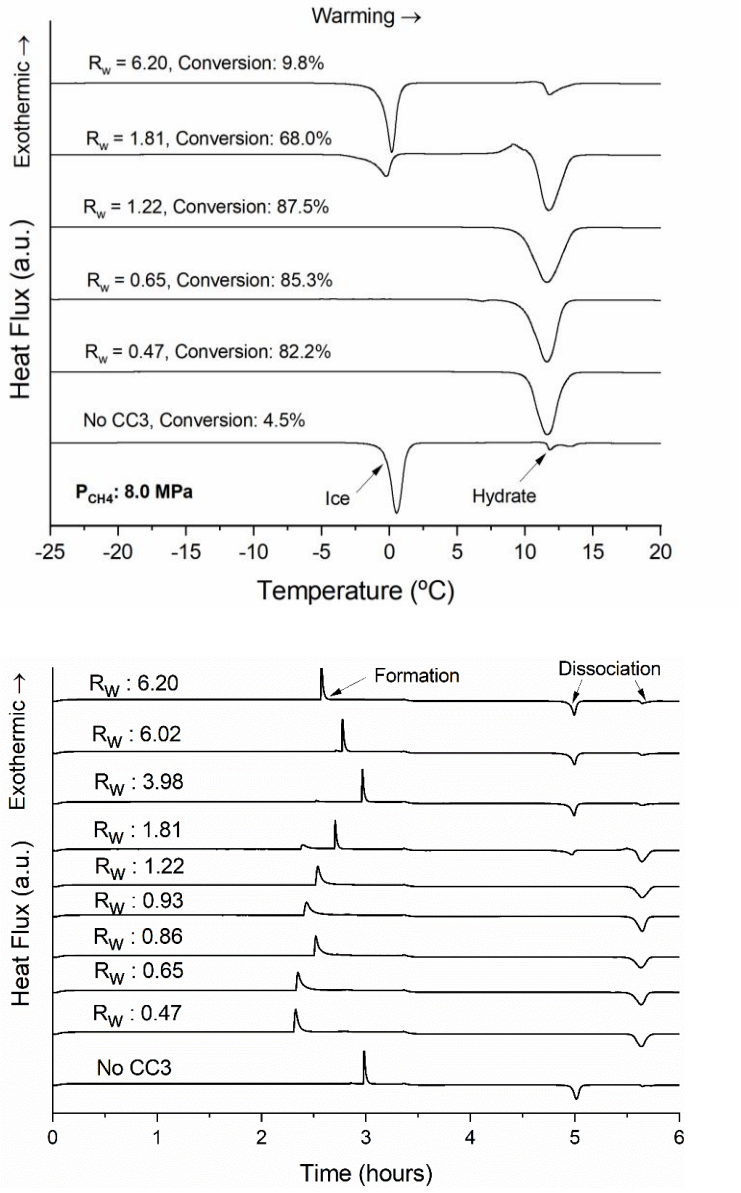

Figure 5.3 (Top) HP-DSC warming profiles for selected water to CC3 mass ratio and a system without CC3. (Bottom) Full HP-DSC cooling and warming profiles for the third cycle of all of the water to CC3 mass ratio experiments and the one absent of CC3.

Without CC3, only 4.5% of the water converted to hydrates, whereas adding CC3 increased the water-to-hydrate conversion to as high as 87.5%. This improvement in conversion correlated directly with a rise in the amount of methane stored relative to the amount of water in the system, going from 0.42 mmol/g without CC3 to as high as 8.1 mmol/g with CC3.

The water to CC3 mass ratio (R_w) was varied to learn if the conversion or dissociation temperature were directly influenced by the concentration of CC3 in the system. Other studies using hollow silica,[180] HKUST-1,[26] activated carbon,[82] and nano silica suspension[181] as hydrate

growth promoters found that the concentration of promoter played a major role in the overall conversion results. Our previous study on HKUST-1 (copper based metal organic framework) resulted in a direct correlation between conversion and R_w; 20.5% conversion at R_w of 0.39 increased to 87.2% conversion at R_w of 1.08.[26] For CC3, from the R_w of 0.47 to 1.22 the average water-to-hydrate conversion was 84.2±2.9% without any ice formation on the third cycle of hydrate formation. In contrast, in the first and second cycle, ice formation was observed. When the R_w reached 1.81, only 68.0% of the water converted to hydrates and ice formed on the third cycle. Therefore, the optimal R_w was 1.22. The water-to-hydrate conversion continued to decline as the R_w increased, and by R_w of 6.20 the conversion dropped to only 9.8%. Although this conversion is low compared to the other ratios, it is more than double the amount in a system without any CC3. The doubled conversion indicates that the large surface area of the synthesized CC3 (415.6 m^2/g) played a key role in promoting growth, as the crystals still increase the gas-to-water contact area as compared to bulk water.

Another property of CC3 that influences the water-to-hydrate conversion is the high methane adsorption capacity of CC3. Methane adsorption isotherms conducted at a low pressure of 1.2 bar and at 273K, shown in Figure 5.4, revealed that the synthesized CC3 used in this study adsorbed 1.60 mmol/g.

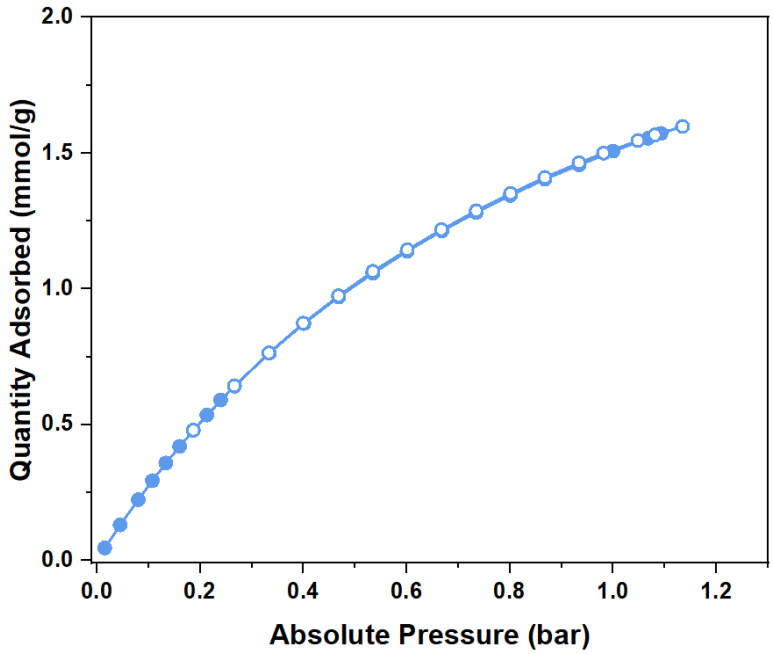

Figure 5.4 Methane adsorption isotherm conducted at 273K for the synthesized CC3.

Studies on methane hydrate formation in the presence of porous materials (excluding POCs) with high methane adsorption have found that the adsorbed methane can form gas bubbles or a gas layer on the surface of the material.[149,182] In these studies, methane bubbles or layers acted as nucleation sites and prevented the surface of the material from negatively interfering with the water ordering.[66,128,182] It is believed that the methane adsorbed on the structure of CC3 may result in a similar effect. Competitive water/methane adsorption occurs on the synthesized CC3, as the amount of water adsorbed is 3.67 mmol/g versus 1.60 mmol/g of methane. (See Figure 5.5 for the water isotherm).

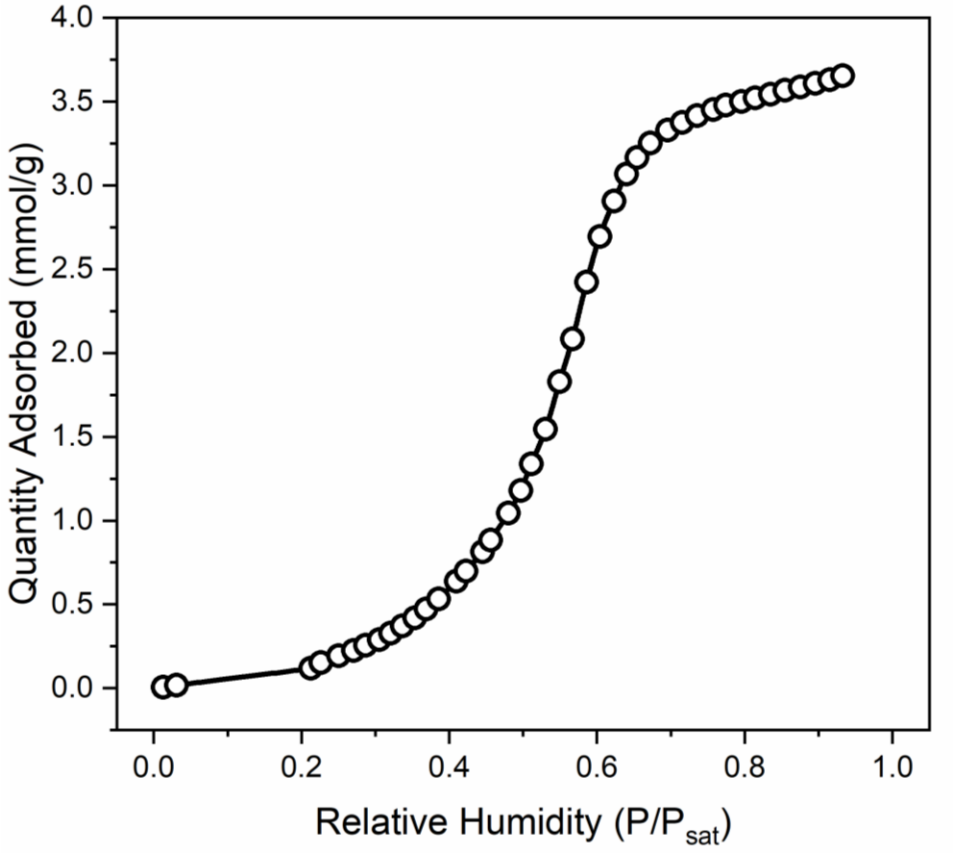

Figure 5.5 Water adsorption isotherm conducted at 295K for the synthesized CC3.

Note, the water adsorbed on this synthesized CC3 is one third of that found in a study in literature on CC3, which corresponds to the synthesized CC3 in this work having one third of the surface area of the CC3 in that study.[183] A study on the effects of hydrophobicity of porous materials on methane hydrate growth indicated that although a flat hydrophobic surface promotes

hydrate growth more than a hydrophilic one, the optimal internal surface of a pore large enough to contain hydrates is one with moderate wettability.[149] Therefore, the wettability of the synthesized CC3 combined with the competitive water/methane adsorption may provide a relatively good balance between promoting hydrate formation in both confined spaces and on the external surface of the crystal. This adsorbed methane may also account for the conversion at high water to CC3 mass ratios being twice that of a system without CC3, as the adsorbed methane creates a gas-to-water interface at the surface of CC3.

5.3.2 Impact of CC3 on Hydrate Dissociation Temperature

The addition of CC3 resulted in a decrease of hydrate dissociation temperature on average by 1.4±0.1℃ for the water to CC3 mass ratios of 0.47-1.22. A shift of the hydrate dissociation temperature to lower values is indicative of a reduction in the stability of the hydrate structure.[104,184] A change in hydrate stability (i.e. thermodynamic phase envelope) has been directly correlated to hydrates that formed in confined spaces, such as interstitial spacing caused by uneven crystallite packing discussed later, as the constricted space leads to lower water activity, and thus less stable hydrates.[58,85,86] A study on the metal organic framework MIL-53 as a hydrate growth promoter found that the hydrates confined in the pores of the material exhibited inhibited thermodynamic behavior (i.e. hydrate destabilization), resulting in hydrates dissociating at lower temperatures, attributing the decrease to reduced water activity.[49] Another study using porous silica glass observed that the hydrate dissociation temperature decreased with decreasing pore diameter, which shows that the extent of thermodynamic effects depends upon the type of material used.[39] A study on methane hydrate growth in silica gels reported a shift in hydrate dissociation temperature as large 6ºC, and found that the confinement effect on dissociation temperature tapered off for materials with pore sizes larger than 100nm.[48] For certain materials, there is an optimum pore size that results in the highest methane storage capacity, such as with model-carbon at a pore size of 25nm, despite the fact that it exhibited a depressed dissociation temperature due to constricted water activity in the pores.[87] Additionally, the chemical composition of the material can alter the stabilization of the hydrates inside of the pores, such as how a very hydrophilic pore inhibits formation.[80] All of these factors must be taken into consideration when evaluating confined hydrate growth.

Cryogenic argon isotherms (87K), shown in Figure 5.6, were used in place of typical nitrogen isotherms (77K) to measure the pore size distribution of CC3, as the kinetic diameter of argon (3.4Å) is small enough to probe the limiting aperture (3.6Å) of CC3.

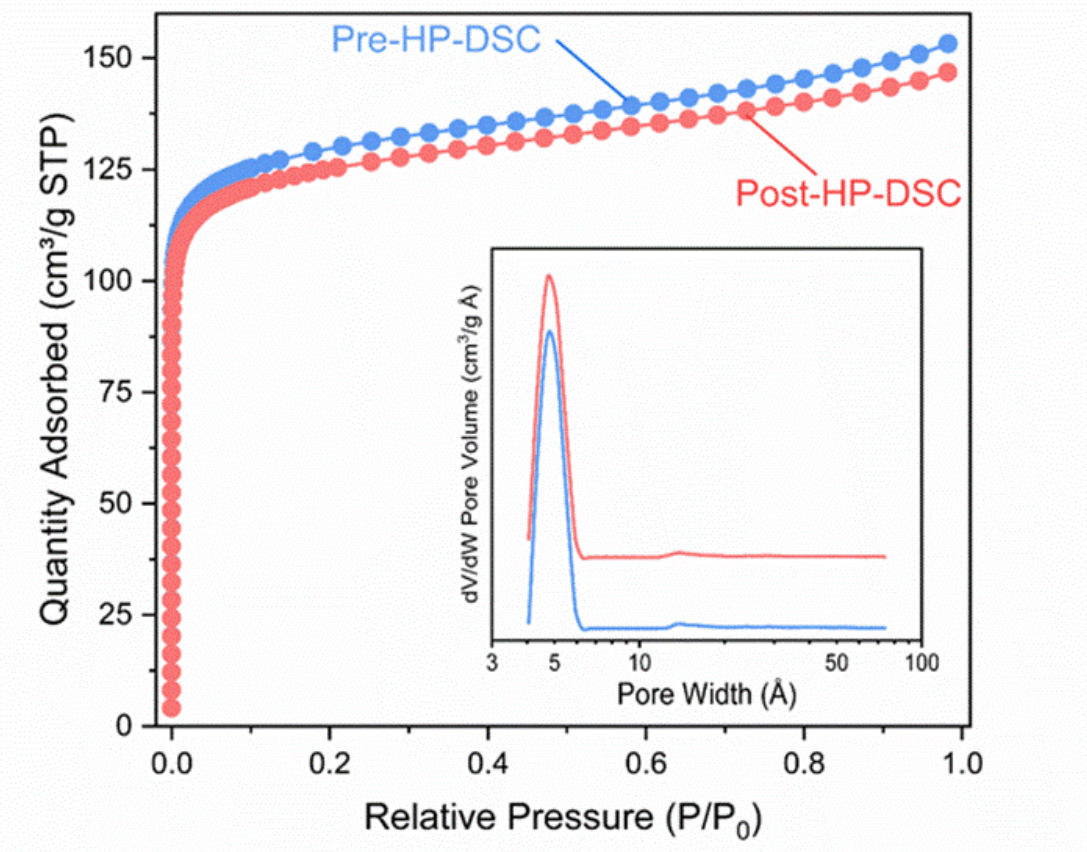

Figure 5.6 Argon isotherms conducted at 87K with insets displaying the pore size distributions calculated from NLDFT for CC3 samples before and after exposure to 3 cycles of hydrate formation and dissociation.

Our results indicate that the synthesized CC3 had a primary cavity size (intrinsic pore diameter) of 5Å, in agreement with the calculated cavity size reported in literature.[185] Hydrates cannot form inside of the CC3 cavity, as the typical methane hydrate structure I has a unit cell size of 12Å.[11,170] The more likely location of confined hydrate formation is in the void spaces caused by uneven packing of CC3 cages or by some incomplete cages, as illustrated in Figure 5.7a.[186]

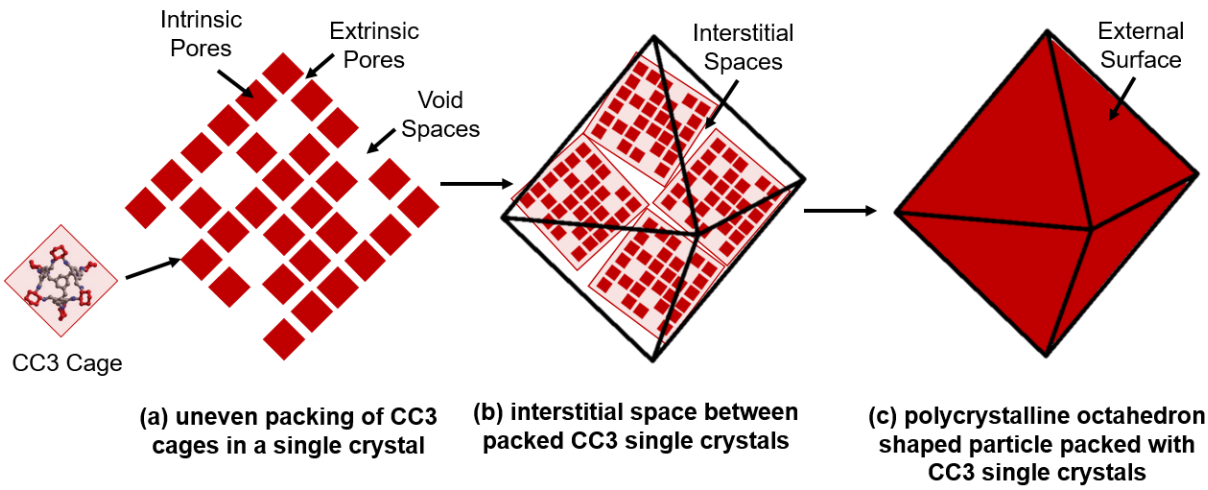

Figure 5.7 Illustration of the stages of CC3 particle packing: (a) uneven packing of CC3 cages in a single crystal creating void spaces ~1.2nm-1.5nm, (b) assembled CC3 single crystals with diameter ~25nm-50nm forming interstitial spacing, and (c) octahedron polycrystalline particle at ~2μm in diameter provides external surface for gas hydrate growth.

These void spaces would account for the secondary pore size at approximately 15Å observed in the argon isotherms at 87K, which represents approximately 5% of the total pore volume. Seminal work by Cooper et al. also observed the presence of larger pore sizes between the range of 12Å to 15Å, which can accommodate the hydrate structure I unit cell.[168]

The other type of confined space that could contain a methane hydrate is the interstitial spacing between the assembled CC3 crystallites, exemplified in Figure 5.7b. These crystallites pack together to form polycrystalline particles in an octahedron shape, illustrated in Figure 5.7c, which results in the overall external surface of the crystal where more hydrate formation can take place.

At the higher water to CC3 mass ratio of 3.98, the drop in conversion to 10.7% still exhibited a depressed dissociation temperature (11.1°C) relative to a system without CC3 (11.5°C). The decrease suggests that in the void and interstitial spaces, adsorbed methane promotes hydrate growth in these confined spaces despite the excess amount of water in the system.

5.3.3 CC3 Influences Hydrate Nucleation Induction Time

Addition of CC3 to the HP-DSC greatly influenced the kinetics of hydrate formation in two ways: 1) reduced the hydrate nucleation induction time and 2) promoted consistent hydrate formation. The isothermal HP-DSC experiments conducted at -10°C, as shown in Figure S5,

resulted in the hydrate nucleation induction time in a system absent of CC3 only forming hydrates 2 out of the 6 experiments, with the times 2.0 hours and 9.7 hours, with 4 out of 6 cycles not forming hydrates at all. The varying induction times are a result of the stochastic nature of hydrate formation, another barrier to commercializing hydrates for natural gas storage and transportation.[82] The isothermal experiments with CC3 showed improved results, as it produced hydrates for all four cycles conducted, as shown in Figure 5.8, with a consistent induction time of 0.8±0.1 hours.

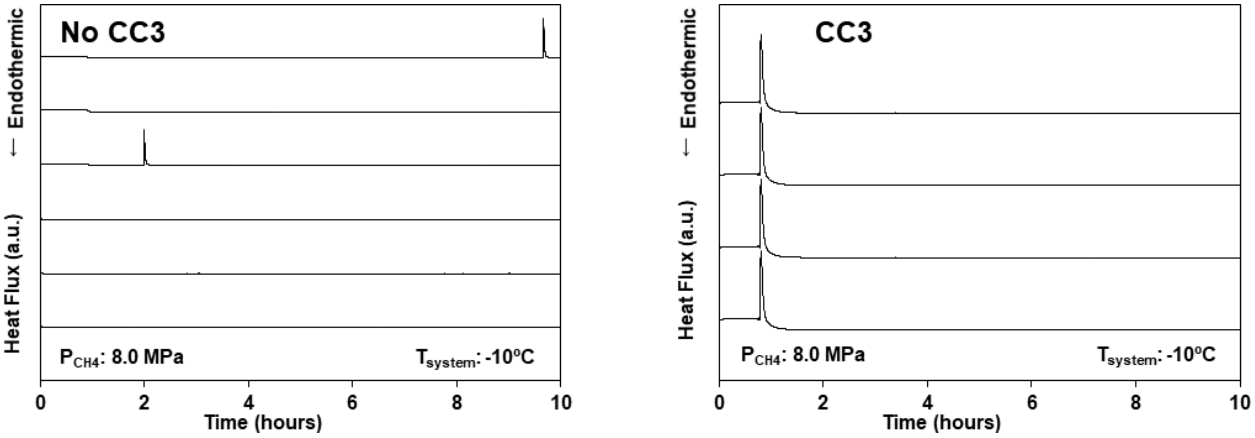

Figure 5.8 HP-DSC isothermal experiments held at -10ºC (left) system without CC3 and (right) system with CC3.

The properties of CC3 that influenced the improved kinetics of hydrate formation are its high methane adsorption capacity and reversible water uptake of CC3.[36,183] As mentioned previously, adsorbed methane acts as a source for hydrate growth, thus promoting growth in the void and interstitial spaces. As for water adsorption, a study on a microporous RHO zeolite as a hydrate promoter found that the hydrated micropores acted as hydrate nucleation sites.[96] The water uptake in CC3 results in hydrated micropores, as one CC3 cage can adsorb up to 12 water molecules, and reversible binding allows the water to disengage from the adsorption sites to participate in hydrate formation.[183] Therefore, the synergistic properties of water and methane adsorption lead to the exceptional performance of CC3 as a kinetic hydrate promoter.

5.3.4 Recyclability of CC3 after Hydrate Formation & Dissociation

Multiple cycles of hydrate formation and dissociation were conducted with CC3 in the HP-DSC to determine if the performance of CC3 was repeatable. The results showed interesting behavior. The water-to-hydrate conversion after the first cycle was on average 30% lower than

that of the second cycle for R_w of 0.47-1.22. For the same range of R_w, ice formation took place during the first cycle, yet no ice formed during the second nor during the third cycle, as exemplified for R_w of 1.22 shown in Figure 5.9.

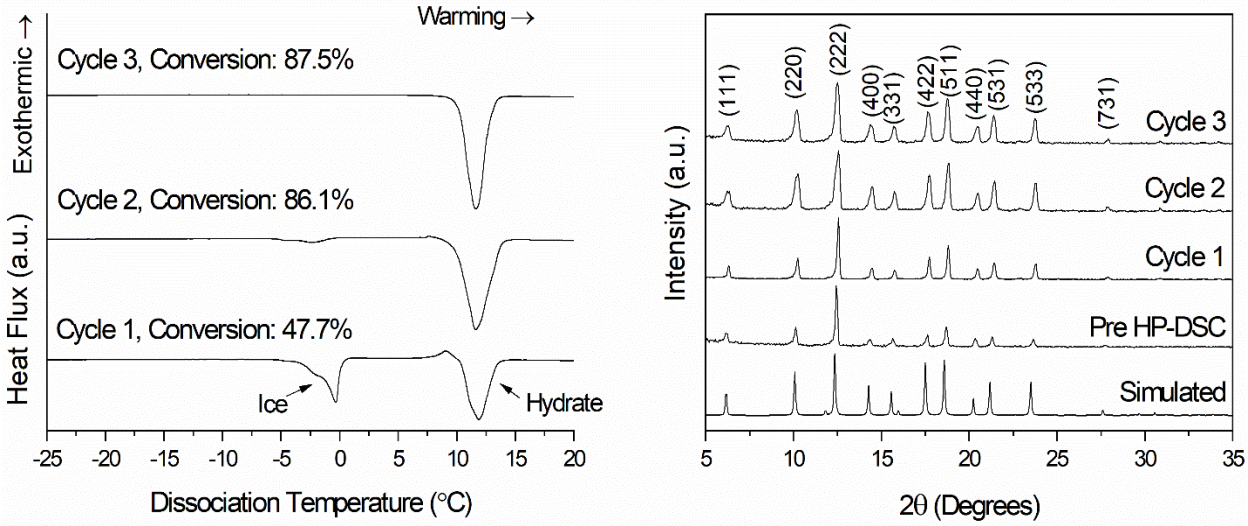

Figure 5.9 (left) HP-DSC warming profiles for CC3 over the course of 3 consecutive hydrate formation and dissociation cycles; (right) XRD patterns of simulated αCC3, sample before hydrate formation and dissociation and after 3 consecutive cycles.

For the CC3 sample subjected to 5 cycles of hydrate formation and dissociation, the second, third, fourth, and fifth cycles only deviated by ±0.2%, suggesting that any changes to the CC3 structure stops after the first cycle.

The powder XRD patterns, shown in Figure 5.10, exhibited a similar trend to the conversion: the peak widths and relative intensities change from the first cycle to the second, and then stayed consistent between the second and third cycle. Despite the change, all of the patterns match the simulated αCC3 XRD pattern well, indicating the robust structural stability of CC3. To further investigate why the change occurred, the measured peak width at half of the maximum intensity of the peak was used to calculate the average Scherrer crystallite size (i.e. single crystal size) for all the peaks using Scherrer's equation, shown in the experimental methods. The Scherrer crystallite size pre HP-DSC was 48.3±7nm, then it dropped slightly to 44.2±5nm after the first cycle, then drastically dropped to 27.6±5nm and 26.2±5nm for the second and third cycle, respectively. The similar Scherrer crystallite size of the pre HP-DSC and the post first cycle samples suggests that the amount of time exposed to the HP-DSC is what

decreases the Scherrer crystallite size. To determine the effects of time on CC3, the HP-DSC isothermal 12 hour experiments were analyzed. After the first cycle, the conversion reached 88.2%, and the powder XRD pattern revealed that the Scherrer crystallite size after the isothermal test was 27.3±5nm. Therefore, the 39% decrease in Scherrer crystallite size was most likely caused by the amount of time exposed to the HP-DSC. The smaller Scherrer crystallite size would lead to more interstitial spacing in the polycrystalline particle, resulting in enhanced water-to-hydrate conversion. Notably, the overall pore volume for the ~12-15Å pores decreased by ~3%, indicating that as the crystallites change size, some of the void spaces are lost at the expense of larger interstitial spacing forming. Furthermore, the relative peak intensity ratios for some of the CC3 planes show a similar trend to the crystallite size decrease. For the (222)/(400) peak ratios, the pre HP-DSC sample is 5.7, then it drops to 4.7 after the first cycle, and 2.71 and 3.22 after the second and third cycle, respectively. The change in peak intensity ratios is indicative of specific planes of the crystals exhibiting preferential exposure.[167] This observation could be attributed to the change in Scherrer crystallite size, as the decrease in size may also alter the crystallites' orientation.

The time length effect on the conversion in the presence of CC3 also may be influenced by the diffusion of methane and water into the structure. A study on the diffusion of methane and carbon dioxide through CC3 using a zero length column discovered that methane diffuses faster than carbon dioxide due to methane's tetrahedral shape passing through the pore pathways better than the linear shape of carbon dioxide, despite the kinetic diameter of methane (3.8Å) being larger than carbon dioxide (3.3Å).[66] When a mixture of 10:90 molar ratio of carbon dioxide to methane was flowed through CC3, the diffusion rate of methane and carbon dioxide decreased due to the competitive adsorption between the two.[32] A similar competitive adsorption effect may be restricting the flow of methane and water though the structure, as the shape of water is bent and both molecules adsorb well to CC3. Slow diffusion would require more time for the competing methane and water to diffuse through the pores to ideal hydrate nucleation sites and promote more water-to-hydrate conversion.

Representative SEM images of the synthesized CC3 sample before and after 3 cycles of hydrate formation and dissociation are shown in Figure 5.10.

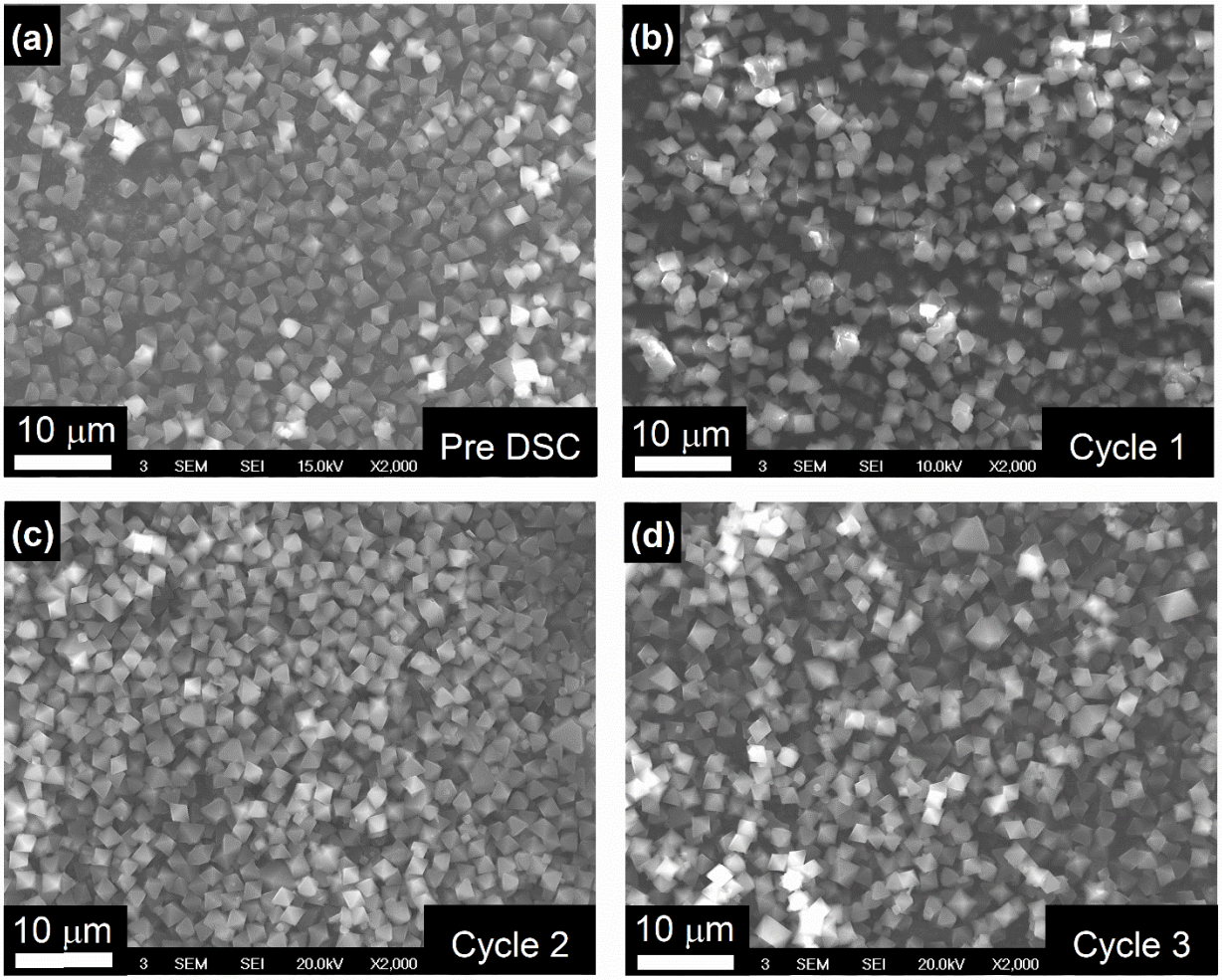

Figure 5.10 SEM images of the synthesized CC3 (a) before hydrate formation and dissociation in the HP-DSC, (b) after 1 cycles of hydrate formation and dissociation, (c) after 2 cycles, and (d) after 3 cycles.

For CC3, no morphological changes occurred. The particle size stayed consistently at 1.9±0.2μm, 1.8±0.1μm, 1.9±0.2μm, and 1.9±0.4μm for the pre HP-DSC and post HP-DSC for first, second, and third cycle, respectively. Overall, CC3 maintained its crystallinity and morphology well, indicating it is a highly recyclable hydrate promoter.

This work on CC3 uses similar experimental conditions as our previous studies on metal organic frameworks HKUST-1[52], and ZIFs [92]. While CC3, HKUST-1, and ZIFs exhibited similar water-to-hydrate conversion, CC3 decreased the hydrate induction time in greater extent as compared to HKUST-1 and ZIFs. Furthermore, the advantage of CC3 over HKUST-1, and ZIFs is related to its more robust life cycle. Specifically, CC3 has improved water stability, and has a longer life cycle as a promoter as compared to HKUST-1 and ZIFs.

5.4 Conclusions

In summary, we demonstrate that a prototypical porous organic cage, denoted as CC3 acts as an efficient growth promoter for methane hydrate formation. Specifically, the addition of CC3 to the HP-DSC water and methane system results in a significant rise in water-to-hydrate conversion from 4.5±0.4% without CC3 to a high of 87.5±1.0% with CC3 (for second and third cycle). The increase in hydrate growth results from CC3's high methane adsorption capacity and large surface area. The presence of CC3 induced a reduction in the hydrate dissociation temperature, going from 11.5±0.1ºC without CC3 to as low as 9.9±0.5ºC with CC3. This reduction suggests that hydrate formation took place in a confined space. Argon isotherms at 87K determined that the intrinsic pore size is 5Å and a secondary pore size at approximately 15Å, representing ~5% of the total pores. The secondary pore corresponds to void spaces in the cage packing, a size which can encompass a methane hydrate unit cell, 12Å. Hydrate formation also induced a decrease in CC3 crystallite size from 48.3nm to 26.2nm, which provided more interstitial spacing and thus increased the hydrate conversion after the first cycle of hydrate formation and dissociation. Addition of CC3 resulted in consistent hydrate formation in 0.8±0.1 hours, whereas a system without CC3 only formed hydrates 2 out of 6 times. The likely reasons for the consistency are the synergistic effects of the high methane adsorbed (source of methane for hydrate formation) and the reversible water uptake (water in pores acts as hydrate nucleation site). The remarkably enhanced performance of CC3 as a methane hydrate growth promoter and its robust structural integrity makes it a highly appealing material for effective methane storage in gas hydrates.

CHAPTER 6
PROMOTING METHANE HYDRATE FORMATION FOR NATURAL GAS STORAGE OVER CHABAZIE ZEOLITES

Modified from: S. Denning, A.AA. Majid, J.M. Crawford, M.A. Carreon, C.A. Koh*, "Promoting Methane Hydrate Formation for Natural Gas Storage Over Chabazite Zeolites" Under review: *ACS Applied Energy Materials, **2021***

This chapter describes the study of the hydrophobicity of zeolites effects methane hydrate formation. These findings are under review in *ACS Applied Energy Materials, **2021***.

6.1 Chabazite Zeolites

A wide assortment of porous materials are undergoing research, such as organic (e.g. activated carbon[82]), hybrid organic-inorganic (e.g. metal organic frameworks[26,81,87,97,187]), and inorganic (e.g. zeolites[96,97]) among others. Zeolites are suitable porous materials due to their high mechanical and thermal stability, high surface areas, and tunable surface chemistry. As far as the authors are aware, few zeolites have been reported as methane hydrate promoters: RHO,[96] 13A,[97] 13X,[89,97], 3A,[98] and 5A.[97,99]

Two small pore zeolites suitable as promoters for methane hydrate formation are SAPO-34 and SSZ-13. These zeolites crystallize in the same chabazite topology, illustrated in Figure 6.1, thus both have limiting pore apertures of 3.8Å, internal pore diameter of ~7.4Å, and surface areas in the ~ 450-550 m^2/g range.[50,188]

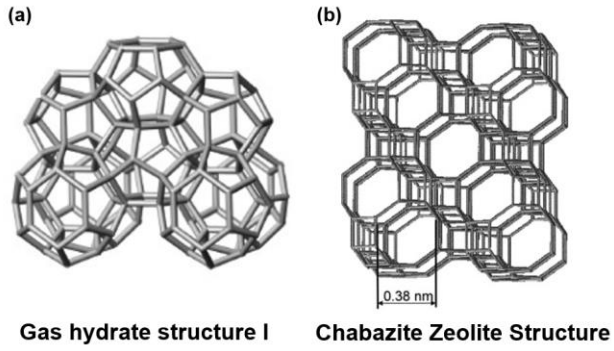

Figure 6.1 Representative illustrations of (a) gas hydrate structure I with unit cell diameter 1.2nm[11,189] and (b) chabazite zeolite structure with a limiting pore window of 0.38 nm.[50] Note, not to scale.

These zeolites differ in composition and surface chemistry: SAPO-34 contains silica, alumina, and phosphate leading to a relatively hydrophilic surface[190] whereas SSZ-13 only contains only silica and alumina, resulting in a more hydrophobic surface.[191] Hydrophobicity influences methane hydrate formation due to its effect on the tetrahedral water ordering needed for hydrate formation.[149,192] A comparison of SAPO-34 and SSZ-13 would provide insight into the effect of hydrophobicity in methane hydrate formation without variance from pore structure differences.

6.2 Experimental Methods

The following sections describe the synthesis procedures for the two zeolites, SAPO-34 and SSZ-13, along with the characterization techniques, procedure for operating the high pressure differential scanning calorimeter (HP-DSC), and calculations for the water-to-hydrate conversion.

6.2.1 SAPO-34 Materials & Synthesis Procedure

The procedure for synthesis is similar to that of other work in our group.[45,193] First, aluminum isopropoxide (Al(i-C3H7O)3, 99.99%, Sigma-Aldrich) was mixed with deionized water and stirred for 1 hour. Second, phosphoric acid (H3PO4, 85 wt.% aqueous solution, Sigma-Aldrich) was added, and the solution stirred for 2 hours. Third, Ludox AS-40 colloidal silica (40 wt.% suspended in H2O, Sigma-Aldrich) was added and then the solution was stirred for 3 hours. Fourth, tetraethylammonium hydroxide (TEAOH, 35 wt.% in aqueous solution, Sigma-Aldrich) was added, and the solution stirred 1 hour. Lastly, dipropylamine (DPA, 99% Acros Organics) was added. The resulting solution contained the following molar ratios: 1.0 Al_2O_3: 2.0 P_2O_5: 0.6 SiO_2: 1.0 TEAOH: 1.6 DPA: 100 H_2O. The solution was aged for 4 days at 45-50ºC with constant stirring. Hydrothermal treatment took place in a Teflon lined autoclave (4744 General Acid Digestion Vessel, 45 mL, Parr Instrument) heated to 220ºC for 6 hours in a conventional oven (Neytech, Vulcan Multi-stage Programmable Furnace, Model 3-550, 550 cu. in., Digital, 9-Stage Program, 120V, 50/60Hz). The autoclave was rapidly cooled. The resulting solution was centrifuged to separate out the crystals, and then the crystals were washed via centrifugation in water for 5 minutes at 4000 rpm for a total of 3 times. The crystals were dried at 110ºC overnight and then calcined at 400ºC for 4 hours with a heating/cooling rate of 0.8ºC/minute in a conventional oven.

6.2.2 SSZ-13 Materials & Synthesis Procedure

The method for synthesizing SSZ-13 stems from other works.[58] Aluminum hydroxide powder (50% Al_2O_3, Rehis F-2000 dried gel) and sodium hydroxide tablets (Baker, reagent grade) were mixed with deionized water and stirred for 1 hour at room temperature. *N*,*N*,*N*,trimethyl-1-adamantammonium hydroxide (TMAdaOH, 25% in aqueous solution, ZeoGen™ SACHEM) was added dropwise over a 15 minute interval, then the solution was stirred for 1 hour. Colloidal silica (Ludox TM-40, Sigma-Aldrich) was added dropwise, resulting in a solution with the following molar ratios: 5 Na: 5 Al_2O_3: 100 SiO_2: 12,000 H_2O: 50 TMAdaOH. Then, the solution was aged via stirring overnight at room temperature. The solution was added to a Teflon lined autoclave (4744 General Acid Digestion Vessel, 45 mL, Parr Instrument) and hydrothermally treated in a conventional oven (Neytech, Vulcan Multi-stage Programmable Furnace, Model 3-550, 550 cu. in., Digital, 9-Stage Program, 120V, 50/60Hz) at 160ºC for 48 hours. Deionized water was used to wash the resulting solution using centrifugation at 4000 rpm for 5 minutes three times. The washed crystals were dried overnight at 100ºC. The dried crystals were calcined for 6 hours at 400ºC in a conventional oven with heat/cooling rate of 0.5ºC/minute.

6.2.3 Methods for Characterizing SAPO-34 & SSZ-13

The crystallinity of the zeolites SAPO-34 and SSZ-13 was derived from powder X-ray diffraction (XRD) patterns that were measured using a Siemens Kristalloflex 810 diffractometer with a voltage of 30 kV, a current of 25 mA, with Cu Kα1 (wavelength of 1.54059Å). The morphology of the zeolites was observed using a field emission scanning electron microscopy (SEM) JEOL JSM-7000F. The porosity and surface area were measured using an ASAP 2020 porosimeter (Micromeritics, Norcross, GA, USA) to obtain a nitrogen isotherm at -196ºC and a methane isotherm at 20ºC after degassing the sample 10 hours at 300ºC. Water adsorption at 1 bar and room temperature were collected by degassing the sample using the same instrument at 300ºC for 10 hours, weighing the sample, then exposing the sample to a humid environment until mass stayed constant.

6.2.4 High Pressure Differential Scanning Calorimeter (HP-DSC) Methods

The high pressure differential scanning calorimeter (HP-DSC) used was VIIa Seteram Inc. at a resolution of 0.04 μW. The operating limitations were -45ºC to 120ºC (±0.2ºC) and 0.1MPa to 15.4MPa (±25kPa). The schematic of the HP-DSC is given in Figure 6.2.[26,121]

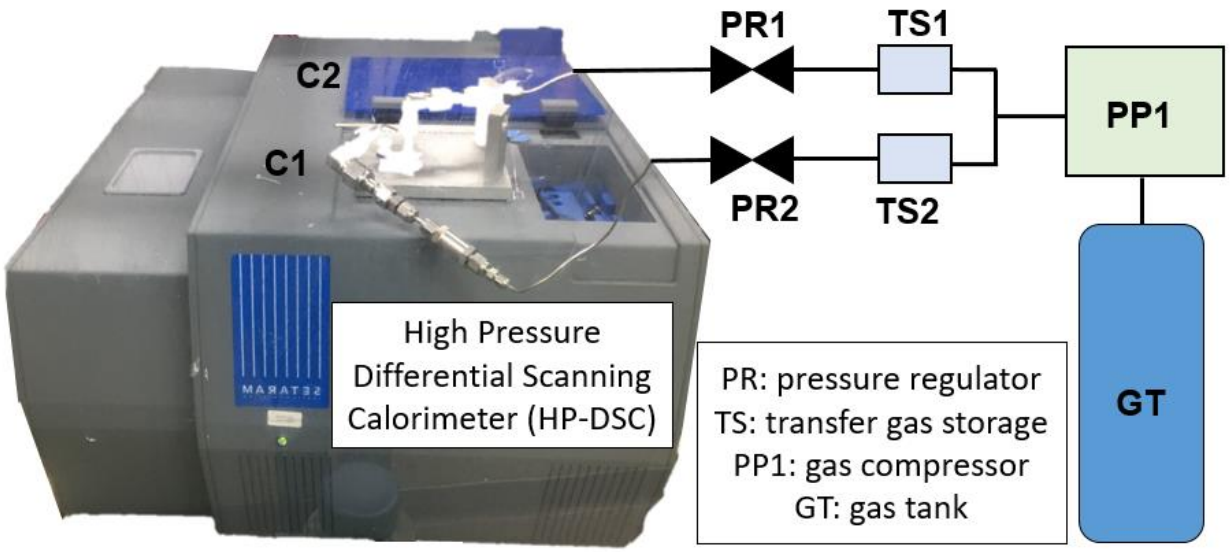

Figure 6.2 Schematic of the VIIa Seteram Inc. high pressure differential scanning calorimeter.[26,121]

A scanning HP-DSC procedure was executed, using similar conditions to previous work from our group.[26] The samples were prepared by first pipetting deionized water into the HP-DSC cell. Second, the powder zeolite (either SAPO-34 or SSZ-13) was added. The mass of the zeolite was varied to achieve different water to zeolite mass ratios (R_w). The HP-DSC cell, using two O-rings (Oil-Resistant Mil. Spec. Dash No. 006,-65°F to 275°F and Square-Profile Oil-Resistant Buna-N O-Ring, Dash Number 006), was sealed and then inserted into the HP-DSC. Then the HP-DSC cell was pressurized with methane (Matherson, 99%) to 8.0MPa.

The steps for the scanning procedure are the following: temperature raised to 30℃ at 0.5℃/min; held at 30℃ for 3 hours; temperature decreased to -30℃ at 0.3℃/min and then increased to 30℃ at the same rate for at least 3 consecutive cycles to ensure reproducibility.

6.2.5 Water-to-Hydrate Calculations

The HP-DSC experiments measure the heat flux as a function of time as the system is undergoing a change in temperature at a constant pressure. To calculate the water-to-hydrate conversion, the area under the endothermic peak (H_{diss}), indicative of hydrate formation, is put into the following equation[26,121]:

$$\text{Hydrate Conversion (\%)} = 100 * \frac{H_{diss} * MW_{H2O} * n_{HYD}}{H_{HYD}} \quad (6.1)$$

In the equation, MW_{H2O} is the molecular weight of water (18 g/mol.), n_{HYD} is the hydration number (5.9)[121], and H_{HYD} is the heat of dissociation associated with structure I methane hydrate (54.4 kJ/mol.).[122]

6.3 Results & Discussion

In this study, we determined the performance of SAPO-34 and SSZ-13 in promoting methane hydrate formation. Without any zeolite present in the HP-DSC, only 5.8±1.4% of the water was converted into hydrate. SSZ-13, the more hydrophobic zeolite due to the high Si/Al ratio in its framework, converted as high as 91.3±0.5% water to hydrate, whereas SAPO-34, the more hydrophilic of the two zeolites due to its low Si/Al, only converted as high as 38.4±1.5%. Thus, SSZ-13 outperformed SAPO-34 as a promoter for improving water-to-hydrate conversion, as evident in Figure 6.3.

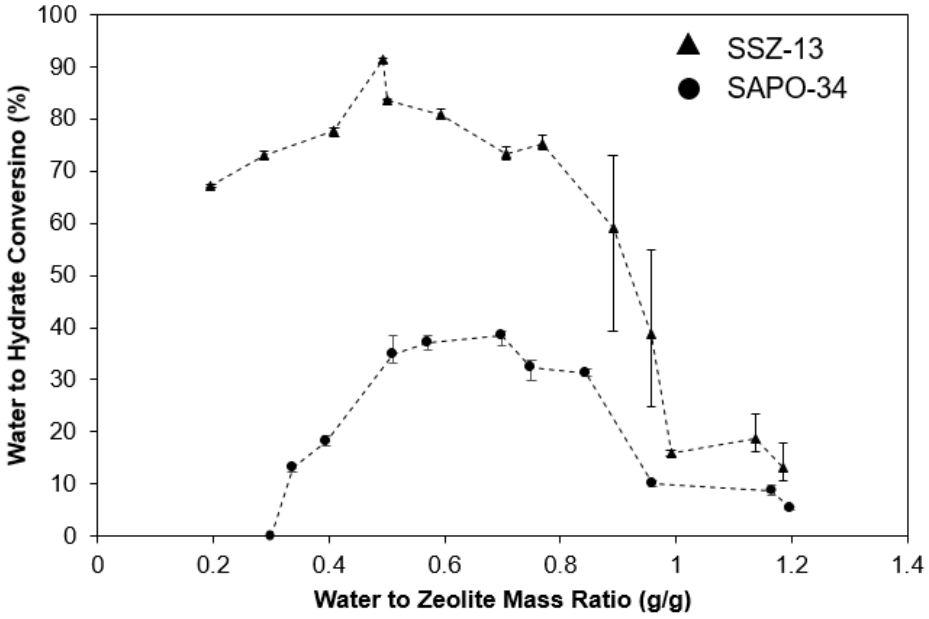

Figure 6.3 Water to hydrate conversion as a function of the water to zeolite mass ratio for SSZ-13 and SAPO-34. Results from scanning procedure in the HP-DSC conducted at 8.0MPa.

The amount of hydrate converted for both zeolites depended upon the mass ratio of water to zeolite (R_w). The values reported in Figure 6.3 are summarized in Tables 6.1 and 6.2 for SAPO-34 and SSZ-13, respectively.

Table 6.1 The water-to-hydrate conversion and hydrate dissociation temperature results from the HP-DSC for systems with and without SAPO-34 at various water to SAPO-34 mass ratios.

Mass Ratio SAPO-34 to H_2O (R_w)	Water-to-Hydrate Conversion (%)	Hydrate Dissociation Temperature (°C)
No SAPO-34*	5.8±1.4	11.4±0.23
0.3	0.0	-
0.34	13.1±0.7	10.3±0.07
0.40	18.1±1.1	10.5±0.003
0.51	35.0±3.0	10.9±0.05
0.57	37.0±1.4	10.9±0.01
0.70	38.4±1.5	11.1±0.03
0.75	32.3±2.2	11.2±0.03
0.85	31.3±0.6	11.2±0.03
0.96	10.1±0.7	11.5±0.03
1.16	8.7±1.4	11.4±0.05
1.20	5.3±0.3	11.8±0.02

Each test repeated 3 times to ensure reproducibility
*Test repeated 14 times

Table 6.2 The water-to-hydrate conversion and hydrate dissociation temperature results from the HP-DSC for systems with and without SSZ-13 at various water to SSZ-13 mass ratios.

Mass Ratio SSZ-13 to H_2O (R_w)	Water-to-Hydrate Conversion (%)	Hydrate Dissociation Temperature (°C)
No SSZ-13*	5.8±1.4	11.4±0.23
0.20	67.3±0.3	11.1±0.07
0.29	73.0±0.8	11.0±0.10
0.41	77.6±0.8	11.1±0.11
0.49	91.3±0.5	11.3±0.07
0.50**	83.5±0.2	10.6±0.05
0.59	80.9±0.9	11.3±0.09
0.71	73.3±1.3	11.3±0.06
0.77	75.3±1.5	11.3±0.08
0.89	59.2±17.6	11.3±0.15
0.96	38.6±15.2	11.4±0.10
0.99	15.8±0.6	11.5±0.02
1.14	18.7±4.1	11.4±0.01
1.19	13.1±2.8	11.4±0.05

Each test repeated 3 times to ensure reproducibility
*Test repeated 14 times
**Test repeated 5 times

The warming HP-DSC profiles corresponding to each R_w are given, respectively, in Figures 6.4 and 6.5.

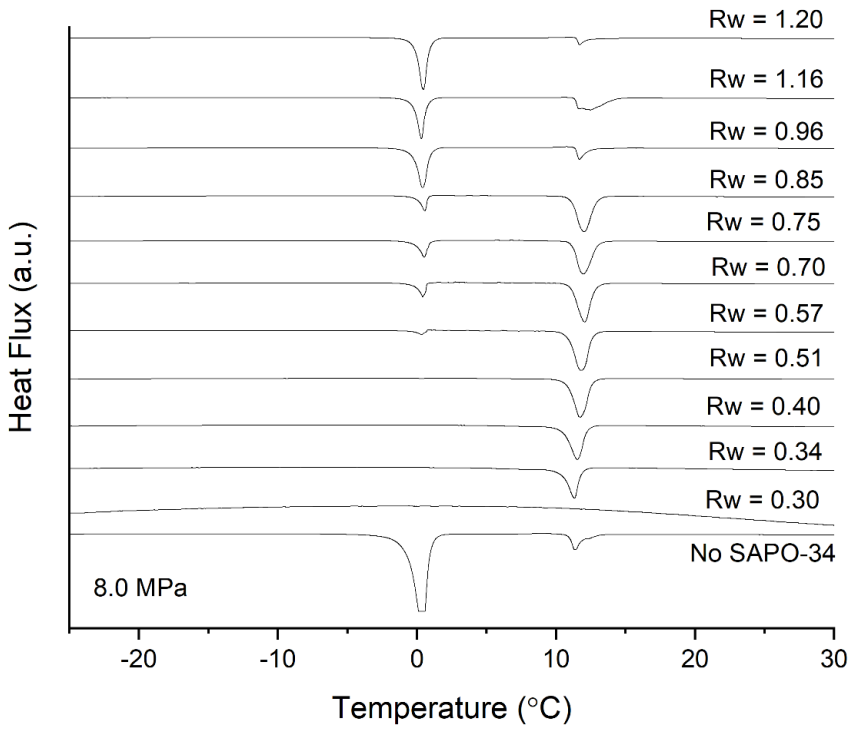

Figure 6.4 HP-DSC warming profiles for systems with and without SAPO-34 at different water to zeolite mass ratios, conducted at 8.0MPa.

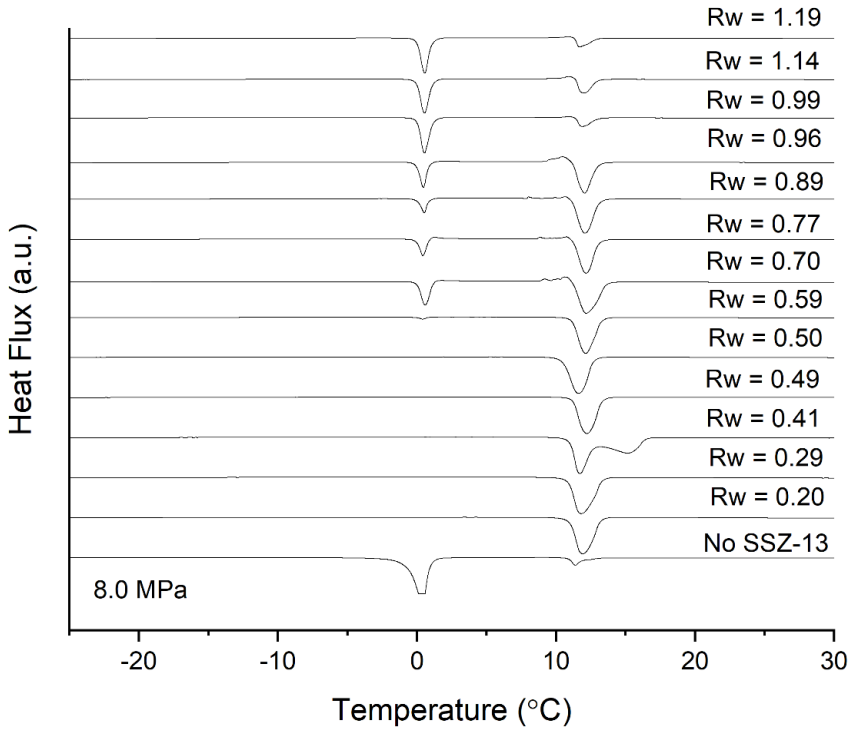

Figure 6.5 HP-DSC warming profiles for systems with and without SSZ-13 at different water to zeolite mass ratios, conducted at 8.0MPa

Both zeolites promote hydrate growth at their respective optimal mass ratios as a result of their large surface areas leading to an enhanced gas-to-water contact area. Notably, no hydrates should form inside of the pores as the pores of these zeolites (0.74 nm in diameter)[188] are too small for the methane hydrate structure I unit cell (1.2 nm).[11]

The discrepancy in water-to-hydrate conversion between SSZ-13 and SAPO-34 is associated with the zeolite's hydrophobicity which affects the wetting of the zeolite particles. The amount of water adsorbed by SSZ-13 (7 mmol/g) is significantly less than that of SAPO-34 (16 mmol/g), indicating that SSZ-13 is more hydrophobic in comparison to the hydrophilic SAPO-34. The effect of hydrophilicity arises especially in the water to zeolite mass ratio (R_w) of 0.3, denoted as a partially saturated bed. At this R_w, SSZ-13 converted 73.0±0.8% of water into hydrate, and does not form any ice. This observation results from the hydrophobicity of SSZ-13 causing high adsorption of methane in its pores and on the external surface of the particles, which can them to be consumed in hydrate formation, as depicted in Figure 6.6(a).

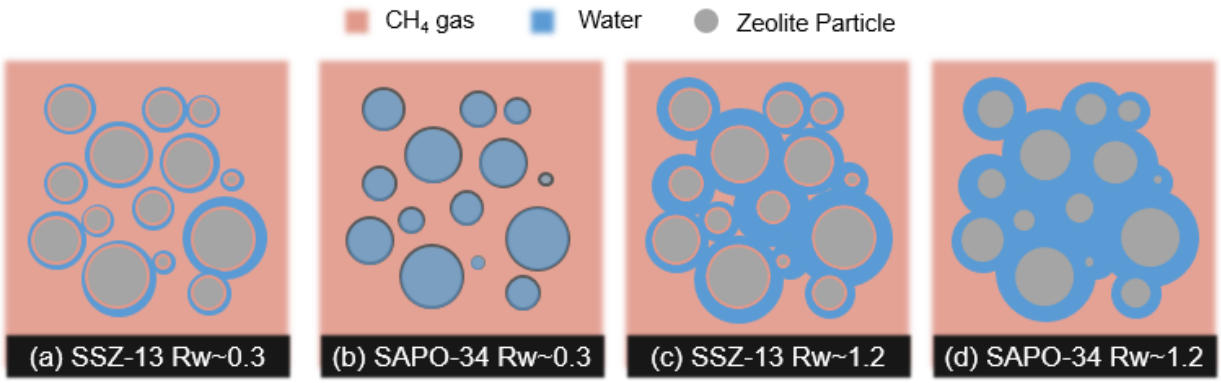

Figure 6.6 Illustration of packing in (a) partially saturated SSZ-13 bed, (b) partially saturated SAPO-34 bed, (c) oversaturated SSZ-13 bed, and (d) oversaturated SAPO-34 bed.[149] Pink represents methane gas, blue represents water, and grey represents zeolite particles.

The large surface area of SSZ-13 results in a thin water layer around the particles, which in principle would promote a thin layer of hydrate formation and thus explain the lack of ice formation. In comparison, in a partially saturated bed of SAPO-34 with an R_w=0.3, no hydrate nor ice formation was observed. Therefore, all of the water in the HP-DSC system fills the

SAPO-34 pores, as illustrated in Figure 6.6(b) where the zeolite particles are tinted blue.[190] The lack of water outside of the SAPO-34 particles results in no formation of hydrate nor ice.

The difference in optimal R_w for the two zeolites also supports the hypothesis that hydrophobicity plays a primary role in how a zeolite can promote water-to-hydrate conversion. As evident in Figure 6.3, the optimal R_w for SSZ-13 (R_w=0.49) is lower than the optimal for SAPO-34 (R_w=0.7). The system with SAPO-34 requires more water to reach its optimal ratio due to the hydrophilicity preferentially filling the pores of SAPO-34 with water. This trapped water cannot convert to hydrate as the pores of SAPO-34 are too small. Thus, a higher ratio of water to zeolite is necessary to create the desirable thin layer of water around the SAPO-34 particles, as the thin layer maximizes the gas-to-water contact area. The relative hydrophobicity of SSZ-13 does not preferentially fill its pores with water, consequently the desirable thin layer of water is reached at a lower water to zeolite ratio.

In the oversaturated saturated scenario (R_w>1.2), SSZ-13 converts more than twice as much hydrate as SAPO-34 (13.1% versus 5.3%, respectively). This difference could result from the adsorbed methane on the surface of SSZ-13 (both inside the pores and on the external surface) creating a thin layer of methane or methane bubbles on the external surface of the particle, illustrated in Figure 6.6(c). The adsorbed methane may be consumed in methane hydrate formation, resulting in an overall increased gas-to-water contact area relative to a system without any hydrates. Despite SSZ-13 and SAPO-34 adsorbing a similar amount of methane (0.53 mmol/g versus 0.52 mmol/g at 1 bar and 20ºC, respectively), the competitive adsorption between water and methane dominates how much methane is adsorbed in the hydrate formation conditions. The methane adsorption isotherms are shown in Figure 6.7.

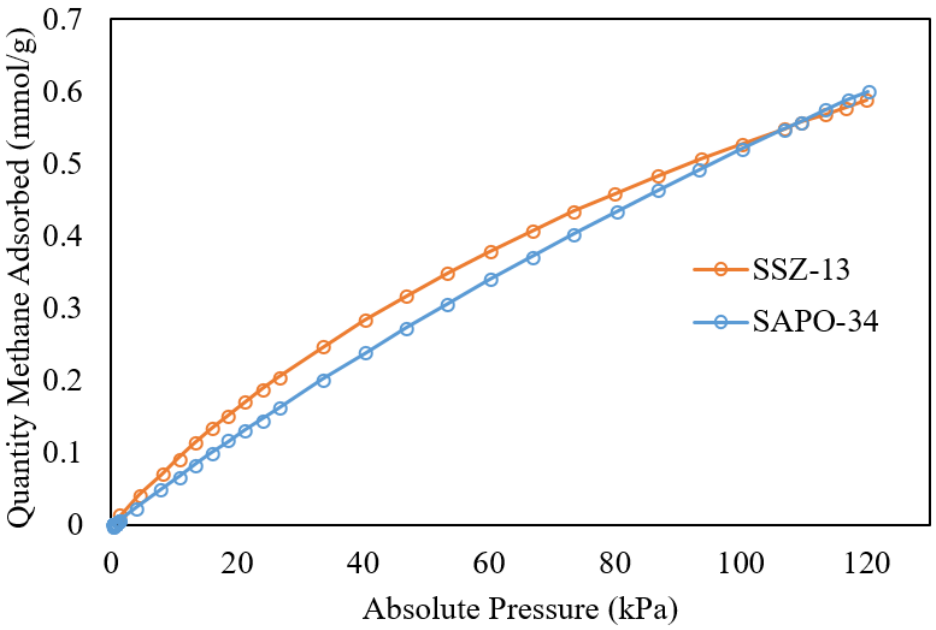

Figure 6.7 Methane adsorption isotherms conducted at 293K for the synthesized SAPO-34 and SSZ-13.

The ratio of water to methane adsorbed for SAPO-34 is 31.5, which is 2.4 times more than SSZ-13 at 13.1. Note, that these ratios are similar to a previous study on the adsorption of methane and water on these zeolites.[194] Similar to the low R_w scenario with SAPO-34, at the high R_w the water blocks the pores. A study on how humidity affects SAPO-34 found that the adsorbed water completely blocked the pores, preventing the permeation of methane through the material.[190] These observations aid in explaining why at R_w~1.2, the conversion in a system with SAPO-34 (5.3±0.3%) is nearly the same as a system without any zeolite (5.8±1.4%). The lack of readily available adsorbed methane on SAPO-34 is illustrated in Figure 6.6(d). The competitive adsorption affects the performance of the zeolites at all other water to zeolite mass ratios, with conversions averaging 2.6 times more for SSZ-13 compared to SAPO-34.

Interestingly, both zeolites showed a similar trend with regard to their effect on the hydrate dissociation temperature. As the amount of water in the system decreased (i.e., zeolite to water mass ratio decreased), the dissociation temperature decreased, as shown in Figure 6.8.

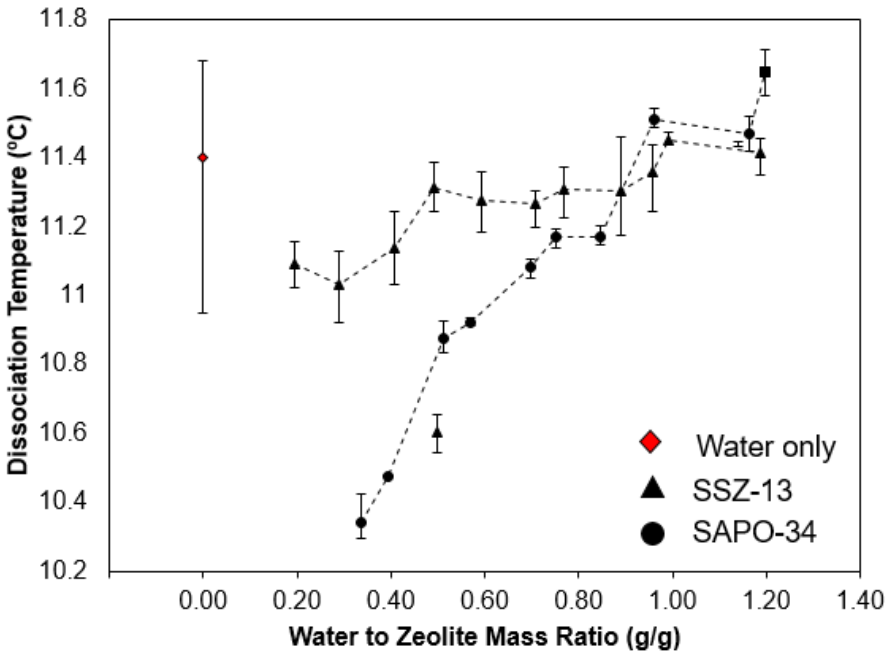

Figure 6.8 Hydrate dissociation temperature for bulk water (red diamond) and for different water to zeolite mass ratios for SSZ-13 (black triangle) and SAPO-34 (black circles).

Although the difference in dissociation temperature (system without zeolite versus system with zeolite) is nearly commensurate with the precision of the HP-DSC (±0.5ºC), the trend is distinct for each zeolite with small deviations. Previous studies found that a decrease in hydrate dissociation temperature correlates to thermodynamic inhibition, which can be caused by a confined space, such as interparticle spacing, restricting the water activity and in consequence shifting the phase envelope.[79,88] To reiterate, the pores of both zeolites in this study (~0.74 nm, shown in nitrogen adsorption isotherms at 77K in Figure 6.9) are too small for hydrate formation (unit cell size 1.2 nm) to take place within the pores, thus the formation is most likely taking place in the interparticle spacing.

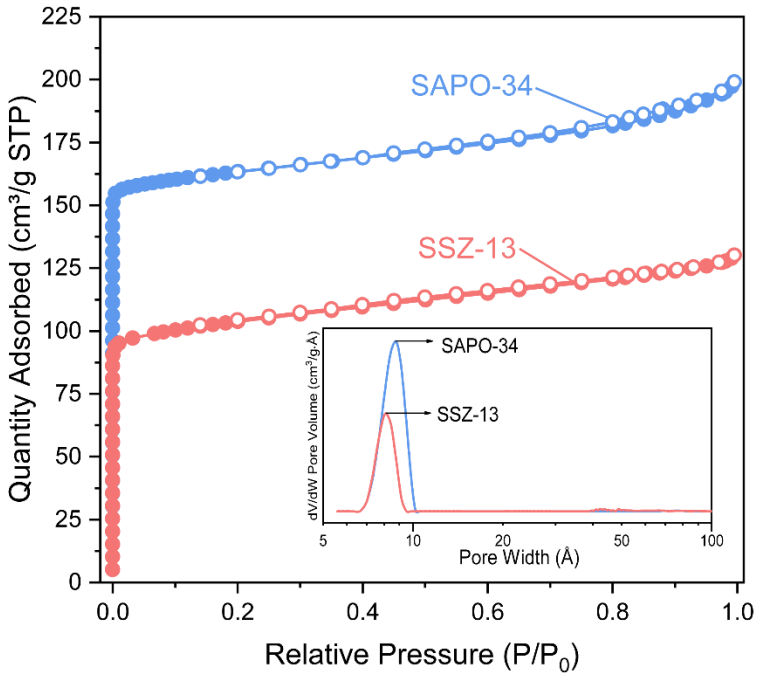

Figure 6.9 Nitrogen isotherms 77K for SAPO-34 (blue) and SSZ-13 (red) with respective NLDFT pore size distributions in the inset.

The effect of zeolite hydrophobicity on the wetting of the zeolite particles may contribute to the fact that SAPO-34 depresses the dissociation temperature at lower water content more than SSZ-13. The hydrophilicity of SAPO-34 may hold water in interstitial and interparticle spaces better than the hydrophobic SSZ-13.[149] Although at a lesser extent, the system with SSZ-13 also experiences a decreasing trend in dissociation temperature, as SSZ-13 is not completely hydrophobic due to the presence of Al in the structure (Si/Al molar ratio is 20).

Furthermore, the higher electrostatic interactions of SAPO-34 due to the high Al content and the presence of phosphorus in the structure can reduce the water activity coefficient, which can cause thermodynamic inhibition.[11] In SSZ-13, the high content of Si leads to low electrostatic interactions, yet the presence of the small amount of Al can attribute to why a small decrease is still observed. Thus, the reactivity and hydrophilicity of SAPO-34 may be the dominating factor leading to the reduced hydrate dissociation temperatures.

To ensure that a difference in zeolite particle size was not a contributing factor in hydrate formation and dissociation, SEM images of SSZ-13 and SAPO-34 were taken and the particles measured, as shown in Figure 6.10(left).

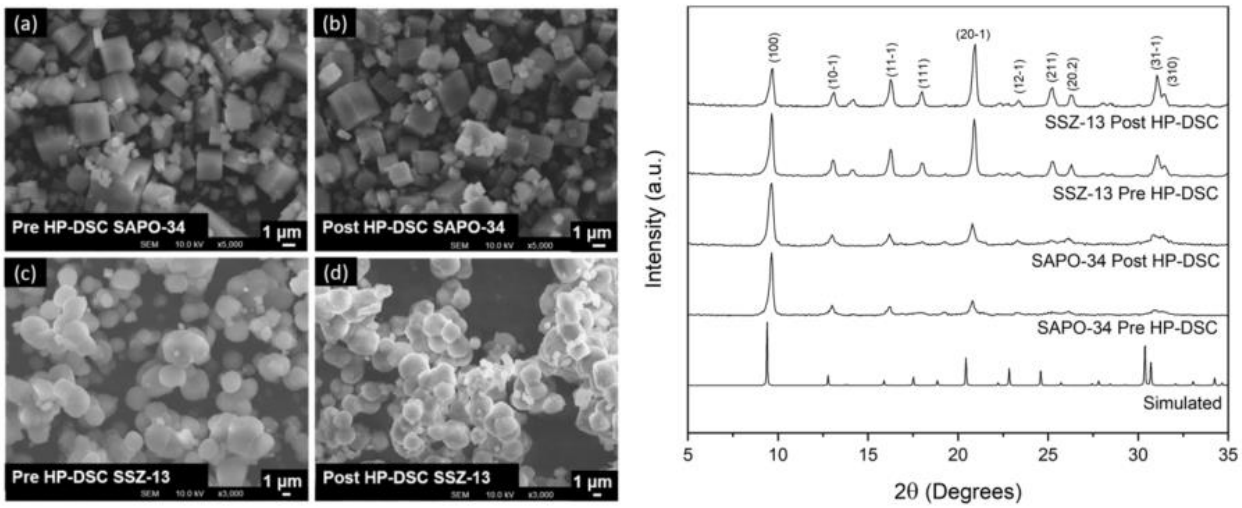

Figure 6.10 (Left) SEM images of SAPO-34 (a) pre HP-DSC and (b) post HP-DSC, and SSZ-13 (c) pre HP-DSC and (d) post HP-DSC. (Right) XRD patterns for simulated chabazite and for measured SAPO-34 and SSZ-13 pre and post HP-DSC.

The overall particle size distribution of SSZ-13 (0.51-3.76 μm) and SAPO-34 (0.38-3.64 μm) were similar. Therefore, it is unlikely that the size of the particles influenced the depressed dissociation temperature.

The XRD patterns, given in Figure 6.10(right), show that the synthesized zeolites match the simulated chabazite zeolite pattern well. Although both pre and post HP-DSC zeolite patterns exhibit no observable change in peak location, the intensity ratios of the peaks change slightly for both zeolites. The (100)/(20-1) plane intensity ratio decreased by a factor of 1.45 for SAPO-34 and 0.48 for SSZ-13. This change in preferential plane exposure may result from water influencing the crystallinity of the samples. As expected, SAPO-34 exhibits a larger change, as one study in the literature found that in a humid environment, SAPO-34 was prone to degrade to a greater extent over time.[190] The higher stability of SSZ-13 also stems from its higher Si/Al ratio as compared to SAPO-34 with a low Si/Al ratio, as one study found that the stability of these zeolites in humid environments increased with increasing Si/Al ratios.[195]

Overall, both SAPO-34 and SSZ-13 maintain their morphology and crystallinity after three consecutive cycles of hydrate formation and dissociation, as evident in the SEM images and XRD patterns given in Figure 5. This structural integrity indicates that the zeolites are recyclable, giving the material a long lifecycle as a hydrate promoter.

The previous work completed by our group using metal organic framework HKUST-1, ZIF-8, and ZIF-67 as methane hydrate promoters exhibited similar high water-to-hydrate

conversion results as SSZ-13.[26,187] The most advantageous aspect of using zeolites instead of metal organic frameworks is that the process for producing zeolites is already well established. Zeolites are composed of non-precious metals/metalloids (i.e. aluminum and silica) as compared to the metal organic frameworks which use copper (HKUST-1), zinc (ZIF-8), or cobalt (ZIF-67). Therefore, SSZ-13 is highly desirable as it provides a more cost-effective approach while also producing the same high hydrate yield.

6.4 Conclusions

In summary, we demonstrated how chabazite zeolites SSZ-13 and SAPO-34 promoted methane hydrate growth by increasing the water-to-hydrate conversion. The more hydrophobic zeolite, SSZ-13, on average over a range of different water to zeolite mass ratios converted 2.6 times more water into hydrate than SAPO-34. The outperformance of SSZ-13 is associated with its hydrophobic nature aiding in correctly orienting water molecules for hydrate formation and its lower water to methane adsorption ratio (13.1), as compared to SAPO-34 (31.5) providing an additional gas-to-water contact area at the surface of the material. The low Si/Al ratio in SAPO-34 (Si/Al of 0.6) resulted in a more electrostatic structure than SSZ-13 (Si/Al of 20), which ended up thermodynamically inhibiting the hydrates in a system with lower water content. The mechanical stability and preservation of crystal integrity after multiple cycles of hydrate formation and dissociation, combined with the induced high water-to-hydrate conversion, suggests that SSZ-13 is a highly appealing candidate as a methane hydrate promoter for natural gas storage.

CHAPTER 7
SUMMARY & FUTURE WORK RECOMMENDATIONS

7.1 Summary of Thesis Findings

In this work, the effects of selected microporous crystals on methane hydrate formation and growth were investigated. The studies focused on materials with varying chemical compositions, and included specific comparisons of microporous materials with the same topology yet different structural chemistry. The primary findings from these studies are:

1. *Large surface areas promote higher water-to-hydrate conversion*
    a. The metal organic framework HKUST-1 significantly increases the water-to-hydrate conversion for methane hydrates (14.8 times more) due to its large surface area and moderate wettability.
    b. The two metal organic frameworks ZIF-8 and ZIF-67 that share the same sodalite topology, differing only in the metal ion (zinc vs. cobalt, respectively) increased the water-to-hydrate conversion on average from 4.5% to 85.6% and 87.7%, respectively, due to both crystals exhibiting a large surface area increasing the water-to-gas contact area.
    c. The porous organic cage CC3 showed excellent promotion of water-to-hydrate conversion (from 4.5% to 87.5%) due to its large surface area, high methane adsorption capacity, and moderate hydrophobicity
    d. The zeolites SSZ-13 and SAPO-34, which share the same chabazite topology, both improved water-to-hydrate conversion from 5.8±1.4% to 91.3±0.5% and 38.4±1.5%, respectively, due to large surface areas and moderate methane adsorption.
2. *High methane adsorption shortens hydrate nucleation induction times & improves conversion*
    a. HKUST-1 reduced the ice/hydrate nucleation induction time by 4.4, as the thermal conductivity of HKUST-1 due to the copper nodes in its structure removed the local heat of hydrate formation and its high methane adsorption capacity.
    b. ZIF-8 and ZIF-67 reduced the hydrate nucleation time by 51.6% and 92.2%. The larger reduction observed for ZIF-67 stems from its larger surface area and higher methane adsorption capacity, as compared to ZIF-8.

c. CC3 reduced the hydrate nucleation induction time to 0.8 hours, as a system without CC3 only formed hydrates 30% of the time with an average formation time of 5.9 hours. The high methane adsorption capacity and reversible water uptake of CC3 attributed to this reduction, as the adsorbed methane can be consumed for hydrate formation and the hydrated CC3 pores can act as hydrate nucleation sites.
d. CC3 also induced consistent shortened hydrate nucleation induction times, ±0.1 hours, whereas a system without CC3 deviated by ±3.9 hours due to the stochastic nature of hydrate formation. Most likely the high methane adsorption tendency of CC3 keeps the methane on and in its structure before and after hydrate formation, thus keeping a readily available source of methane for hydrates to use during formation.

3. *Confined spaces reduced water activity thus depressed the hydrate dissociation temperature*
   a. Both ZIF-8 and ZIF-67 reduced the methane hydrate dissociation temperature from 11.5°C±0.1 (pure water) to 8.2°C±0.3 and 8.8°C±0.1, respectively, due to hydrate formation taking place in the confined interstitial spacing in the polycrystalline particles, which reduces the water activity leading to thermodynamic inhibition.
   b. The dissociation temperature of methane hydrates is depressed in a system with CC3, most likely due to formation taking place in void (due to uneven packing of the CC3 cages) and interstitial spacing (particles are polycrystalline) in the crystals.
   c. Both zeolites SAPO-34 and SSZ-13 induced thermodynamic inhibition at low water content due to the effects of their electrostatic structure on water activity and methane adsorption. SAPO-34 depressed the hydrate dissociation temperature at a greater extent than SSZ-13 due to the difference in electrostatic structure of the zeolites, as SSZ-13 has a higher Si/Al ratio of 20 as compared to SAPO-34 with only 0.6.
4. *Morphological changes are induced by hydrate formation*
   a. HKUST-1 exhibited signs of decomposition due to the exposure of water. This finding indicates that HKUST-1 may need to be regenerated during its lifecycle as a methane hydrate promoter.
   b. ZIF-8 underwent a morphological change after three cycles of hydrate formation and dissociation. The particles agglomerated to a uniform size, potentially due to the water molecules hydrogen bonding promoting attraction between the ZIF-8 particles until reaching a stable particle size.

5. *Maintained structural integrity/crystallinity indicates good recyclability*
    a. After subjection to multiple cycles of hydrate formation and dissociation, HKUST-1 maintained its overall crystallinity.
    b. ZIF-67 exhibited a change in relative crystallinity after the first cycle of hydrate formation and dissociation with no subsequent changes afterwards. The change most likely stems from the presence of water and the high pressure conditions causing any unused precursors to form more crystal.
    c. After experiencing one cycle of hydrate formation and dissociation, a change in crystallinity and crystallite size (39% decrease) in CC3 occurred, caused most likely by hydrate formation inside the CC3 particles halving the crystallites. The crystallite size stayed constant after consecutive cycles, indicating good overall stability.
    d. Both SAPO-34 and SSZ-13 maintained overall crystallinity and morphology along with the promotion effects show high reproducibility, indicating a long lifecycle for both zeolites as they are recycled.
6. *Hydrophobic microporous crystalline material promotes hydrate growth better than hydrophilic*
    a. SSZ-13 converted on average 2.6 times more water to hydrate than SAPO-34 due to SSZ-13 being more hydrophobic than SAPO-34. This difference occurs as SSZ-13 did not interfere as much as SAPO-34 with the water ordering required for hydrate formation as it is less electrostatic and preferentially adsorbed more methane versus water than SAPO-34 (water to methane adsorption ratio of 13.1 versus 31.5, respectively).

7.2 Recommendations for Future Work

1. Effects of Pressure on Performance of Microporous Crystals as Methane Hydrate Promoters

The work completed in this thesis focused on results obtained at 8 MPa. Some of the materials induced a degree of thermodynamic inhibition at 8 MPa (ZIF-8, ZIF-67, CC3, SAPO-34, SSZ-13)[187,196], indicating that these materials may shift the entire pressure/temperature equilibrium curve for methane hydrates. The extent of this shift at different conditions may elude to more optimum operating conditions for the formation of hydrates with these promoters.[88]

2. Scalability of Methane Hydrate Growth Promotion Performance

Although the results in the microscale high pressure differential scanning calorimeter in the materials tested show great potential for commercialization, further testing must be

conducted to determine if these results are reproducible on a large scale.[197] This is not a trivial issue, but one that deserves attention.

3. Hydrate Formation Promoter in Apparatus Optimization

The type of apparatus that these microporous crystals are introduced to in order to promote methane hydrate growth should be investigated to determine which optimizes performance.[198] The type of apparatus can affect the extent of water-to-hydrate conversion, the hydrate nucleation induction time, and the concentration of promoters needed. A study on silica sand discovered that in a large scale fixed bed, the porous material promoted hydrate growth better than that of a stirred tank.[131]

4. Application of Growth Promoters to Other Gas Hydrates

The process of utilizing gas hydrates for methane storage is not the only application of gas hydrates. Currently, studies are being performed to determine the capabilities of hydrates to capture and store carbon dioxide for sequestration.[199,200] The microporous crystals studied in this dissertation for methane hydrate growth can be applied to other gases including carbon dioxide hydrates. If these crystals are not optimal carbon dioxide hydrate growth promoters, other gases can be explored.

5. Application of Hydrates with Promoters for Gas Separation

Gas hydrates will preferentially form using a gas that stabilizes the hydrate structure better than others, making hydrates a candidate for gas separation purposes.[201] For instance, gas hydrates preferentially form with carbon dioxide as compared to methane, thus they could be applied to natural gas purification. Once studies are performed on the effects of the promoters in this dissertation on the other gas hydrates that may be present in the targeted gas mixture, then those materials could be tested to see the effect on promoting hydrate growth for selective gas capture.

6. Application of Hydrates with Promoters for Desalinization of Seawater

Another potential use of gas hydrates is for desalinization of seawater, as hydrates will exclude the salts from their structure upon formation.[202] If the hydrate promoters in this dissertation were applied to gas hydrate desalinization, then the effects of salts on these promoters in an aqueous environment would need to be studied.

7. Synergistic Effects with Other Hydrate Growth Promoters

The combination of the microporous materials in this study combined with another hydrate growth promoter may exhibit heightened performance. For example, in the case of ZIF-8 and ZIF-67, the thermodynamic inhibition induced by the effects of these materials on water activity could be reversed with the addition of a thermodynamic promoter, such as THF.[203] Other studies in the literature probed this concept, as shown with the combination of cetyl trimethyl ammonium bromide (CTAB) and copper nanoparticles,[204] indicating that similar synergistic effects could be observed with the microporous materials tested in this thesis work.

8. Ion-Exchanged Zeolites as Hydrate Promoters

Zeolites can undergo a chemical change to incorporate ions such as copper into their framework, such as SSZ-13 to Cu-SSZ-13. This exchange could take the attractive properties of zeolites (mechanical and thermal stability) and the thermal conductivity capabilities of copper to form an excellent hydrate growth promoter.

9. Compare Racemic vs. Single Chirality CC3 as Hydrate Promoters

The synthesis of the porous organic cage CC3 can use either single chirality diamines (R,R- or S,S-cyclohexanediamine) or racemic, with the former more expensive than the later. The difference in behavior exhibited, such as how racemic CC3 precipitates out of many organic solvents whereas the single chirality CC3s readily dissolve, may influence methane hydrate growth.[37]

REFERENCES

(1) Energy Information Administration, U. *International Energy Outlook 2019*; 2019.

(2) U.S. Natural Gas Total Consumption (Million Cubic Feet) https://www.eia.gov/dnav/ng/hist/n9140us2a.htm (accessed Jan 13, 2020).

(3) Ma, S.; Zhou, H. C. Gas Storage in Porous Metal-Organic Frameworks for Clean Energy Applications. *Chemical Communications*. Royal Society of Chemistry January 7, 2010, pp 44–53. https://doi.org/10.1039/b916295j.

(4) Speight, J. G. Recovery, Storage, and Transportation. In *Natural Gas*; Elsevier, 2019; pp 149–186. https://doi.org/10.1016/b978-0-12-809570-6.00005-9.

(5) Chen, Q. S.; Wegrzyn, J.; Prasad, V. Analysis of Temperature and Pressure Changes in Liquefied Natural Gas (LNG) Cryogenic Tanks. *Cryogenics (Guildf).* **2004**, *44* (10), 701–709. https://doi.org/10.1016/j.cryogenics.2004.03.020.

(6) Cracknell, R. F.; Gordon, P.; Gubbins, K. E. *Influence of Pore Geometry on the Design of Microporous Materials for Methane Storage*; 1993; Vol. 97.

(7) Morris, R. E.; Wheatley, P. S. Gas Storage in Nanoporous Materials. *Angewandte Chemie - International Edition*. John Wiley & Sons, Ltd June 23, 2008, pp 4966–4981. https://doi.org/10.1002/anie.200703934.

(8) Yilmaz, B.; Trukhan, N.; Müller, U. Industrial Outlook on Zeolites and Metal Organic Frameworks. *Cuihua Xuebao/Chinese Journal of Catalysis*. Elsevier January 1, 2012, pp 3–10. https://doi.org/10.1016/s1872-2067(10)60302-6.

(9) Menon, V. C.; Komarneni, S. Porous Adsorbents for Vehicular Natural Gas Storage: A Review. *J. Porous Mater.* **1998**, *5* (1), 43–58. https://doi.org/10.1023/A:1009673830619.

(10) Sun, Y.; Liu, C.; Su, W.; Zhou, Y.; Zhou, L. Principles of Methane Adsorption and Natural Gas Storage. *Adsorption* **2009**, *15*, 133–137. https://doi.org/10.1007/s10450-009-9157-x.

(11) Sloan, E. D.; Koh, C. A. *Clathrate Hydrates of Natural Gases*, 3rd ed.; CRC Press: Boca Raton, FL, 2008.

(12) Gudmundsson, J. S.; Parlaktuna, M.; Khokhar, A. A. Storing Natural Gas as Frozen Hydrate. *SPE Prod. Facil.* **1994**, *9* (1), 69–73. https://doi.org/10.2118/24924-pa.

(13) Sun, Z. G.; Wang, R.; Ma, R.; Guo, K.; Fan, S. Natural Gas Storage in Hydrates with the Presence of Promoters. *Energy Convers. Manag.* **2003**, *44* (17), 2733–2742. https://doi.org/10.1016/S0196-8904(03)00048-7.

(14) Gudmundsson, J.; Borrehaug, A. Frozen Hydrate for Transport of Natural Gas. In *International Conference on Natural Gas Hydrates*; Toulouse, 1996; pp 415–422.

(15) Makogon, Y. F.; Holditch, S. A.; Makogon, T. Y. Natural Gas-Hydrates - A Potential Energy Source for the 21st Century. *J. Pet. Sci. Eng.* **2007**, *56* (1–3), 14–31. https://doi.org/10.1016/j.petrol.2005.10.009.

(16) Konno, Y.; Fujii, T.; Sato, A.; Akamine, K.; Naiki, M.; Masuda, Y.; Yamamoto, K.; Nagao, J. Key Findings of the World's First Offshore Methane Hydrate Production Test off the Coast of Japan: Toward Future Commercial Production. *Energy and Fuels* **2017**, *31* (3), 2607–2616. https://doi.org/10.1021/acs.energyfuels.6b03143.

(17) Walsh, M. R.; Hancock, S. H.; Wilson, S. J.; Patil, S. L.; Moridis, G. J.; Boswell, R.; Collett, T. S.; Koh, C. A.; Sloan, E. D. Preliminary Report on the Commercial Viability of Gas Production from Natural Gas Hydrates. *Energy Econ.* **2009**, *31* (5), 815–823. https://doi.org/10.1016/j.eneco.2009.03.006.

(18) Merey, S.; Sinayuc, C. Numerical Simulations for Short-Term Depressurization Production Test of Two Gas Hydrate Sections in the Black Sea. *J. Nat. Gas Sci. Eng.* **2017**, *44*, 77–95. https://doi.org/10.1016/j.jngse.2017.04.011.

(19) Wang, B.; Dong, H.; Liu, Y.; Lv, X.; Liu, Y.; Zhao, J.; Song, Y. Evaluation of Thermal Stimulation on Gas Production from Depressurized Methane Hydrate Deposits☆. *Appl. Energy* **2018**, *227*, 710–718. https://doi.org/10.1016/j.apenergy.2017.08.005.

(20) Lee, J.; Park, S.; Sung, W. An Experimental Study on the Productivity of Dissociated Gas from Gas Hydrate by Depressurization Scheme. *Energy Convers. Manag.* **2010**, *51* (12), 2510–2515. https://doi.org/10.1016/j.enconman.2010.05.015.

(21) Boswell, R.; Hancock, S.; Yamamoto, K.; Collett, T.; Pratap, M.; Lee, S.-R. Natural Gas Hydrates. In *Future Energy*; Elsevier, 2020; pp 111–131. https://doi.org/10.1016/B978-0-08-102886-5.00006-2.

(22) Venna, S. R.; Carreon, M. A. Metal Organic Framework Membranes for Carbon Dioxide Separation. *Chem. Eng. Sci.* **2015**, *124*, 3–19. https://doi.org/10.1016/j.ces.2014.10.007.

(23) Siberio-Pérez, D. Y.; Wong-Foy, A. G.; Yaghi, O. M.; Matzger, A. J. Raman Spectroscopic Investigation of CH 4 and N 2 Adsorption in Metal-Organic Frameworks. *Chem. Mater.* **2007**, *19* (15), 3681–3685. https://doi.org/10.1021/cm070542g.

(24) Wu, H.; Simmons, J. M.; Liu, Y.; Brown, C. M.; Wang, X. Sen; Shengqian, M.; Peterson, V. K.; Southon, P. D.; Kepert, C. J.; Zhou, H. C.; Yildirim, T.; Zhou, W. Metal-Organic Frameworks with Exceptionally High Methane Uptake: Where and How Is Methane Stored? *Chem. - A Eur. J.* **2010**, *16* (17), 5205–5214. https://doi.org/10.1002/chem.200902719.

(25) Peng, Y.; Krungleviciute, V.; Eryazici, I.; Hupp, J. T.; Farha, O. K.; Yildirim, T. Methane Storage in Metal-Organic Frameworks: Current Records, Surprise Findings, and Challenges. *J. Am. Chem. Soc.* **2013**, *135* (32), 11887–11894. https://doi.org/10.1021/ja4045289.

(26) Denning, S.; Majid, A. A.; Lucero, J. M.; Crawford, J. M.; Carreon, M. A.; Koh, C. A. Metal–Organic Framework HKUST-1 Promotes Methane Hydrate Formation for Improved Gas Storage Capacity. *ACS Appl. Mater. Interfaces* **2020**, *12*, 53510–53518. https://doi.org/10.1021/acsami.0c15675.

(27) Todaro, M.; Buscarino, G.; Sciortino, L.; Alessi, A.; Messina, F.; Taddei, M.; Ranocchiari, M.; Cannas, M.; Gelardi, F. M. Decomposition Process of Carboxylate MOF

HKUST-1 Unveiled at the Atomic Scale Level. *J. Phys. Chem. C* **2016**, *120* (23), 12879–12889. https://doi.org/10.1021/acs.jpcc.6b03237.

(28) Park, K. S.; Ni, Z.; Côté, A. P.; Choi, J. Y.; Huang, R.; Uribe-Romo, F. J.; Chae, H. K.; O'Keeffe, M.; Yaghi, O. M. Exceptional Chemical and Thermal Stability of Zeolitic Imidazolate Frameworks. *Proc. Natl. Acad. Sci. U. S. A.* **2006**, *103* (27), 10186–10191. https://doi.org/10.1073/pnas.0602439103.

(29) Banerjee, R.; Phan, A.; Wang, B.; Knobler, C.; Furukawa, H.; O'Keeffe, M.; Yaghi, O. M. High-Throughput Synthesis of Zeolitic Imidazolate Frameworks and Application to CO2 Capture. *Science (80-.).* **2008**, *319* (5865), 939–943. https://doi.org/10.1126/science.1152516.

(30) Pérez-Pellitero, J.; Amrouche, H.; Siperstein, F. R.; Pirngruber, G.; Nieto-Draghi, C.; Chaplais, G.; Simon-Masseron, A.; Bazer-Bachi, D.; Peralta, D.; Bats, N. Adsorption of CO2, CH4, and N2 on Zeolitic Imidazolate Frameworks: Experiments and Simulations. *Chem. - A Eur. J.* **2010**, *16* (5), 1560–1571. https://doi.org/10.1002/chem.200902144.

(31) Wu, H.; Zhou, W.; Yildirim, T. Methane Sorption in Nanoporous Metal-Organic Frameworks and First-Order Phase Transition of Confined Methane. *J. Phys. Chem. C* **2009**, *113* (7), 3029–3035. https://doi.org/10.1021/jp8103276.

(32) Gelles, T.; Rownaghi, A. A.; Rezaei, F. Diffusion Kinetics of CO2, CH4, and Their Binary Mixtures in Porous Organic Cage CC3. *J. Phys. Chem. C* **2019**, *123* (39), 24172–24180. https://doi.org/10.1021/acs.jpcc.9b07438.

(33) Lucero, J.; Elsaidi, S. K.; Anderson, R.; Wu, T.; Gómez-Gualdrón, D. A.; Thallapally, P. K.; Carreon, M. A. Time Dependent Structural Evolution of Porous Organic Cage CC3. *Cryst. Growth Des.* **2018**, *18* (2), 921–927. https://doi.org/10.1021/acs.cgd.7b01405.

(34) Lucero, J.; Crawford, J. M.; Osuna, C.; Carreon, M. A. Solvothermal Synthesis of Porous Organic Cage CC3 in the Presence of Dimethylformamide as Solvent. *CrystEngComm* **2019**, *21* (34), 5039–5044. https://doi.org/10.1039/c9ce00662a.

(35) Lucero, J. M.; Jasinski, J. B.; Song, M.; Li, D.; Liu, L.; Liu, J.; De Yoreo, J. J.; Thallapally, P. K.; Carreon, M. A. Synthesis of Porous Organic Cage CC3 via Solvent Modulated Evaporation. *Inorganica Chim. Acta* **2020**, *501*, 119312. https://doi.org/10.1016/j.ica.2019.119312.

(36) Charles, C. D.; Bloch, E. D. High-Pressure Methane Storage and Selective Gas Adsorption in a Cyclohexane-Functionalised Porous Organic Cage. *Supramol. Chem.* **2019**, *31* (8), 508–513. https://doi.org/10.1080/10610278.2019.1630739.

(37) Slater, A. G.; Little, M. A.; Briggs, M. E.; Jelfs, K. E.; Cooper, A. I. A Solution-Processable Dissymmetric Porous Organic Cage. *Mol. Syst. Des. Eng.* **2018**, *3* (1), 223–227. https://doi.org/10.1039/c7me00090a.

(38) Mitra, T.; Wu, X.; Clowes, R.; Jones, J. T. A.; Jelfs, K. E.; Adams, D. J.; Trewin, A.; Bacsa, J.; Steiner, A.; Cooper, A. I. A Soft Porous Organic Cage Crystal with Complex Gas Sorption Behavior. *Chem. - A Eur. J.* **2011**, *17* (37), 10235–10240. https://doi.org/10.1002/chem.201101631.

(39) Lucero, J. M.; Carreon, M. A. Separation of Light Gases from Xenon over Porous Organic Cage Membranes. *ACS Appl. Mater. Interfaces* **2020**, *12* (28), 32182–32188. https://doi.org/10.1021/acsami.0c08040.

(40) Carreon, M. A. Molecular Sieve Membranes for N_2/CH_4 Separation. *J. Mater. Res.* **2018**, *33* (1), 32–43. https://doi.org/10.1557/jmr.2017.297.

(41) Kamarudin, K. S. N.; Hamdan, H.; Mat, H. *Methane Adsorption Characteristic Dependency on Zeolite Structures and Properties*; 2003.

(42) Zhang, S.-Y.; Talu, O.; Hayhurst, D. T. *High-Pressure Adsorption of Methane in NaX, MgX, CaX, SrX, and BaX*; 1991; Vol. 95.

(43) NaY, B.; Zeolites Orhan Talu, B.; Zhang, S.-Y.; Hayhurst, D. T. *Effect of Cations on Methane Adsorption by NaY, MgY, CaY, SrY, and BaY Zeolites*; 1993; Vol. 97.

(44) Breck, D. *Zeolite Molecular Sieves: Structure, Chemistry and Use*; John Wiley & Sons, Inc.: New York, 1974.

(45) Denning, S.; Lucero, J.; Koh, C. A.; Carreon, M. A. Chabazite Zeolite SAPO-34 Membranes for He/CH_4 Separation. *ACS Mater. Lett.* **2019**, *1* (6), 655–659. https://doi.org/10.1021/acsmaterialslett.9b00324.

(46) Davis, M. E. *Zeolites and Molecular Sieves: Not Just Ordinary Catalysts*; 1991; Vol. 30.

(47) File:Framework structure of CHA-type zeolites.svg - Wikimedia Commons https://commons.wikimedia.org/wiki/File:Framework_structure_of_CHA-type_zeolites.svg (accessed Jun 23, 2021).

(48) Li, S.; Falconer, J. L.; Noble, R. D. SAPO-34 Membranes for CO2/CH4 Separations: Effect of Si/Al Ratio. *Microporous Mesoporous Mater.* **2008**, *110* (2–3), 310–317. https://doi.org/10.1016/j.micromeso.2007.06.016.

(49) Carreon, M. A.; Li, S.; Falconer, J. L.; Noble, R. D. Alumina-Supported SAPO-34 Membranes for CO2/CH4 Separation. *J. Am. Chem. Soc.* **2008**, *130* (16), 5412–5413. https://doi.org/10.1021/ja801294f.

(50) Falconer, J. L.; Carreon, M. A.; Li, S.; Noble, R. D. Synthesis of Zeolites and Zeolite Membranes Using Multiple Structure Directing Agents. US No. 8302782B2, 2012.

(51) Li, S.; Zong, Z.; Zhou, S. J.; Huang, Y.; Song, Z.; Feng, X.; Zhou, R.; Meyer, H. S.; Yu, M.; Carreon, M. A. SAPO-34 Membranes for N2/CH4 Separation: Preparation, Characterization, Separation Performance and Economic Evaluation. *J. Memb. Sci.* **2015**, *487*, 141–151. https://doi.org/10.1016/j.memsci.2015.03.078.

(52) Huang, Y.; Wang, L.; Song, Z.; Li, S.; Yu, M. Back Cover: Growth of High-Quality, Thickness-Reduced Zeolite Membranes towards N_2/CH_4 Separation Using High-Aspect-Ratio Seeds (Angew. Chem. Int. Ed. 37/2015). *Angew. Chemie Int. Ed.* **2015**, *54* (37), 10986–10986. https://doi.org/10.1002/anie.201507477.

(53) Zong, Z.; Feng, X.; Huang, Y.; Song, Z.; Zhou, R.; Zhou, S. J.; Carreon, M. A.; Yu, M.; Li, S. Highly Permeable N2/CH4 Separation SAPO-34 Membranes Synthesized by

Diluted Gels and Increased Crystallization Temperature. *Microporous Mesoporous Mater.* **2016**, *224*, 36–42. https://doi.org/10.1016/j.micromeso.2015.11.014.

(54) Poshusta, J. C.; Tuan, V. A.; Pape, E. A.; Noble, R. D.; Falconer, J. L. Separation of Light Gas Mixtures Using SAPO-34 Membranes. *AIChE J.* **2000**, *46* (4), 779–789. https://doi.org/10.1002/aic.690460412.

(55) Kosinov, N.; Gascon, J.; Kapteijn, F.; Hensen, E. J. M. Recent Developments in Zeolite Membranes for Gas Separation. *J. Memb. Sci.* **2016**, *499*, 65–79. https://doi.org/10.1016/j.memsci.2015.10.049.

(56) Cui, Y.; Kita, H.; Okamoto, K. I. Preparation and Gas Separation Performance of Zeolite T Membrane. *J. Mater. Chem.* **2004**, *14* (5), 924–932. https://doi.org/10.1039/b311881a.

(57) Zheng, Y.; Hu, N.; Wang, H.; Bu, N.; Zhang, F.; Zhou, R. Preparation of Steam-Stable High-Silica CHA (SSZ-13) Membranes for CO2/CH4 and C2H4/C2H6 Separation. *J. Memb. Sci.* **2015**, *475*, 303–310. https://doi.org/10.1016/j.memsci.2014.10.048.

(58) Song, S.; Gao, F.; Zhang, Y.; Li, X.; Zhou, M.; Wang, B.; Zhou, R. Preparation of SSZ-13 Membranes with Enhanced Fluxes Using Asymmetric Alumina Supports for N2/CH4 and CO2/CH4 Separations. *Sep. Purif. Technol.* **2019**, *209*, 946–954. https://doi.org/10.1016/j.seppur.2018.09.016.

(59) Hasegawa, Y.; Tanaka, T.; Watanabe, K.; Jeong, B. H.; Kusakabe, K.; Morooka, S. Separation of CO2-CH4 and CO2-N 2 Systems Using Ion-Exchanged FAU-Type Zeolite Membranes with Different Si/Al Ratios. *Korean J. Chem. Eng.* **2002**, *19* (2), 309–313. https://doi.org/10.1007/BF02698420.

(60) van den Bergh, J.; Zhu, W.; Gascon, J.; Moulijn, J. A.; Kapteijn, F. Separation and Permeation Characteristics of a DD3R Zeolite Membrane. *J. Memb. Sci.* **2008**, *316* (1–2), 35–45. https://doi.org/10.1016/j.memsci.2007.12.051.

(61) Inkong, K.; Rangsunvigit, P.; Kulprathipanja, S.; Linga, P. Effects of Temperature and Pressure on the Methane Hydrate Formation with the Presence of Tetrahydrofuran (THF) as a Promoter in an Unstirred Tank Reactor. *Fuel* **2019**, *255*, 115705. https://doi.org/10.1016/j.fuel.2019.115705.

(62) Lafond, P. G.; Olcott, K. A.; Dendy Sloan, E.; Koh, C. A.; Sum, A. K. Measurements of Methane Hydrate Equilibrium in Systems Inhibited with NaCl and Methanol. *J. Chem. Thermodyn.* **2012**, *48*, 1–6. https://doi.org/10.1016/j.jct.2011.12.023.

(63) Koh, C. A.; Westacott, R. E.; Zhang, W.; Hirachand, K.; Creek, J. L.; Soper, A. K. Mechanisms of Gas Hydrate Formation and Inhibition. In *Fluid Phase Equilibria*; Elsevier, 2002; Vol. 194–197, pp 143–151. https://doi.org/10.1016/S0378-3812(01)00660-4.

(64) Warrier, P.; Khan, M. N.; Srivastava, V.; Maupin, C. M.; Koh, C. A. Overview: Nucleation of Clathrate Hydrates. *Journal of Chemical Physics*. American Institute of Physics Inc. December 7, 2016, p 211705. https://doi.org/10.1063/1.4968590.

(65) Davies, S. R.; Hester, K. C.; Lachance, J. W.; Koh, C. A.; Dendy Sloan, E. Studies of Hydrate Nucleation with High Pressure Differential Scanning Calorimetry. *Chem. Eng.*

Sci. **2009**, *64* (2), 370–375. https://doi.org/10.1016/j.ces.2008.10.017.

(66) Maeda, N. Interfacial Nanobubbles and the Memory Effect of Natural Gas Hydrates. *J. Phys. Chem. C* **2018**, *122* (21), 11399–11406. https://doi.org/10.1021/acs.jpcc.8b02416.

(67) Choudhary, N.; Hande, V. R.; Roy, S.; Chakrabarty, S.; Kumar, R. Effect of Sodium Dodecyl Sulfate Surfactant on Methane Hydrate Formation: A Molecular Dynamics Study. *J. Phys. Chem. B* **2018**, *122* (25), 6536–6542. https://doi.org/10.1021/acs.jpcb.8b02285.

(68) Ivall, J.; Pasieka, J.; Posteraro, D.; Servio, P. Profiling the Concentration of the Kinetic Inhibitor Polyvinylpyrrolidone throughout the Methane Hydrate Rormation Process. *Energy and Fuels* **2015**, *29* (4), 2329–2335. https://doi.org/10.1021/acs.energyfuels.5b00145.

(69) Freer, E. M.; Sami Selim, M.; Dendy Sloan, E. Methane Hydrate Film Growth Kinetics. *Fluid Phase Equilib.* **2001**, *185* (1–2), 65–75. https://doi.org/10.1016/S0378-3812(01)00457-5.

(70) Luo, Y. T.; Zhu, J. H.; Fan, S. S.; Chen, G. J. Study on the Kinetics of Hydrate Formation in a Bubble Column. *Chem. Eng. Sci.* **2007**, *62* (4), 1000–1009. https://doi.org/10.1016/j.ces.2006.11.004.

(71) Veluswamy, H. P.; Kumar, A.; Kumar, R.; Linga, P. An Innovative Approach to Enhance Methane Hydrate Formation Kinetics with Leucine for Energy Storage Application. *Appl. Energy* **2017**, *188*, 190–199. https://doi.org/10.1016/j.apenergy.2016.12.002.

(72) Uchida, T.; Ebinuma, T.; Takeya, S.; Nagao, J.; Narita, H. Effects of Pore Sizes on Dissociation Temperatures and Pressures of Methane, Carbon Dioxide, and Propane Hydrates in Porous Media. *J. Phys. Chem. B* **2002**, *106* (4), 820–826. https://doi.org/10.1021/jp012823w.

(73) Cuadrado-Collados, C.; Mouchaham, G.; Daemen, L.; Cheng, Y.; Ramirez-Cuesta, A.; Aggarwal, H.; Missyul, A.; Eddaoudi, M.; Belmabkhout, Y.; Silvestre-Albero, J. Quest for an Optimal Methane Hydrate Formation in the Pores of Hydrolytically Stable Metal-Organic Frameworks. *J. Am. Chem. Soc.* **2020**, *142* (31), 13391–13397. https://doi.org/10.1021/jacs.0c01459.

(74) Lee, J.; Shin, C.; Lee, Y. Experimental Investigation to Improve the Storage Potentials of Gas Hydrate under the Unstirring Condition. *Energy and Fuels* **2010**, *24* (2), 1129–1134. https://doi.org/10.1021/ef901020g.

(75) Majid, A. A. A.; Koh, C. A. Self-Preservation Phenomenon in Gas Hydrates and Its Application for Energy Storage. In *Intra- and Intermolecular Interactions Between Non-covalently Bonded Species*; Elsevier, 2021; pp 267–285. https://doi.org/10.1016/b978-0-12-817586-6.00008-6.

(76) Stern, L. A.; Circone, S.; Kirby, S. H.; Durham, W. B. Anomalous Preservation of Pure Methane Hydrate at 1 Atm. *J. Phys. Chem. B* **2001**, *105* (9), 1756–1762. https://doi.org/10.1021/jp003061s.

(77) Stern, L. A.; Circone, S.; Kirby, S. H.; Durham, W. B. Temperature, Pressure, and

Compositional Effects on Anomalous or "Self" Preservation of Gas Hydrates. *Can. J. Phys.* **2003**, *81* (1–2), 271–283. https://doi.org/10.1139/p03-018.

(78) Casco, M. E.; Zhang, E.; Grätz, S.; Krause, S.; Bon, V.; Wallacher, D.; Grimm, N.; Többens, D. M.; Hauß, T.; Borchardt, L. Experimental Evidence of Confined Methane Hydrate in Hydrophilic and Hydrophobic Model Carbons. *J. Phys. Chem. C* **2019**, *123* (39), 24071–24079. https://doi.org/10.1021/acs.jpcc.9b06366.

(79) Borchardt, L.; Casco, M. E.; Silvestre-Albero, J. Methane Hydrate in Confined Spaces: An Alternative Storage System. *ChemPhysChem* **2018**, *19* (11), 1298–1314. https://doi.org/10.1002/cphc.201701250.

(80) Cha, S. B.; Ouar, H.; Wildeman, T. R.; Sloan, E. D. A Third-Surface Effect on Hydrate Formation. *J. Phys. Chem* **1988**, *92*, 6492–6494.

(81) Cuadrado-Collados, C.; Mouchaham, G.; Daemen, L.; Cheng, Y.; Ramirez-Cuesta, A.; Aggarwal, H.; Missyul, A.; Eddaoudi, M.; Belmabkhout, Y.; Silvestre-Albero, J. Quest for an Optimal Methane Hydrate Formation in the Pores of Hydrolytically Stable Metal-Organic Frameworks. *J. Am. Chem. Soc.* **2020**, *142* (31), 13391–13397. https://doi.org/10.1021/jacs.0c01459.

(82) Cuadrado-Collados, C.; Majid, A. A. A.; Martínez-Escandell, M.; Daemen, L. L.; Missyul, A.; Koh, C.; Silvestre-Albero, J. Freezing/Melting of Water in the Confined Nanospace of Carbon Materials: Effect of an External Stimulus. *Carbon N. Y.* **2020**, *158*, 346–355. https://doi.org/10.1016/j.carbon.2019.10.081.

(83) Govindaraj, V.; Mech, D.; Pandey, G.; Nagarajan, R.; Sangwai, J. S. Kinetics of Methane Hydrate Formation in the Presence of Activated Carbon and Nano-Silica Suspensions in Pure Water. *J. Nat. Gas Sci. Eng.* **2015**, *26*, 810–818. https://doi.org/10.1016/j.jngse.2015.07.011.

(84) Liu, J.; Wei, Y.; Meng, W.; Li, P.-Z.; Zhao, Y.; Zou, R. Understanding the Pathway of Gas Hydrate Formation with Porous Materials for Enhanced Gas Separation. *Research* **2019**, *2019*, 3206024. https://doi.org/10.34133/2019/3206024.

(85) Handa, Y. P.; Stupin, D. Thermodynamic Properties and Dissociation Characteristics of Methane and Propane Hydrates in 70-Å-Radius Silica Gel Pores. *J. Phys. Chem.* **1992**, *96* (21), 8599–8603. https://doi.org/10.1021/j100200a071.

(86) Seo, Y. J.; Seol, J.; Yeon, S. H.; Koh, D. Y.; Cha, M.; Kang, S. P.; Seo, Y. T.; Bahk, J. J.; Lee, J.; Lee, H. Structural, Mineralogical, and Rheological Properties of Methane Hydrates in Smectite Clays. *J. Chem. Eng. Data* **2009**, *54* (4), 1284–1291. https://doi.org/10.1021/je800833y.

(87) Casco, M. E.; Rey, F.; Jordá, J. L.; Rudić, S.; Fauth, F.; Martínez-Escandell, M.; Rodríguez-Reinoso, F.; Ramos-Fernández, E. V.; Silvestre-Albero, J. Paving the Way for Methane Hydrate Formation on Metal-Organic Frameworks (MOFs). *Chem. Sci.* **2016**, *7* (6), 3658–3666. https://doi.org/10.1039/c6sc00272b.

(88) Kim, D.; Ahn, Y. H.; Lee, H. Phase Equilibria of CO2 and CH4 Hydrates in Intergranular Meso/Macro Pores of MIL-53 Metal Organic Framework. *J. Chem. Eng. Data* **2015**, *60*

(7), 2178–2185. https://doi.org/10.1021/acs.jced.5b00322.

(89) Liu, H.; Zhan, S.; Guo, P.; Fan, S.; Zhang, S. Understanding the Characteristic of Methane Hydrate Equilibrium in Materials and Its Potential Application. *Chem. Eng. J.* **2018**, *349*, 775–781. https://doi.org/10.1016/j.cej.2018.05.150.

(90) Mu, L.; Liu, B.; Liu, H.; Yang, Y.; Sun, C.; Chen, G. A Novel Method to Improve the Gas Storage Capacity of ZIF-8. *J. Mater. Chem.* **2012**, *22* (24), 12246–12252. https://doi.org/10.1039/c2jm31541f.

(91) He, Z.; Zhang, K.; Jiang, J. Formation of CH4 Hydrate in a Mesoporous Metal-Organic Framework MIL-101: Mechanistic Insights from Microsecond Molecular Dynamics Simulations. *J. Phys. Chem. Lett.* **2019**, 7002–7008. https://doi.org/10.1021/acs.jpclett.9b02808.

(92) Kong, X.; Jiang, J. Porous Organic Cage Membranes for Water Desalination: A Simulation Exploration. *Phys. Chem. Chem. Phys.* **2017**, *19* (28), 18178–18185. https://doi.org/10.1039/c7cp02670f.

(93) Columbia/MD, G. D.-; 2010, undefined. Sylobead Adsorbents for Process Applications.

(94) Hunger, B.; Heuchel, M.; Clark, L. A.; Snurr, R. Q. Characterization of Acidic OH Groups in Zeolites of Different Types: An Interpretation of NH3-TPD Results in the Light of Confinement Effects. *J. Phys. Chem. B* **2002**, *106* (15), 3882–3889. https://doi.org/10.1021/jp012688n.

(95) Chen, N. Y. Hydrophobic Properties of Zeolites. *J. Phys. Chem.* **1976**, *80* (1), 60–64.

(96) Andres-Garcia, E.; Dikhtiarenko, A.; Fauth, F.; Silvestre-Albero, J.; Ramos-Fernández, E. V.; Gascon, J.; Corma, A.; Kapteijn, F. Methane Hydrates: Nucleation in Microporous Materials. *Chem. Eng. J.* **2019**, *360*, 569–576. https://doi.org/10.1016/j.cej.2018.11.216.

(97) Kim, N.-J.; Park, S.-S.; Shin, S.-W.; Hyun, J.-H.; Chun, W. An Experimental Investigation into the Effects of Zeolites on the Formation of Methane Hydrates. *Int. J. Energy Res.* **2015**, *39* (1), 26–32. https://doi.org/10.1002/er.3201.

(98) Zang, X.; Du, J.; Liang, D.; Fan, S.; Tang, C. Influence of A-Type Zeolite on Methane Hydrate Formation. *Chinese J. Chem. Eng.* **2009**, *17* (5), 854–859. https://doi.org/10.1016/S1004-9541(08)60287-6.

(99) Zhao, Y.; Zhao, J.; Liang, W.; Gao, Q.; Yang, D. Semi-Clathrate Hydrate Process of Methane in Porous Media-Microporous Materials of 5A-Type Zeolites. *Fuel* **2018**, *220*, 185–191. https://doi.org/10.1016/j.fuel.2018.01.067.

(100) Casco, M. E.; Silvestre-Albero, J.; Ramírez-Cuesta, A. J.; Rey, F.; Jordá, J. L.; Bansode, A.; Urakawa, A.; Peral, I.; Martínez-Escandell, M.; Kaneko, K.; Rodríguez-Reinoso, F. Methane Hydrate Formation in Confined Nanospace Can Surpass Nature. *Nat. Commun.* **2015**, *6* (1), 1–8. https://doi.org/10.1038/ncomms7432.

(101) Cuadrado-Collados, C.; Fauth, F.; Such-Basañez, I.; Martínez-Escandell, M.; Silvestre-Albero, J. Methane Hydrate Formation in the Confined Nanospace of Activated Carbons in Seawater Environment. *Microporous Mesoporous Mater.* **2018**, *255*, 220–225.

https://doi.org/10.1016/j.micromeso.2017.07.047.

(102) Lim, S.-H.; Riffat, S. B.; Park, S.-S.; Oh, S.-J.; Chun, W.; Kim, N.-J. Enhancement of Methane Hydrate Formation Using a Mixture of Tetrahydrofuran and Oxidized Multi-Wall Carbon Nanotubes. *Int. J. Energy Res.* **2014**, *38* (3), 374–379. https://doi.org/10.1002/er.3051.

(103) Seo, Y.; Lee, H.; Uchida, T. Methane and Carbon Dioxide Hydrate Phase Behavior in Small Porous Silica Gels: Three-Phase Equilibrium Determination and Thermodynamic Modeling. *Langmuir* **2002**, *18* (24), 9164–9170. https://doi.org/10.1021/la0257844.

(104) Uchida, T.; Ebinuma, T.; Ishizaki, T. Dissociation Condition Measurements of Methane Hydrate in Confined Small Pores of Porous Glass. *J. Phys. Chem. B* **1999**, *103* (18), 3659–3662. https://doi.org/10.1021/jp984559l.

(105) Nair, V. C.; Ramesh, S.; Ramadass, G. A.; Sangwai, J. S. Influence of Thermal Stimulation on the Methane Hydrate Dissociation in Porous Media under Confined Reservoir. *J. Pet. Sci. Eng.* **2016**, *147*, 547–559. https://doi.org/10.1016/j.petrol.2016.09.017.

(106) Linga, P.; Haligva, C.; Nam, S. C.; Ripmeester, J. A.; Englezos, P. Gas Hydrate Formation in a Variable Volume Bed of Silica Sand Particles. *Energy and Fuels* **2009**, *23* (11), 5496–5507. https://doi.org/10.1021/ef900542m.

(107) Kim, D.; Ahn, Y. H.; Kim, S. J.; Lee, J. Y.; Lee, J.; Seo, Y. J.; Lee, H. Gas Hydrate in Crystalline-Swelled Clay: The Effect of Pore Dimension on Hydrate Formation and Phase Equilibria. *J. Phys. Chem. C* **2015**, *119* (38), 22148–22153. https://doi.org/10.1021/acs.jpcc.5b03229.

(108) Waite, W. F.; Winters, W. J.; Mason, D. H. Methane Hydrate Formation in Partially Water-Saturated Ottawa Sand. *Am. Mineral.* **2004**, *89* (8–9), 1202–1207. https://doi.org/10.2138/am-2004-8-906.

(109) Babu, P.; Kumar, R.; Linga, P. A New Porous Material to Enhance the Kinetics of Clathrate Process: Application to Precombustion Carbon Dioxide Capture. *Environ. Sci. Technol.* **2013**, *47* (22), 13191–13198. https://doi.org/10.1021/es403516f.

(110) Yang, L.; Fan, S.; Wang, Y.; Lang, X.; Xie, D. Accelerated Formation of Methane Hydrate in Aluminum Foam. *Ind. Eng. Chem. Res.* **2011**, *50* (20), 11563–11569. https://doi.org/10.1021/ie200825e.

(111) Zhong, D. L.; Li, Z.; Lu, Y. Y.; Wang, J. Le; Yan, J.; Qing, S. L. Investigation of CO2 Capture from a CO2 + CH4 Gas Mixture by Gas Hydrate Formation in the Fixed Bed of a Molecular Sieve. *Ind. Eng. Chem. Res.* **2016**, *55* (29), 7973–7980. https://doi.org/10.1021/acs.iecr.5b03989.

(112) Lin, K. S.; Adhikari, A. K.; Ku, C. N.; Chiang, C. L.; Kuo, H. Synthesis and Characterization of Porous HKUST-1 Metal Organic Frameworks for Hydrogen Storage. In *International Journal of Hydrogen Energy*; Pergamon, 2012; Vol. 37, pp 13865–13871. https://doi.org/10.1016/j.ijhydene.2012.04.105.

(113) Senkovska, I.; Kaskel, S. High Pressure Methane Adsorption in the Metal-Organic

Frameworks Cu3(Btc)2, Zn2(Bdc)2dabco, and Cr3F(H2O)2O(Bdc)3. *Microporous Mesoporous Mater.* **2008**, *112* (1–3), 108–115. https://doi.org/10.1016/j.micromeso.2007.09.016.

(114) Guthrie, S.; Huelsenbeck, L.; Salahi, A.; Varhue, W.; Smith, N.; Yu, X.; Yoon, L. U.; Choi, J. J.; Swami, N.; Giri, G. Crystallization of High Aspect Ratio HKUST-1 Thin Films in Nanoconfined Channels for Selective Small Molecule Uptake. *Nanoscale Adv.* **2019**, *1* (8), 2946–2952. https://doi.org/10.1039/c9na00254e.

(115) Babaei, H.; McGaughey, A. J. H.; Wilmer, C. E. Transient Mass and Thermal Transport during Methane Adsorption into the Metal-Organic Framework HKUST-1. *ACS Appl. Mater. Interfaces* **2018**, *10* (3), 2400–2406. https://doi.org/10.1021/acsami.7b13605.

(116) HKUST-1 Metal Organic Framework https://www.chemtube3d.com/mof-hkust-1-2/ (accessed May 18, 2020).

(117) Methane/Propane Double Hydrate | Janda Lab https://ps.uci.edu/group/kcjanda/research/methanepropane-double-hydrate (accessed May 18, 2020).

(118) Sun, B.; Kayal, S.; Chakraborty, A. Study of HKUST (Copper Benzene-1,3,5-Tricarboxylate, Cu-BTC MOF)-1 Metal Organic Frameworks for CH4 Adsorption: An Experimental Investigation with GCMC (Grand Canonical Monte-Carlo) Simulation. *Energy* **2014**, *76*, 419–427. https://doi.org/10.1016/j.energy.2014.08.033.

(119) Prestipino, C.; Regli, L.; Vitillo, J. G.; Bonino, F.; Damin, A.; Lamberti, C.; Zecchina, A.; Solari, P. L.; Kongshaug, K. O.; Bordiga, S. Local Structure of Framework Cu(II) in HKUST-1 Metallorganic Framework: Spectroscopic Characterization upon Activation and Interaction with Adsorbates. *Chemistry of Materials*. 2006, pp 1337–1346. https://doi.org/10.1021/cm052191g.

(120) Guerrero, V. V.; Yoo, Y.; McCarthy, M. C.; Jeong, H. K. HKUST-1 Membranes on Porous Supports Using Secondary Growth. *J. Mater. Chem.* **2010**, *20* (19), 3938–3943. https://doi.org/10.1039/b924536g.

(121) Lachance, J. Investigation of Gas Hydrates Using Differential Scanning Calorimetry with Water-in-Oil Emulsions, Colorado School of Mines, Golden, 2008.

(122) Gupta, A.; Lachance, J.; Sloan, E. D.; Koh, C. A. Measurements of Methane Hydrate Heat of Dissociation Using High Pressure Differential Scanning Calorimetry. *Chem. Eng. Sci.* **2008**, *63* (24), 5848–5853. https://doi.org/10.1016/j.ces.2008.09.002.

(123) Moellmer, J.; Moeller, A.; Dreisbach, F.; Glaeser, R.; Staudt, R. High Pressure Adsorption of Hydrogen, Nitrogen, Carbon Dioxide and Methane on the Metal-Organic Framework HKUST-1. *Microporous Mesoporous Mater.* **2011**, *138* (1–3), 140–148. https://doi.org/10.1016/j.micromeso.2010.09.013.

(124) Falenty, A.; Kuhs, W. F.; Glockzin, M.; Rehder, G. "self-Preservation" of CH4 Hydrates for Gas Transport Technology: Pressure-Temperature Dependence and Ice Microstructures. *Energy and Fuels* **2014**, *28* (10), 6275–6283. https://doi.org/10.1021/ef501409g.

(125) Mimachi, H.; Takeya, S.; Yoneyama, A.; Hyodo, K.; Takeda, T.; Gotoh, Y.; Murayama, T. Natural Gas Storage and Transportation within Gas Hydrate of Smaller Particle: Size Dependence of Self-Preservation Phenomenon of Natural Gas Hydrate. *Chem. Eng. Sci.* **2014**, *118*, 208–213. https://doi.org/10.1016/j.ces.2014.07.050.

(126) Gul-E-Noor, F.; Michel, D.; Krautscheid, H.; Haase, J.; Bertmer, M. Time Dependent Water Uptake in Cu3(Btc)2 MOF: Identification of Different Water Adsorption States by 1H MAS NMR. *Microporous Mesoporous Mater.* **2013**, *180*, 8–13. https://doi.org/10.1016/j.micromeso.2013.06.033.

(127) Taylor, C. J.; Miller, K. T.; Koh, C. A.; Sloan, E. D. Macroscopic Investigation of Hydrate Film Growth at the Hydrocarbon/Water Interface. *Chem. Eng. Sci.* **2007**, *62* (23), 6524–6533. https://doi.org/10.1016/j.ces.2007.07.038.

(128) Bai, D.; Chen, G.; Zhang, X.; Sum, A. K.; Wang, W. How Properties of Solid Surfaces Modulate the Nucleation of Gas Hydrate. *Sci. Rep.* **2015**, *5* (1), 1–12. https://doi.org/10.1038/srep12747.

(129) Koh, C. A.; Wisbey, R. P.; Wu, X.; Westacott, R. E.; Soper, A. K. Water Ordering around Methane during Hydrate Formation. *J. Chem. Phys.* **2000**, *113* (15), 6390–6397. https://doi.org/10.1063/1.1288818.

(130) Andrew Lin, K. Y.; Hsieh, Y. T. Copper-Based Metal Organic Framework (MOF), HKUST-1, as an Efficient Adsorbent to Remove p-Nitrophenol from Water. *J. Taiwan Inst. Chem. Eng.* **2015**, *50*, 223–228. https://doi.org/10.1016/j.jtice.2014.12.008.

(131) Linga, P.; Daraboina, N.; Ripmeester, J. A.; Englezos, P. Enhanced Rate of Gas Hydrate Formation in a Fixed Bed Column Filled with Sand Compared to a Stirred Vessel. *Chem. Eng. Sci.* **2012**, *68* (1), 617–623. https://doi.org/10.1016/j.ces.2011.10.030.

(132) Prasad, P. S. R.; Sowjanya, Y.; Dhanunjana Chari, V. Enhancement in Methane Storage Capacity in Gas Hydrates Formed in Hollow Silica. *J. Phys. Chem. C* **2014**, *118* (15), 7759–7764. https://doi.org/10.1021/jp411873m.

(133) Findenegg, G. H.; Jähnert, S.; Akcakayiran, D.; Schreiber, A. Freezing and Melting of Water Confined in Silica Nanopores. *ChemPhysChem* **2008**, *9*, 2651–2659. https://doi.org/10.1002/cphc.200800616.

(134) Carreon, M. A.; Guliants, V. V. Macroporous Vanadium Phosphorus Oxide Phases Displaying Three-Dimensional Arrays of Spherical Voids. *Chem. Mater.* **2002**, *14* (6), 2670–2675. https://doi.org/10.1021/cm0117376.

(135) Domán, A.; Czakkel, O.; Porcar, L.; Madarász, J.; Geissler, E.; László, K. Role of Water Molecules in the Decomposition of HKUST-1: Evidence from Adsorption, Thermoanalytical, X-Ray and Neutron Scattering Measurements. *Appl. Surf. Sci.* **2019**, *480*, 138–147. https://doi.org/10.1016/j.apsusc.2019.02.177.

(136) Majano, G.; Martin, O.; Hammes, M.; Smeets, S.; Baerlocher, C.; Pérez-Ramírez, J. Solvent-Mediated Reconstruction of the Metal-Organic Framework HKUST-1 (Cu3(BTC)2). *Adv. Funct. Mater.* **2014**, *24* (25), 3855–3865. https://doi.org/10.1002/adfm.201303678.

(137) Sun, X.; Li, H.; Li, Y.; Xu, F.; Xiao, J.; Xia, Q.; Li, Y.; Li, Z. A Novel Mechanochemical Method for Reconstructing the Moisture-Degraded HKUST-1. *Chem. Commun.* **2015**, *51* (54), 10835–10838. https://doi.org/10.1039/c5cc02809d.

(138) Bazer-Bachi, D.; Assié, L.; Lecocq, V.; Harbuzaru, B.; Falk, V. Towards Industrial Use of Metal-Organic Framework: Impact of Shaping on the MOF Properties. *Powder Technol.* **2014**, *255*, 52–59. https://doi.org/10.1016/j.powtec.2013.09.013.

(139) Decoste, J. B.; Peterson, G. W.; Schindler, B. J.; Killops, K. L.; Browe, M. A.; Mahle, J. J. The Effect of Water Adsorption on the Structure of the Carboxylate Containing Metal-Organic Frameworks Cu-BTC, Mg-MOF-74, and UiO-66. *J. Mater. Chem. A* **2013**, *1* (38), 11922–11932. https://doi.org/10.1039/c3ta12497e.

(140) Zhou, H. C.; Long, J. R.; Yaghi, O. M. Introduction to Metal−Organic Frameworks. *Chem. Rev.* **2012**, *112*, 673–674. https://doi.org/10.1021/cr300014x.

(141) Chen, B.; Yang, Z.; Zhu, Y.; Xia, Y. Zeolitic Imidazolate Framework Materials: Recent Progress in Synthesis and Applications. *Journal of Materials Chemistry A*. Royal Society of Chemistry October 28, 2014, pp 16811–16831. https://doi.org/10.1039/c4ta02984d.

(142) Bao, Q.; Lou, Y.; Xing, T.; Chen, J. Rapid Synthesis of Zeolitic Imidazolate Framework-8 (ZIF-8) in Aqueous Solution via Microwave Irradiation. *Inorg. Chem. Commun.* **2013**, *37*, 170–173. https://doi.org/10.1016/j.inoche.2013.09.061.

(143) Guo, X.; Xing, T.; Lou, Y.; Chen, J. Controlling ZIF-67 Crystals Formation through Various Cobalt Sources in Aqueous Solution. *J. Solid State Chem.* **2016**, *235*, 107–112. https://doi.org/10.1016/j.jssc.2015.12.021.

(144) Zhou, K.; Mousavi, B.; Luo, Z.; Phatanasri, S.; Chaemchuen, S.; Verpoort, F. Characterization and Properties of Zn/Co Zeolitic Imidazolate Frameworks vs. ZIF-8 and ZIF-67. *J. Mater. Chem. A* **2017**, *5* (3), 952–957. https://doi.org/10.1039/C6TA07860E.

(145) Khan, A.; Ali, M.; Ilyas, A.; Naik, P.; Vankelecom, I. F. J.; Gilani, M. A.; Bilad, M. R.; Sajjad, Z.; Khan, A. L. ZIF-67 Filled PDMS Mixed Matrix Membranes for Recovery of Ethanol via Pervaporation. *Sep. Purif. Technol.* **2018**, *206*, 50–58. https://doi.org/10.1016/j.seppur.2018.05.055.

(146) Sann, E. E.; Pan, Y.; Gao, Z.; Zhan, S.; Xia, F. Highly Hydrophobic ZIF-8 Particles and Application for Oil-Water Separation. *Sep. Purif. Technol.* **2018**, *206*, 186–191. https://doi.org/10.1016/j.seppur.2018.04.027.

(147) Matatagui, D.; Sainz-Vidal, A.; Gràcia, I.; Figueras, E.; Cané, C.; Saniger, J. Improving Sensitivity of a Chemoresistive Hydrogen Sensor by Combining ZIF-8 and ZIF-67 Nanocrystals. *Proceedings* **2017**, *1* (4), 462. https://doi.org/10.3390/proceedings1040462.

(148) Erkartal, M.; Erkilic, U.; Tam, B.; Usta, H.; Yazaydin, O.; Hupp, J. T.; Farha, O. K.; Sen, U. From 2-Methylimidazole to 1,2,3-Triazole: A Topological Transformation of ZIF-8 and ZIF-67 by Post-Synthetic Modification. *Chem. Commun.* **2017**, *53* (12), 2028–2031. https://doi.org/10.1039/c6cc08746a.

(149) Nguyen, N. N.; Galib, M.; Nguyen, A. V. Critical Review on Gas Hydrate Formation at Solid Surfaces and in Confined Spaces - Why and How Does Interfacial Regime Matter?

Energy and Fuels **2020**, *34* (6), 6751–6760. https://doi.org/10.1021/acs.energyfuels.0c01291.

(150) Khay, I.; Chaplais, G.; Nouali, H.; Ortiz, G.; Marichal, C.; Patarin, J. Assessment of the Energetic Performances of Various ZIFs with SOD or RHO Topology Using High Pressure Water Intrusion-Extrusion Experiments. *Dalt. Trans.* **2016**, *45* (10), 4392–4400. https://doi.org/10.1039/c5dt03486h.

(151) Klinowski, J.; Almeida Paz, F. A.; Silva, P.; Rocha, J. Microwave-Assisted Synthesis of Metal-Organic Frameworks. *Dalton Transactions*. Royal Society of Chemistry January 14, 2011, pp 321–330. https://doi.org/10.1039/c0dt00708k.

(152) Ni, Z.; Masel, R. I. Rapid Production of Metal-Organic Frameworks via Microwave-Assisted Solvothermal Synthesis. *J. Am. Chem. Soc.* **2006**, *128* (38), 12394–12395. https://doi.org/10.1021/ja0635231.

(153) Venna, S. R.; Carreon, M. A. Microwave Assisted Phase Transformation of Silicoaluminophosphate Zeolite Crystals. *J. Mater. Chem.* **2009**, *19* (20), 3138–3140. https://doi.org/10.1039/b903316e.

(154) Xie, Z.; Zhu, M.; Nambo, A.; Jasinski, J. B.; Carreon, M. A. Microwave-Assisted Synthesized SAPO-56 as a Catalyst in the Conversion of CO2 to Cyclic Carbonates. *Dalt. Trans.* **2013**, *42* (19), 6732–6735. https://doi.org/10.1039/c3dt00064h.

(155) Lucero, J.; Osuna, C.; Crawford, J. M.; Carreon, M. A. Microwave-Assisted Synthesis of Porous Organic Cages CC3 and CC2. *CrystEngComm* **2019**, *21* (31), 4534–4537. https://doi.org/10.1039/c9ce00880b.

(156) Qian, J.; Sun, F.; Qin, L. Hydrothermal Synthesis of Zeolitic Imidazolate Framework-67 (ZIF-67) Nanocrystals. *Mater. Lett.* **2012**, *82*, 220–223. https://doi.org/10.1016/j.matlet.2012.05.077.

(157) Llewellyn, P.; Reinoso, F.; Rouqerol, J.; Seaton, N. *Characterization of Porous Solids VII: Proceedings of the 7th International Symposium on the Characterization of Porous Solids (COPS-VII), Aix-En-Provence*; 2006.

(158) An, H.; Park, S.; Kwon, H. T.; Jeong, H. K.; Lee, J. S. A New Superior Competitor for Exceptional Propylene/Propane Separations: ZIF-67 Containing Mixed Matrix Membranes. *J. Memb. Sci.* **2017**, *526*, 367–376. https://doi.org/10.1016/j.memsci.2016.12.053.

(159) Zhang, K.; Lively, R. P.; Zhang, C.; Koros, W. J.; Chance, R. R. Investigating the Intrinsic Ethanol/Water Separation Capability of ZIF-8: An Adsorption and Diffusion Study. *J. Phys. Chem. C* **2013**, *117* (14), 7214–7225. https://doi.org/10.1021/jp401548b.

(160) Tu, M.; Wannapaiboon, S.; Khaletskaya, K.; Fischer, R. A. Engineering Zeolitic-Imidazolate Framework (ZIF) Thin Film Devices for Selective Detection of Volatile Organic Compounds. *Adv. Funct. Mater.* **2015**, *25* (28), 4470–4479. https://doi.org/10.1002/adfm.201500760.

(161) Koh, C. A.; Wisbey, R. P.; Wu, X.; Westacott, R. E.; Soper, A. K. Water Ordering around Methane during Hydrate Formation. *J. Chem. Phys.* **2000**, *113* (15), 6390–6397.

https://doi.org/10.1063/1.1288818.

(162) Liang, S.; Rozmanov, D.; Kusalik, P. G. Crystal Growth Simulations of Methane Hydrates in the Presence of Silica Surfaces. *Phys. Chem. Chem. Phys.* **2011**, *13* (44), 19856–19864. https://doi.org/10.1039/c1cp21810g.

(163) Kwon, T.-H.; Cho, G.-C.; Santamarina, J. C. Gas Hydrate Dissociation in Sediments: Pressure-Temperature Evolution. *Geochemistry, Geophys. Geosystems* **2008**, *9* (3), n/a-n/a. https://doi.org/10.1029/2007GC001920.

(164) Park, T.; Lee, J. Y.; Kwon, T. H. Effect of Pore Size Distribution on Dissociation Temperature Depression and Phase Boundary Shift of Gas Hydrate in Various Fine-Grained Sediments. *Energy and Fuels* **2018**, *32* (4), 5321–5330. https://doi.org/10.1021/acs.energyfuels.8b00074.

(165) Fairen-Jimenez, D.; Moggach, S. A.; Wharmby, M. T.; Wright, P. A.; Parsons, S.; Düren, T. Opening the Gate: Framework Flexibility in ZIF-8 Explored by Experiments and Simulations. *J. Am. Chem. Soc.* **2011**, *133* (23), 8900–8902. https://doi.org/10.1021/ja202154j.

(166) Awadallah-F, A.; Hillman, F.; Al-Muhtaseb, S. A.; Jeong, H. K. Adsorption Equilibrium and Kinetics of Nitrogen, Methane and Carbon Dioxide Gases onto ZIF-8, Cu10%/ZIF-8, and Cu30%/ZIF-8. *Ind. Eng. Chem. Res.* **2019**, *58* (16), 6653–6661. https://doi.org/10.1021/acs.iecr.8b05892.

(167) Feng, X.; Carreon, M. A. Kinetics of Transformation on ZIF-67 Crystals. *J. Cryst. Growth* **2015**, *418*, 158–162. https://doi.org/10.1016/j.jcrysgro.2015.02.064.

(168) Tozawa, T.; Jones, J. T. A.; Swamy, S. I.; Jiang, S.; Adams, D. J.; Shakespeare, S.; Clowes, R.; Bradshaw, D.; Hasell, T.; Chong, S. Y.; Tang, C.; Thompson, S.; Parker, J.; Trewin, A.; Bacsa, J.; Slawin, A. M. Z.; Steiner, A.; Cooper, A. I. Porous Organic Cages. *Nat. Mater.* **2009**, *8* (12), 973–978. https://doi.org/10.1038/nmat2545.

(169) Little, M. A.; Cooper, A. I. The Chemistry of Porous Organic Molecular Materials. *Advanced Functional Materials*. Wiley-VCH Verlag October 1, 2020, p 1909842. https://doi.org/10.1002/adfm.201909842.

(170) Chen, L.; Reiss, P. S.; Chong, S. Y.; Holden, D.; Jelfs, K. E.; Hasell, T.; Little, M. A.; Kewley, A.; Briggs, M. E.; Stephenson, A.; Al, E. Separation of Rare Gases and Chiral Molecules by Selective Binding in Porous Organic Cages. *Nat. Mater.* **2014**, *13* (10), 954–960. https://doi.org/10.1038/nmat4035.

(171) Komulainen, S.; Roukala, J.; Zhivonitko, V. V.; Javed, M. A.; Chen, L.; Holden, D.; Hasell, T.; Cooper, A.; Lantto, P.; Telkki, V. V. Inside Information on Xenon Adsorption in Porous Organic Cages by NMR. *Chem. Sci.* **2017**, *8* (8), 5721–5727. https://doi.org/10.1039/c7sc01990d.

(172) Hasell, T.; Armstrong, J. A.; Jelfs, K. E.; Tay, F. H.; Thomas, K. M.; Kazarian, S. G.; Cooper, A. I. High-Pressure Carbon Dioxide Uptake for Porous Organic Cages: Comparison of Spectroscopic and Manometric Measurement Techniques. *Chem. Commun.* **2013**, *49* (82), 9410–9412. https://doi.org/10.1039/c3cc45924a.

(173) Liu, M.; Chen, L.; Lewis, S.; Chong, S. Y.; Little, M. A.; Hasell, T.; Aldous, I. M.; Brown, C. M.; Smith, M. W.; Morrison, C. A.; Hardwick, L. J.; Cooper, A. I. Three-Dimensional Protonic Conductivity in Porous Organic Cage Solids. *Nat. Commun.* **2016**, *7* (1), 1–9. https://doi.org/10.1038/ncomms12750.

(174) Kewley, A.; Stephenson, A.; Chen, L.; Briggs, M. E.; Hasell, T.; Cooper, A. I. Porous Organic Cages for Gas Chromatography Separations. *Chem. Mater.* **2015**, *27* (9), 3207–3210. https://doi.org/10.1021/acs.chemmater.5b01112.

(175) Sun, J. K.; Zhan, W. W.; Akita, T.; Xu, Q. Toward Homogenization of Heterogeneous Metal Nanoparticle Catalysts with Enhanced Catalytic Performance: Soluble Porous Organic Cage as a Stabilizer and Homogenizer. *J. Am. Chem. Soc.* **2015**, *137* (22), 7063–7066. https://doi.org/10.1021/jacs.5b04029.

(176) Hasell, T.; Miklitz, M.; Stephenson, A.; Little, M. A.; Chong, S. Y.; Clowes, R.; Chen, L.; Holden, D.; Tribello, G. A.; Jelfs, K. E.; Cooper, A. I. Porous Organic Cages for Sulfur Hexafluoride Separation. *J. Am. Chem. Soc.* **2016**, *138* (5), 1653–1659. https://doi.org/10.1021/jacs.5b11797.

(177) Deshmane, C. A.; Jasinski, J. B.; Carreon, M. A. Microwave-Assisted Synthesis of Nanocrystalline Mesoporous Gallium Oxide. *Microporous Mesoporous Mater.* **2010**, *130* (1–3), 97–102. https://doi.org/10.1016/J.MICROMESO.2009.10.018.

(178) Sing, K. S. W. Assessment of Surface Area by Gas Adsorption. In *Adsorption by Powders and Porous Solids: Principles, Methodology and Applications: Second Edition*; Elsevier Inc., 2013; pp 237–268. https://doi.org/10.1016/B978-0-08-097035-6.00007-3.

(179) Ghorbani, H.; Ghahramaninezhad, M.; Niknam Shahrak, M. The Effect of Organic and Ionic Liquid Solvents on Structure Crystallinity and Crystallite Size of ZIF-8 for CO2 Uptake. *J. Solid State Chem.* **2020**, *289*, 121512. https://doi.org/10.1016/j.jssc.2020.121512.

(180) Veluswamy, H. P.; Prasad, P. S. R.; Linga, P. Mechanism of Methane Hydrate Formation in the Presence of Hollow Silica. *Korean J. Chem. Eng.* **2016**, *33* (7), 2050–2062. https://doi.org/10.1007/s11814-016-0039-0.

(181) Chari, V. D.; Sharma, D. V. S. G. K.; Prasad, P. S. R.; Murthy, S. R. Methane Hydrates Formation and Dissociation in Nano Silica Suspension. *J. Nat. Gas Sci. Eng.* **2013**, *11*, 7–11. https://doi.org/10.1016/j.jngse.2012.11.004.

(182) Guo, Y.; Xiao, W.; Pu, W.; Hu, J.; Zhao, J.; Zhang, L. CH4 Nanobubbles on the Hydrophobic Solid-Water Interface Serving as the Nucleation Sites of Methane Hydrate. *Langmuir* **2018**, *34* (34), 10181–10186. https://doi.org/10.1021/acs.langmuir.8b01900.

(183) Hasell, T.; Schmidtmann, M.; Stone, C. A.; Smith, M. W.; Cooper, A. I. Reversible Water Uptake by a Stable Imine-Based Porous Organic Cage. *Chem. Commun.* **2012**, *48* (39), 4689–4691. https://doi.org/10.1039/c2cc31212c.

(184) Chong, Z. R.; Yang, M.; Khoo, B. C.; Linga, P. Size Effect of Porous Media on Methane Hydrate Formation and Dissociation in an Excess Gas Environment. *Ind. Eng. Chem. Res.* **2016**, *55* (29), 7981–7991. https://doi.org/10.1021/acs.iecr.5b03908.

(185) Slater, A. G.; Reiss, P. S.; Pulido, A.; Little, M. A.; Holden, D. L.; Chen, L.; Chong, S. Y.; Alston, B. M.; Clowes, R.; Haranczyk, M.; Briggs, M. E.; Hasell, T.; Day, G. M.; Cooper, A. I. Computationally-Guided Synthetic Control over Pore Size in Isostructural Porous Organic Cages. *ACS Cent. Sci.* **2017**, *3* (7), 734–742. https://doi.org/10.1021/acscentsci.7b00145.

(186) Zhu, G.; Liu, Y.; Flores, L.; Lee, Z. R.; Jones, C. W.; Dixon, D. A.; Sholl, D. S.; Lively, R. P. Formation Mechanisms and Defect Engineering of Imine-Based Porous Organic Cages. *Chem. Mater.* **2018**, *30* (1), 262–272. https://doi.org/10.1021/acs.chemmater.7b04323.

(187) Denning, S.; Majid, A. A. A.; Lucero, J. M.; Crawford, J. M.; Carreon, M. A.; Koh, C. A. Methane Hydrate Growth Promoted by Microporous Zeolitic Imidazolate Frameworks ZIF-8 and ZIF-67 for Enhanced Methane Storage. *ACS Sustain. Chem. Eng.* **2021**, *9* (27), 9001–9010. https://doi.org/10.1021/ACSSUSCHEMENG.1C01488.

(188) Li, S.; Falconer, J. L.; Noble, R. D. SAPO-34 Membranes for CO2/CH4 Separation. *J. Memb. Sci.* **2004**, *241* (1), 121–135. https://doi.org/10.1016/J.MEMSCI.2004.04.027.

(189) Koh, C. A.; Sloan, E. D. Natural Gas Hydrates: Recent Advances and Challenges in Energy and Environmental Applications. *AIChE J.* **2007**, *53* (7), 1636–1643. https://doi.org/10.1002/aic.11219.

(190) Poshusta, J. C.; Noble, R. D.; Falconer, J. L. Characterization of SAPO-34 Membranes by Water Adsorption. *J. Memb. Sci.* **2001**, *186* (1), 25–40. https://doi.org/10.1016/S0376-7388(00)00666-9.

(191) Kosinov, N.; Auffret, C.; Borghuis, G. J.; Sripathi, V. G. P.; Hensen, E. J. M. Influence of the Si/Al Ratio on the Separation Properties of SSZ-13 Zeolite Membranes. *J. Memb. Sci.* **2015**, *484*, 140–145. https://doi.org/10.1016/j.memsci.2015.02.044.

(192) Nguyen, N. N.; Nguyen, A. V. Hydrophobic Effect on Gas Hydrate Formation in the Presence of Additives. *Energy and Fuels* **2017**, *31* (10), 10311–10323. https://doi.org/10.1021/ACS.ENERGYFUELS.7B01467.

(193) Wu, T.; Lucero, J.; Crawford, J. M.; Sinnwell, M. A.; Thallapally, P. K.; Carreon, M. A. SAPO-34 Membranes for Xenon Capture from Air. *J. Memb. Sci.* **2019**, *573*, 288–292. https://doi.org/10.1016/j.memsci.2018.12.021.

(194) Luo, Y.; Funke, H. H.; Falconer, J. L.; Noble, R. D. Adsorption of CO_2, CH_4, C_3H_8, and H_2O in SSZ-13, SAPO-34, and T-Type Zeolites. *Ind. Eng. Chem. Res.* **2016**, *55* (36), 9749–9757. https://doi.org/10.1021/acs.iecr.6b02034.

(195) Deimund, M. A.; Harrison, L.; Lunn, J. D.; Liu, Y.; Malek, A.; Shayib, R.; Davis, M. E. Effect of Heteroatom Concentration in SSZ-13 on the Methanol-to-Olefins Reaction. *ACS Catal.* **2015**, *6* (2), 542–550. https://doi.org/10.1021/ACSCATAL.5B01450.

(196) Denning, S.; Lucero, J. M.; Majid, A. A. A.; Crawford, J. M.; Carreon, M. A.; Koh, C. A. Porous Organic Cage CC3: An Effective Promoter for Methane Hydrate Formation for Natural Gas Storage. *J. Phys. Chem. C* **2021**. https://doi.org/10.1021/ACS.JPCC.1C04657.

(197) Veluswamy, H. P.; Wong, A. J. H.; Babu, P.; Kumar, R.; Kulprathipanja, S.;

Rangsunvigit, P.; Linga, P. Rapid Methane Hydrate Formation to Develop a Cost Effective Large Scale Energy Storage System. *Chem. Eng. J.* **2016**, *290*, 161–173. https://doi.org/10.1016/j.cej.2016.01.026.

(198) Hao, W.; Wang, J.; Fan, S.; Hao, W. Evaluation and Analysis Method for Natural Gas Hydrate Storage and Transportation Processes. **2008**, *49* (10), 2546–2553. https://doi.org/10.1016/j.enconman.2008.05.016.

(199) Park, Y.; Kim, D. Y.; Lee, J. W.; Huh, D. G.; Park, K. P.; Lee, J.; Lee, H. Sequestering Carbon Dioxide into Complex Structures of Naturally Occurring Gas Hydrates. *Proc. Natl. Acad. Sci. U. S. A.* **2006**, *103* (34), 12690–12694. https://doi.org/10.1073/pnas.0602251103.

(200) Lee, Y.; Lee, S.; Lee, J.; Seo, Y. Structure Identification and Dissociation Enthalpy Measurements of the CO2 + N2 Hydrates for Their Application to CO2 Capture and Storage. *Chem. Eng. J.* **2014**, *246*, 20–26. https://doi.org/10.1016/J.CEJ.2014.02.045.

(201) Warrier, P.; Naveed Khan, M.; Carreon, M. A.; Peters, C. J.; Koh, C. A. Integrated Gas Hydrate-Membrane System for Natural Gas Purification. *J. Renew. Sustain. Energy* **2018**, *10* (3), 034701. https://doi.org/10.1063/1.5019967.

(202) Zheng, J. nan; Yang, M. Experimental Investigation on Novel Desalination System via Gas Hydrate. *Desalination* **2020**, *478*, 114284. https://doi.org/10.1016/J.DESAL.2019.114284.

(203) Inkong, K.; Veluswamy, H. P.; Rangsunvigit, P.; Kulprathipanja, S.; Linga, P. Innovative Approach to Enhance the Methane Hydrate Formation at Near-Ambient Temperature and Moderate Pressure for Gas Storage Applications. *Ind. Eng. Chem. Res.* **2019**, *58* (49), 22178–22192. https://doi.org/10.1021/acs.iecr.9b04498.

(204) Pahlavanzadeh, H.; Rezaei, S.; Khanlarkhani, M.; Manteghian, M.; Mohammadi, A. H. Kinetic Study of Methane Hydrate Formation in the Presence of Copper Nanoparticles and CTAB. *J. Nat. Gas Sci. Eng.* **2016**, *34*, 803–810. https://doi.org/10.1016/j.jngse.2016.07.001.

APPENDIX A

The following copyright permissions were obtained and attached as supplementary files.

1. Permission from journals for published works presented in this thesis:
    a. Copyright Permissions ACS Applied Materials & Interfaces
    b. Copyright Permissions ACS Sustainable Chemistry & Engineering
    c. Copyright Permissions the Journal of Physical Chemistry C
2. Co-author permission for published works and manuscript under review:
    a. Co-author Permission Publications – Ahmad AA Majid
    b. Co-author Permission Publications – James Crawford
    c. Co-author Permission Publications – Jolie Lucero
    d. Co-author Permission Submitted Article – Ahmad AA Majid
    e. Co-author Permission Submitted Article – James Crawford
3. Permissions from journals to reprint selected figures:
    a. Copyright Permissions Thesis Figure 2.8
    b. Copyright Permissions Thesis Figure 2.9